# Characterisation of Interface Spin Clusters in Polycrystalline Exchange Bias Thin Films

Nicholas Charles Cramp

Doctor of Philosophy

University of York

Physics

May 2013

## Abstract

A study of exchange bias systems has been made focusing on the characteristics of the interfacial spin clusters found in-between the bilayers. The materials studied were primarily IrMn (10nm) / CoFe (2nm) thin films of varying grain sizes. They were selected as the bulk properties have already been well characterised and they exhibit the effects being looked for.

A combination of vibrating sample magnetometry and electron microscopy has been used to investigate the nature of the interfacial spin clusters. Measurements were selected which specifically highlight the properties of the clusters. The first set of measurements consisted of increasing the setting field. The second, reducing the measurement temperature of median blocking curve measurements. The third involved taking hysteresis loops at liquid Helium temperatures.

The first set of measurements clearly showed an increase in the exchange bias that was due to the interfacial spin clusters. This increase was shown to correlate with the spin cluster size of the samples and showed quasi-superparamagnetic behaviour. The second set of measurements showed a temperature dependent variation in coercivity that implied the coercivity was due to the interfacial spin clusters. The final set of measurements showed a change in behaviour of the spin clusters whereby they started to act as a spin glass, which again was cluster size dependent. All of these results could be explained by virtue of an energy barrier distribution of the spin clusters whereby they could take on one of three different states, thermally unstable, partially stable, or fully stable. Taken as a whole, the results and conclusions give a good insight into the nature of the interfacial spin clusters and their effects on the exchange bias and coercivity of IrMn / CoFe polycrystalline thin films.

## Contents

## List of Figures

## List of Tables

## Acknowledgements

*For those who had faith in me.*

## Declaration

I declare that the work presented in this thesis is based purely on my own research and has not already been submitted for a degree in either this or any other university. However, as stated in the text at the appropriate locations, some of the work has been published [*Cramp,2012*].

*Publications*

Cramp, N.C., Carpenter, R., O'Grady, K.,Characterisation of Interface Spin Clusters in Exchange Bias Systems. IEEE Transactions on Magnetics, 2012, 48(11): p2881-2884.

Signed

N.Cramp.

# 1. Applications of Exchange Bias

## 1.1 Spin Valves

### 1.1.1 History of Spin-Valves

There is an unending quest to store the ever increasing volume of data that is being generated, and one of the most successful ways of doing this has been on magnetic hard disk drives. The most important element of a hard disk drive is arguably the read / write head. The write head uses an inductive method to generate magnetic fields that can induce magnetisations of a particular direction in the hard disk drive. The read head makes use of the spin valve. This thesis focuses on a very particular aspect of the spin valve, but before this, there is a brief overview of its history.

The history of the spin valve has a number of important milestones. The first was in 1857 when William Thomson [*Thomson,1857*] discovered that the resistance of a ferromagnet varied when a magnetic field was applied.

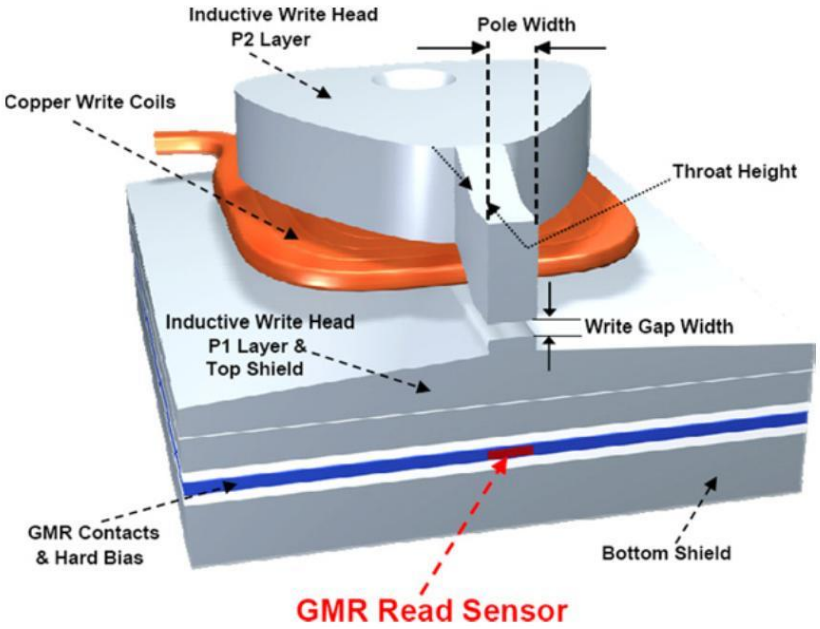


**Figure 1: GMR read-write head with inductive writer and GMR location [*Hitachi*].**

In 1896 [*Thomson,1897*] J. J. Thomson discovered the electron, in 1936 Sir Neville Mott predicted the existence of two separate spin channels in a charge current [*Mott,1936*] and in 1956 Meiklejohn [*Meiklejohn and Bean,1957*] discovered exchange bias. Finally, in 1988, Albert Fert and Peter Grünberg discovered giant magnetoresistance (GMR) [*Baibich,1988*].

Figure 1 shows where the giant magnetoresistance read sensor is located in a read / write head of a hard disk drive. Although a relatively small part of the overall instrument, its size is still very important in ultimately how much data can be stored on a disk. The smaller the read head, the smaller the bit size on the disk, which in turn leads to an increase in data density [*Fontana,2005*].

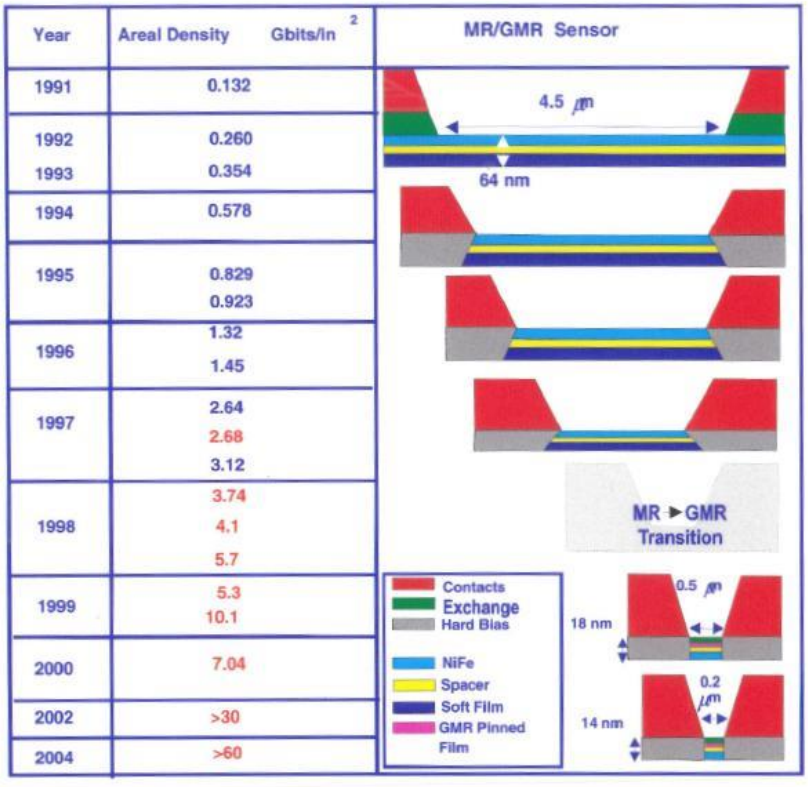


**Figure 2: Reduction in read sensor size with the introduction of GMR [*Hitachi*].**

At the time of the discovery of giant magnetoresistance, anisotropic magnetic resistance (AMR) read heads were being used in hard disk drives. When the AMR read head was initially used, it was the first time that the read head and write head

had become separate components, previously, both tasks had been carried out by same inductive unit. The AMR read head took advantage of the dependence of electrical resistance on the angle between the direction of electrical current and orientation of the magnetic field. However, GMR produced significantly more sensitive read heads. It took about 10 years to perfect the design of the giant magnetoresistance spin valve for use in hard disk drives after its discovery, but once this had happened, the conversion of the manufacturing procedure was relatively straight forward. The result of this was that by 2004 the dimensions of the read head sensor had reduced from 64nm thick and 4.5 µm wide to 14nm thick and 0.3 µm wide (Figure 2). This reduction in size along with other improvements led to the areal density improving from over 5 Gbits/in$^2$ in 2000 to over 500 Gbits/in$^2$ in 2012 [*IHS Technology*].

### 1.1.2 Development of GMR read head

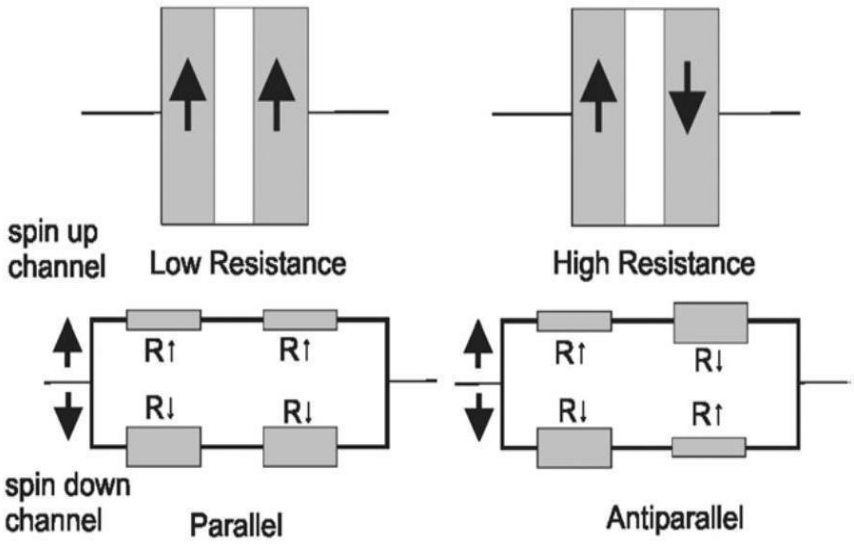


**Figure 3: Resistor network model of GMR [*Thompson,2008*].**

The basic principle behind a spin valve is relatively simple. A charged current consists of two carriers, spin up electrons and spin down electrons. Magnetism in a

material is due to it having a more electrons in one spin direction than the other. When a current passes through a magnetised material, the electrons whose spins are in the same direction as the orientation of the magnetisation will have less collisions and therefore experience lower resistance than the electrons whose spin is in the opposite direction. Looking at the left hand diagram in Figure 3, only the down spin channel will experience a high resistance (Equation 1-1), whereas with the right hand diagram (Equation 1-2), both spin channels experience a high resistance. Therefore, the antiparallel configuration has a higher overall resistance than the parallel configuration.

$$R_P = \frac{R\uparrow R\downarrow}{R\uparrow + R\downarrow} \qquad \text{Eqn. 1-1}$$

$$R_{AP} = \frac{R\uparrow + R\downarrow}{2} \qquad \text{Eqn. 1-2}$$

where $R_P$ is the resistance in the parallel configuration, $R_{AP}$ is the resistance in the antiparallel configuration, $R\uparrow$ is the resistance experience by the up spin electrons and $R\downarrow$ is the resistance experienced by the down spin electrons. It is one thing establishing the principle, but the application of this to the detection of the direction of a magnetic field poses an immediate problem. The purpose of one of the layers is to respond to the external magnetic field, but the other layer is required to be 'pinned'.

The first spin valves did not rely on the exchange bias effect, instead, it just relied on using ferromagnets of different coercivities [*Fert,2003*]. However, the most successful method by far was to take advantage of the exchange bias effect which had been discovered in 1956. Up until the concept of the spin valve, exchange bias was only of scientific curiosity, but when it was realised that it could be utilised in

spin valves the hard disk drive industry invested a great deal of effort into its understanding. The result was a proliferation of papers which dominated the research world of magnetism and is the primary subject of this thesis.

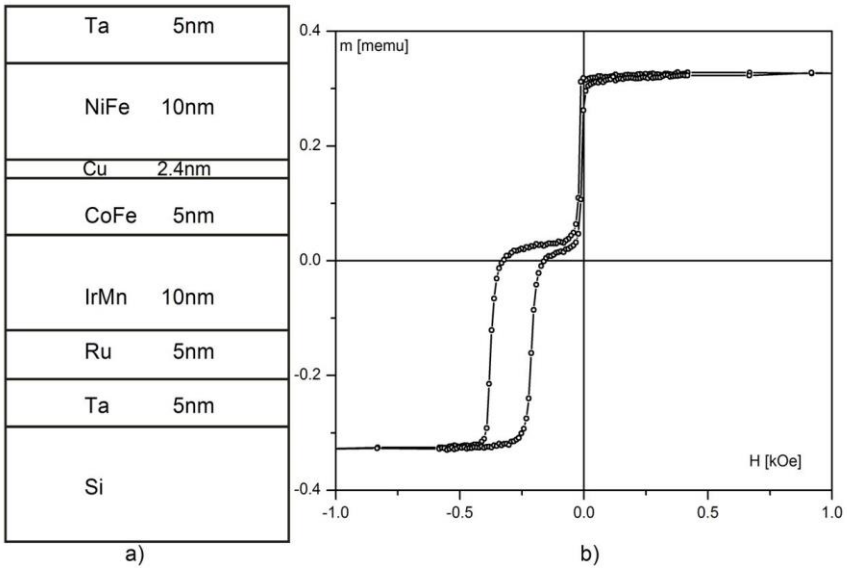


**Figure 4: Schematic of spin valve with corresponding hysteresis loop.**

A basic spin valve can be grown relatively easily and Figure 4 shows an example of the thickness of layers involved. The hysteresis loop nicely shows the advantage of using an antiferromagnet to pin the fixed ferromagnetic layer as the coercivity of the free layer is significantly lower than the exchange bias of the fixed layer.

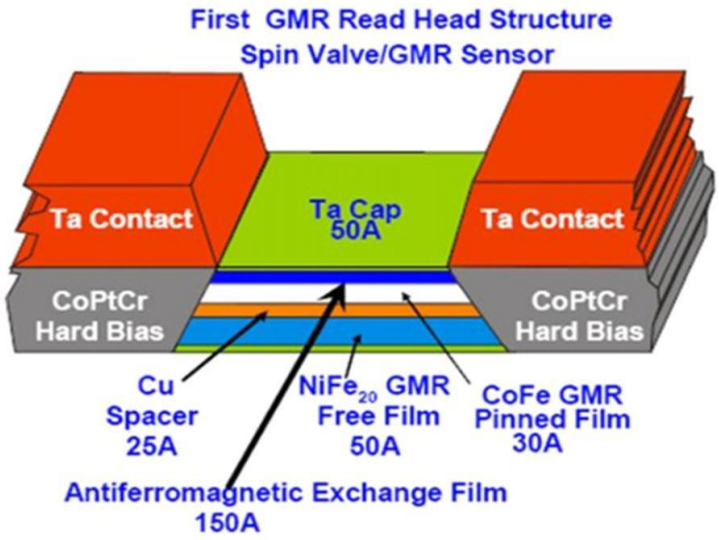


**Figure 5: GMR read sensor [*Hitachi*].**

Figure 5 shows how this system is adapted for actual use in a hard drive and can now be directly compared to Figure 1 which locates the position of the GMR sensor (lateral dimensions for this type of sensor have been given in Figure 2).

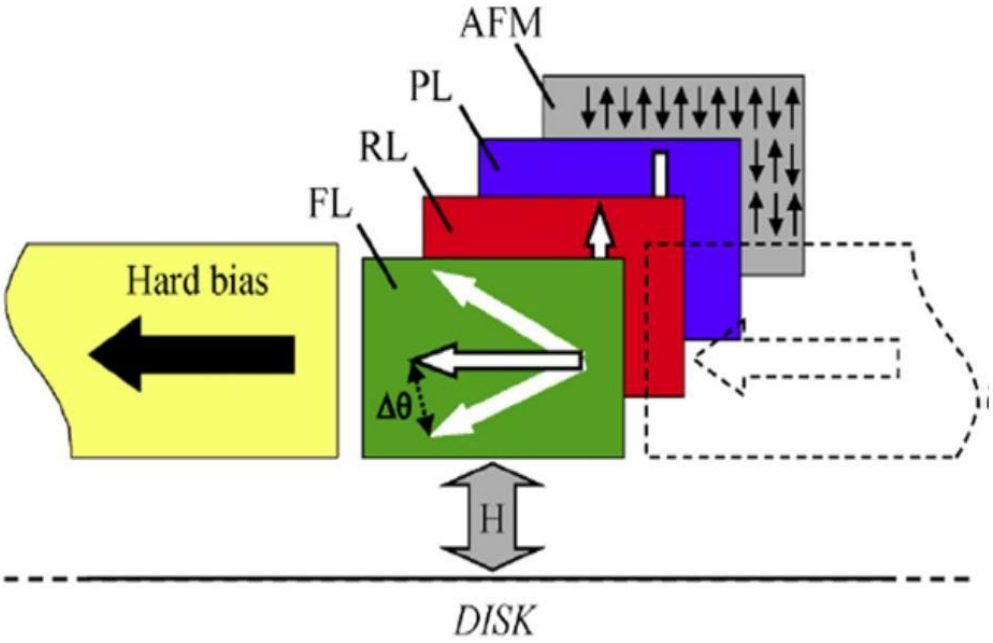


**Figure 6: Relative magnetisations of GMR head [*Fontana,2005*].**

A simple cross sectional schematic of the orientations of the free ferromagnetic layer (such as in Figure 3) suggests it rotates 180 degrees. This is not the case, the magnetisation of the free layer is actually aligned perpendicular to the fixed layer and it oscillates little more than 30 degrees (Figure 6).

$$\frac{\Delta R}{R} \propto \boldsymbol{M_1} \cdot \boldsymbol{M_2} \qquad \text{Eqn. 1-3}$$

As can be seen in Figure 7, the variation in magnetoresistance is at its greatest at 90 degrees and a 30 degree rotation of the free layer results in a sufficient change in the

resistance that can be measured. Equation 1-3 describes this function where $\boldsymbol{M_1}$ and $\boldsymbol{M_2}$ are the directions of magnetisation of the two layers and $R$ is the resistance.

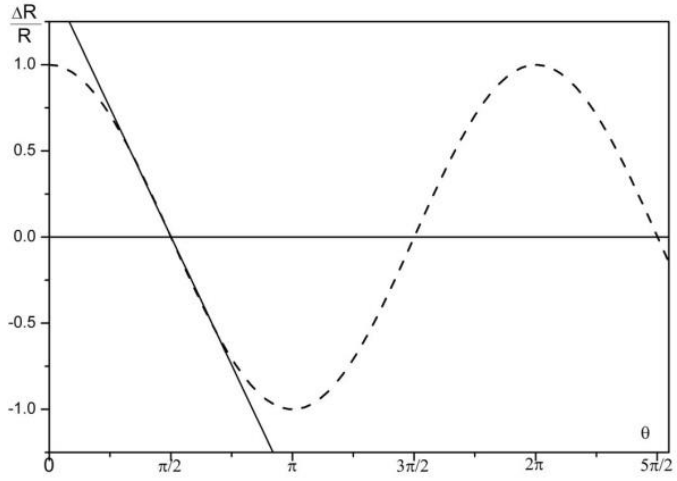


**Figure 7: Cosine dependence of giant magnetoresistance.**

## 1.2 Current Induced Magnetic Reversal

The spin valve was the first practical application of spintronics, or magnetoelectronics, in the data recording industry. As the technology has developed new concepts utilising spintronics have been discovered. With the spin valve, the effect of a magnetic field from a ferromagnet on a current is utilised, however, with current induced magnetic reversal, it is the effect of the current on the field that is of significance.

In 1996 Slonczewski [*Slonczewski,1996*] theoretically predicted what would happen when a current flowed perpendicularly to two parallel magnetic films connected by a normal metallic spacer. He suggested that, due to spin transfer torque, the switching of magnetic states could be achieved. Four years later Katine [*Katine,2000*] made a device which experimentally proved that this could happen.

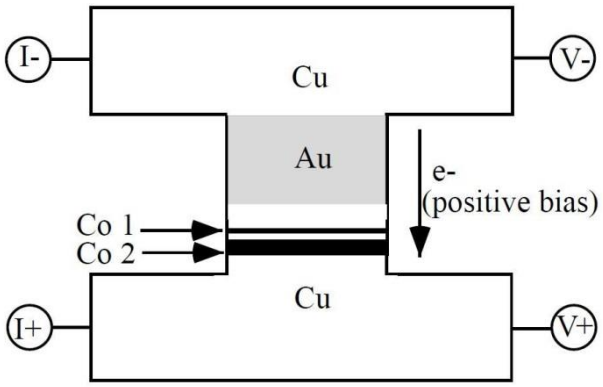


**Figure 8: Schematic of pillar device [*Katine,2000*].**

Figure 8 shows a schematic of the device. It was fabricated by sputtering 120nm Cu / 10nm Co / 6nm Cu / 2.5nm Co / 15nm Cu / 3nm Pt / 60nm Au on a silicon substrate. Electron beam lithography, evaporation and lift-off were used to pattern 100nm diameter pillars. The difference between the thicknesses of the Cobalt layers is so that the magnetisation of the thicker layer can be fixed.

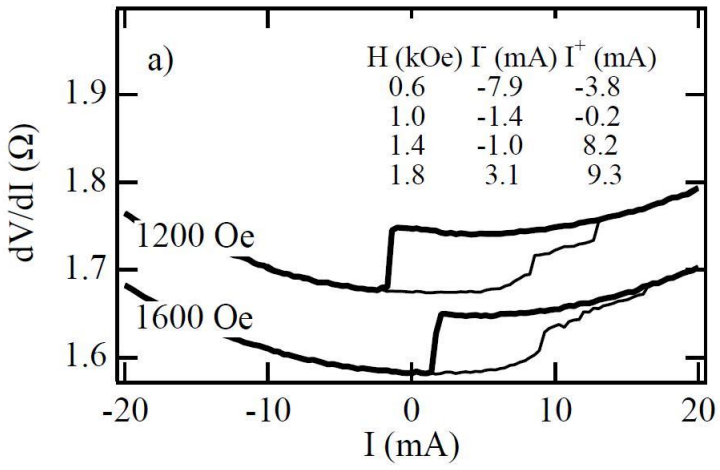


**Figure 9: dV / dI of a pillar device exhibiting hysteretic jumps as the current is swept [*Katine,2000*].**

Figure 9 shows the hysteretic variation in resistance as a function of the device current in the presence of a steady magnetic field. Two loops are shown, one when

1200 Oe was applied and another when 1600 Oe was applied. There are a number of aspects to this figure. The general curve increase in resistance is attributed to increased electron-magnon and electron-phonon scattering. The 1200 Oe sample starts at *I=0* in a low resistance state and, as the current is increased, the resistance increases in two jumps until it reaches the higher resistance state. If the current is reduced and then reversed, the system returns to the low resistance state. The 1600 Oe sample shows similar behaviour. The low resistance state is assumed to be when the magnetic layers are in parallel alignment and the high resistance state is when the layers are antiparallel. However, the curious jumps are not easy to explain, they could possibly be due to quasi-stable magnetic domain configurations.

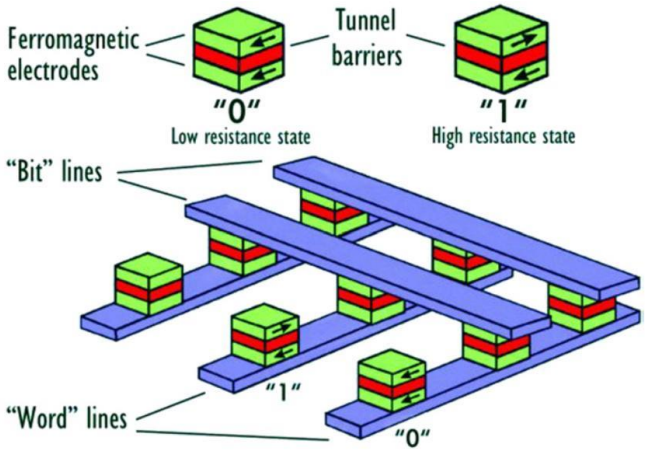


**Figure 10: Structure of MRAM [*Fert,2003*].**

Katine demonstrated how a single cell would work. Figure 10 scales this up to a full useable magnetic random access memory (MRAM) device and, by using this structure, each cell can be individually accessed. A spin current of around $10^8$ $Acm^{-2}$ can be passed through a cell aligning the layers either parallel or antiparallel. The state of the cell can then be detected by using a standard giant magnetoresistance technique. The advantages of magnetic random access memory are that it is non-volatile, has radiation hardness and is low on energy consumption.

# 2. Magnetism in Thin Films

## 2.1 Exchange Interactions

### 2.1.1 Molecular Field

The first major step forward in understanding magnetism was the work carried out by Wiess. He is sometimes referred to as the father of modern magnetism and his theories, although modified now, are still used today. He came up with insights that can only be explained by the use of Quantum Mechanics, an area of Physics which he pre-dated. According to the Langevin theory of paramagnetism, the magnetic carriers of magnetic moments in a substance are non-interacting. However, in order to explain some of the features of ferromagnetism, Wiess postulated that there was interaction between them, and he called this interaction the 'molecular field'. This could be used to explain why ferromagnets are able to spontaneously magnetise to saturation under relatively low fields. He suggested that this 'molecular field', $H_M$ , was proportional to the magnetisation and took the following form

$$H_m = \gamma M \qquad \text{Eqn. 2-1}$$

where γ is the constant of proportionality. From a non-quantum mechanical perspective, the magnetic carriers would take the form of dipoles. Given the Curie temperature of Iron is ~ $770^{O}$C this would result in an internal magnetic field of around 720T which is clearly unrealistic [*Cullity,1972*].

However, he did come up with other ideas which were accurate. For example, in order to explain the presence of unmagnetised ferromagnets, he introduced the concept of domains. Each domain has been magnetised to saturation, but the domains are randomly oriented so that the net magnetisation is zero. A greater understanding of the molecular field was only achieved with the advent of quantum mechanical exchange forces.

### 2.1.2 Direct Exchange

Heisenberg was concerned with the question of how the two electrons in a hydrogen molecule could occupy what is virtually the same space given that they were fermions. The answer was that electrons possessed a quantum state called spin and that each electron had opposite spin, this allowed them to be in the same orbital. If there are two hydrogen atoms that are close enough for there to be some over lapping of the electron orbits then the electrons can both be in the same spin state, but this results in the two atoms being in a higher energy state.

This variation in energy state is called the exchange energy, the name comes from the fact that the electrons are able to exchange position. As it is also due to an interaction between electrons, it is electrostatic in nature. The value ($E_X$) is given by Equation 2-2 where $S_i$ and $S_j$ are the spins of two electrons and $J_{EX}$ is the exchange integral.

$$E_X = -2J_{EX}\boldsymbol{S_i} \cdot \boldsymbol{S_j} \qquad \text{Eqn. 2-2}$$

This exchange energy is the quantum mechanical origin of Wiess' molecular field and can be used to explain many aspects of magnetism. However, the influence and effect of this energy is determined by the values of the exchange integral, and in here lies some problems. The above equation only relates to a two electron system and even now it has not been successfully extended to a giant crystal of iron without any impurities even with modern day computers.

However, there have been a number attempts to solve the exchange energy equation for large systems using various assumptions which are used in order to simplify the maths. Exchange forces only act over short distances as they follow a $1/r^6$ law, so by making the assumption that these only interact with nearest

neighbour atoms, the complexity of the solution is reduced. One of the more successful of these solutions is the one which has become known as the Bethe-Slater Curve. Its success is based on the fact that it is able to predict the magnetic properties a number of elements (Figure 11).

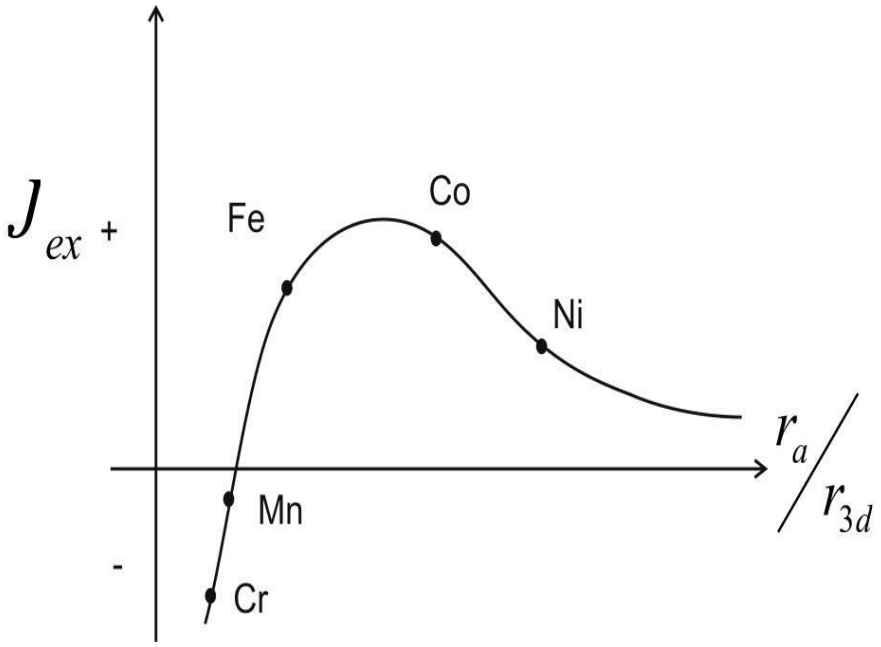


**Figure 11: Bethe-Slater Curve [*Cullity,1972*].**

The curve shows the variation of the exchange integral with the ratio $r_a$ / $r_{3d}$, where $r_a$ is the radius of an atom and $r_{3d}$ is the radius of the *3d* shell of electrons. Whether the exchange integral is positive or negative relates to whether the element is ferromagnetic or anti-ferromagnetic, and the size of exchange integral relates to either the Curie temperature or Néel temperature. When the distances between the atoms are the same as that in the figure, Chromium has a higher Néel temperature than Manganese and Cobalt has the highest Curie temperature of the ferromagnets. Above these temperatures, the thermal energy over comes the exchange energy and they all become paramagnetic.

### 2.1.3 Indirect Exchange

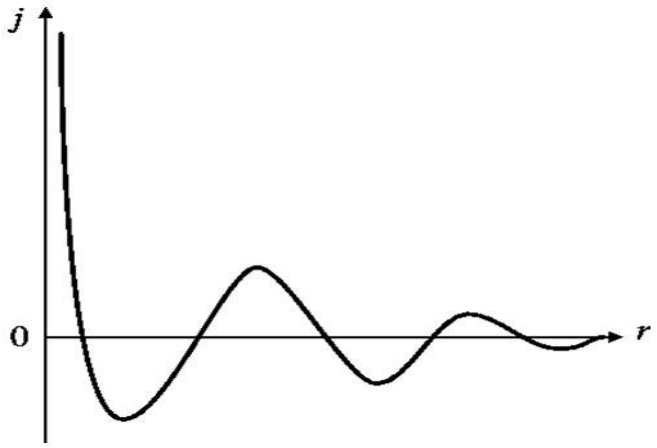


**Figure 12: Variation of RKKY interaction [*O'Handley,2000*].**

.

As is often the case in magnetism, one theory may well be able to explain one effect but not another and another question in magnetism that needed to be answered was why rare earth metals and alloys were magnetic. Although the underlying reason is similar to the Bethe-Slater Curve, there is actually a different physical explanation which can be introduced here in order to explain this. The exchange force considered in the Bethe-Slater Curve is only over very short distances such as nearest neighbour atoms, hence it is called a direct exchange. The force that explains why rare earth metals are magnetic acts of over much longer distances and is called an indirect force.

The magnetic moment of a rare earth metal is due to the spin state of electrons in the *4f* orbital, but the radius of the *4f* orbital is only about 10% of the interatomic spacing [*O'Handley,2000*]. However, the polarised electrons in this *4f* orbital interact with the conduction electrons in the $5d^1$ and $6s^2$ bands. The now weakly polarised conduction electrons have an extended wave function and therefore interact with *4f* electrons at other atomic sites, this indirect exchange is called RKKY interaction. Returning to the exchange integral, calculations can now be performed which predict its value for different atomic spacing (Figure 12). Depending on these values the material can either be ferromagnetic, antiferromagnetic or helimagnetic.

### 2.1.4 Super Exchange

There is also a third from of exchange interaction which results in antiferromagnetism. Like direct exchange, the basis of it is the Pauli Exclusion Principle, however, unlike direct exchange, magnetic sites are not nearest neighbours, instead there is an oxide ion that lies in-between two transition metals ions.

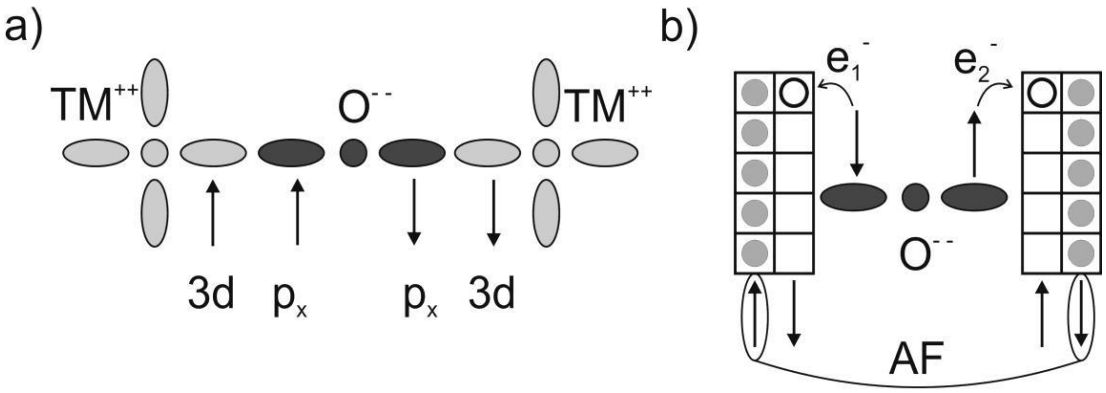


**Figure 13: Superexchange mechanisms in transitions metal oxides (***Figure a shows the relative location of the orbits. Figure b shows how the electrons take up an antiferromagnetic state)***.**

The 3*d* orbitals of the transition metals are half occupied, but after the transfer of electrons to the Oxygen atom, its outer orbital is completely full. Due to the Pauli Exclusion Principle, these electrons must take up opposite spins. If electrons are now exchanged between the oxygen ion and the transition metal, their spin must be conserved, this then results in effectively an antiferromagnetic coupling between the transition metals and is referred to as superexchange (Figure 13). Cobalt Oxide is a good example of this kind of antiferromagnet as it was this material which first demonstrated exchange bias (see section 3.1.1).

### 2.1.5 Interlayer Coupling

The paper that Fert published [*Baibich,1988*] which presented the results of GMR used Iron/Chromium magnetic superlattices. By either applying or removing a magnetic field, the Fe layers would either align parallel or anti-parallel, and the resistance would change accordingly. This was an example of antiferromagnetic coupling between two ferromagnetic layers with a spacer.

This antiferromagnetic behaviour was also demonstrated by *Parkin et. al*. where he varied the thickness of the spacer [*Parkin,1990*]. The experiment was based on a trilayer system where a spacer layer of Ruthenium of varying thickness was inserted between two layers of Cobalt. The sample was then tested to find out how large a field was required in order to saturate it. There was a significant variation in this field as the Ruthenium's thickness varied (Figure 14).

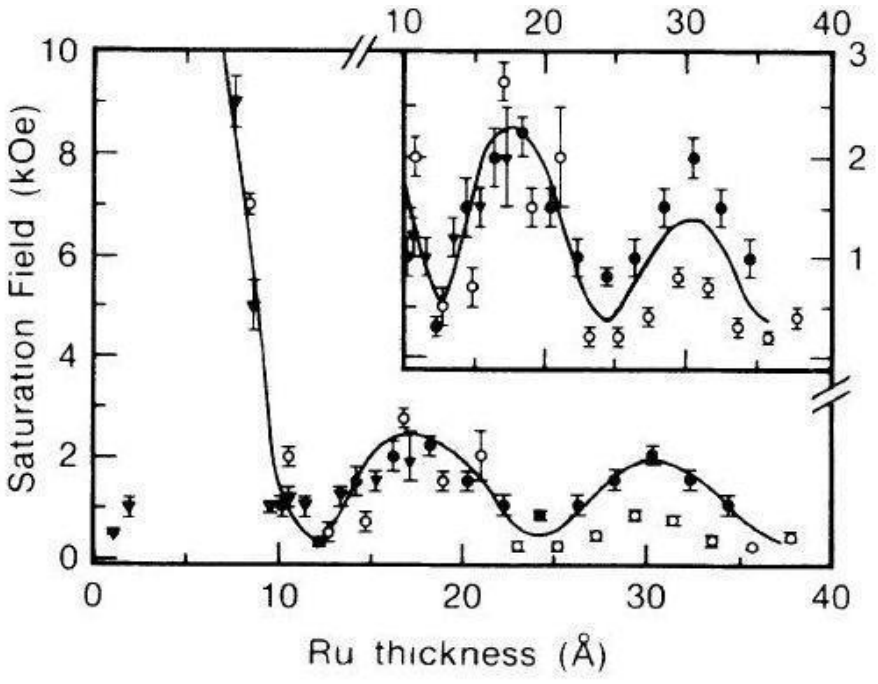


**Figure 14: Variation of interlayer exchange coupling in Co/Ru multilayers with varying Ru thickness [*Parkin,1990*].**

This was explained as being due to a change in the coupling between the two layers with the nature of the interlay coupling varying from ferromagnetic to antiferromagnetic. In terms of an exchange integral, its value is oscillating from positive to negative. The form of the exchange integral (Equation 2-3) is similar to that of direct exchange

$$E_X = -J_{EX}\, A\, \boldsymbol{M_1} \cdot \boldsymbol{M_2} \qquad \text{Eqn. 2-3}$$

where $\boldsymbol{M_1}$ and $\boldsymbol{M_2}$ are the magnetisations of the ferromagnetic layers and $A$ is the area. The reason for the oscillation is that the spacer layer acts as a potential well for the conduction electrons. These electrons will experience different probabilities of transmission or reflection within the potential well walls depending on their energy.

A conduction electron whose spin is parallel to the magnetisation of the Cobalt will experience a different energy barrier to one whose spin is anti-parallel. Therefore, as the spacer layer thickness varies along with the height of the potential wall, either antiferromagnetic or ferromagnetic coupling will be favoured depending on the spin and energy of the electron.

### 2.1.6 Inter Granular Coupling

The exchange bias samples in this project typically consist of a ferromagnet deposited on an antiferromagnet. They are grown in a sputtering system (see section 5.1.2) and the resulting bilayers are known to be granular (Figure 15). For the Cobalt Iron layer the atomic magnetic sites within a grain experience direct exchange and so, according to the Bethe-Slater Curve, all the moments will be aligned.

In Cobalt Iron, RKKY interaction results in indirect exchange between the grains. Reversal mechanisms then occur by a nucleation site which reverses first, usually at corner where the demagnetisation field is strongest, and then, by virtue of RKKY interaction, the rest of the layer reverses by domain wall motion.

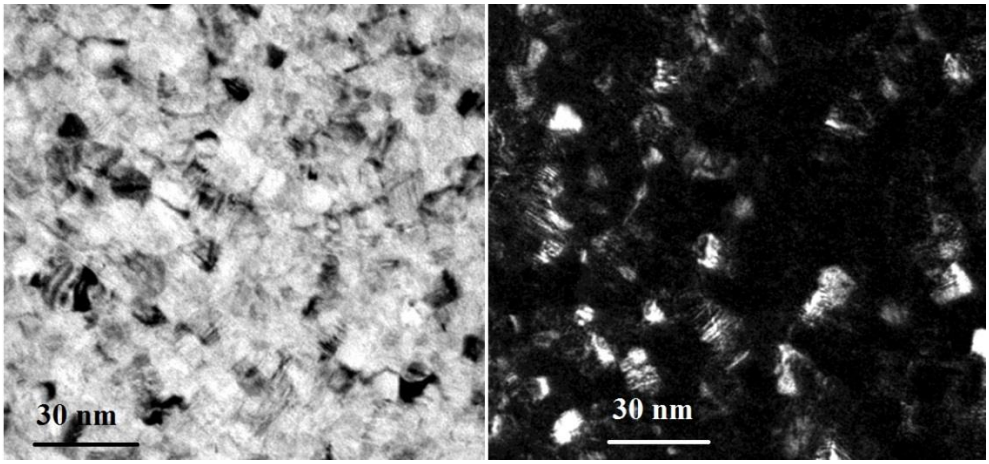


**Figure 15: Bright field and dark field images of typical exchange bias sample consisting of CoFe and IrMn.**

The antiferromagnet also consists of grains which are ordered. These ordered regions, when examined under a TEM, obey the Bragg Diffraction Law (see section 5.4.3) and appear black in a bright field image (Figure 15). If a dark field image is taken, all of the disordered region now appears black, however, only the grains that are orientated in a certain direction appear as white. As can be seen in the images, there are more black grains in the bright field image than there are white ones in the dark field image. This means that the grains have an angular distribution within the sample. The result of this distribution is that there is no possibility of the type of coupling described by Parkin as adjacent grains are very unlikely to be oriented in the same direction and they are a reasonable distance from each other. There is also no possibility of RKKY interaction as an antiferromagnetic grain does not have a net magnetic moment. It is for these reasons that in the model proposed by *O'Grady et al.* (section 4.1) the assumption is made that there is no intergranular coupling in the antiferromagnet.

.

## 2.2 Magnetic Domains in Cobalt Iron

### 2.2.1 Domain Structures

Wiess not only postulated why materials were magnetic, he also wondered why it was possible for ferromagnetic materials not to be magnetised even though they possessed, what he called, the molecular field. The answer he came up with was that the material was still magnetised but that this magnetisation occurred in regions, or domains, whose orientation was random. This would then mean that the net magnetisation was zero.

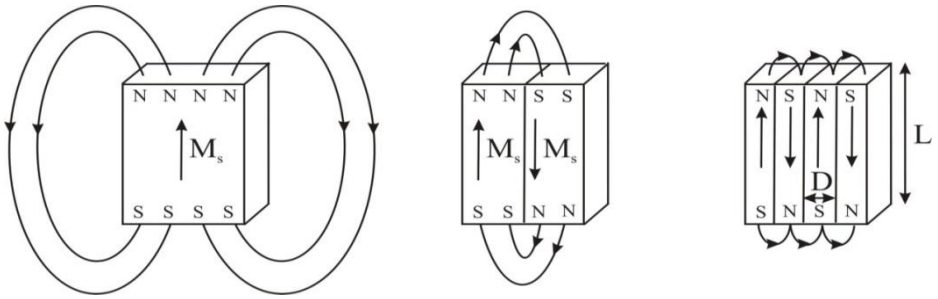


**Figure 16: Division into domains [*Cullity,1972*].**

Below its Curie temperature, an 'unmagnetised' ferromagnet is actually in its lowest energy state. This is because domains form in order to minimise the magnetostatic energy (Figure 16). There are a number of energetic balances going on here. Clearly, the smaller the domains, the lower the magnetostatic energy, however, a domain wall costs energy because throughout the wall, magnetic moments are not aligning parallel. Within the wall lie other energetic balances. Not only does the exchange force want to align all moments parallel but there is also an anisotropic energy cost in taking the moment out of the plane of its easy axis. Both of these effect the size of the domain wall, which in turn affects the overall size of the domains. For bulk Cobalt a typical domain width would be around $10^{-3}$ cm [*Cullity,1972*].

### 2.2.2 Néel and Bloch Walls

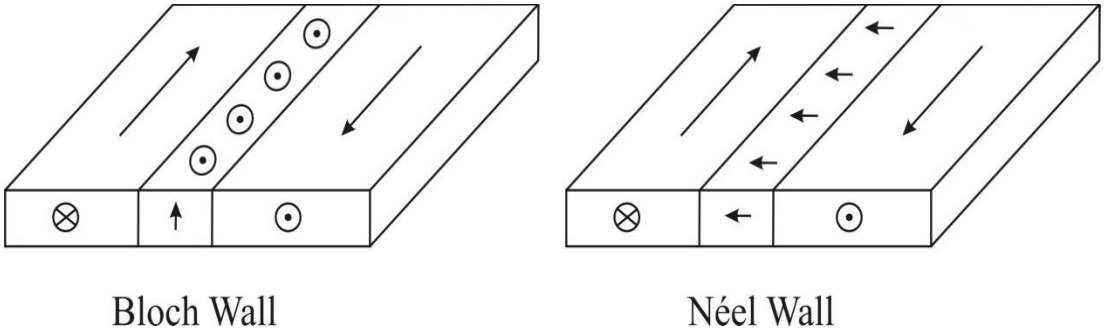


**Figure 17: Directions of rotation of magnetic moment for Bloch walls and Néel walls.**

There are two types of domain walls, Bloch walls and Néel walls. With the Bloch walls the moment rotates out of the plane of the sample, with Néel walls the moment rotates in the plane of the sample (Figure 17). Given that the Cobalt Iron layers are usually around 2nm in the samples grown for this project, the Néel wall is much preferred as the energy required to rotate a moment perpendicular in such a thin sample is significantly higher than keeping the moment in plane (Figure 18).

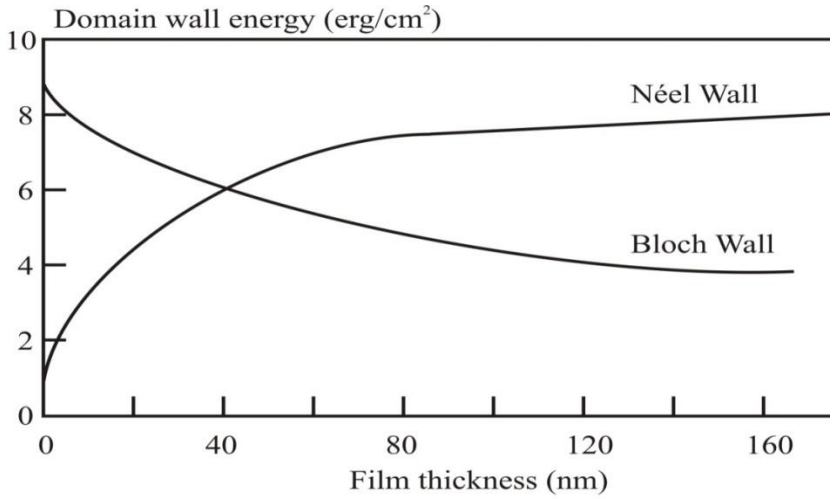


**Figure 18: Energy per unit thickness of a Bloch wall and a Néel wall as a function of film thickness [*O'Handley,2000*].**

## 2.3 Anisotropy

### 2.3.1 Magnetocrystalline Anisotropy

Anisotropy is when a property or characteristic behaves differently in different directions, as opposed to isotropy which is when a property behaves the same in different directions. The following section will examine different types of magnetic anisotropies. The first one to be discussed will be the most important one, an intrinsic anisotropy, afterwards a few extrinsic anisotropies will be covered.

The crystallographic structure of a material influences the orbits of the electrons. The spins of the electrons are coupled to their orbits by spin-orbit coupling. The combination of these interactions results in the spins of the electrons preferentially aligning in a certain direction. This direction is called the easy axis and a material will saturate more readily in this direction than in any other. In order to saturate the material in another direction this spin-orbit coupling needs to be overcome, however, this coupling is relatively weak.

The easy axis is not always simple to predict for example in *bcc* Iron, the easy axis is <100> and the hard axis is <111> whereas in *fcc* Nickel the easy axis is <111> and the hard axis is <100>. In this project, both Cobalt Iron and Iridium Manganese are cubic. The energy required to magnetise a cubic material in a given direction ($E_K$) is given by

$$E_K = K_O + K_1(\propto_1\propto_2+\propto_2\propto_3+\propto_3\propto_1)+ K_1(\propto_1\propto_2\propto_3) +\ldots \qquad \text{Eqn. 2-4}$$

where $K_O$, $K_1$ and $K_2$ are anisotropy constants for a given material and $\alpha_1$, $\alpha_2$ and $\alpha_3$ are cosines of the angles between the saturation magnetisation $M_S$ and the crystal axes.

Jung [*Jung,2003*] carried out anisotropy measurements on 50nm of Cobalt Iron sputtered on to various seed layers such as Copper, Tantalum and Ruthenium, he found that the uniaxial anisotropy for the Copper seed layer was $2.4 \times 10^4$ergs/cc. It is assumed that the characteristics of the Cobalt Iron layers in this project are similar to this. The work by carried out by *O'Grady et al*. proposes a method to calculate the anisotropy of Iridium Manganese in thin film sputtered materials, the theory behind this is explained in section 4.1.

### 2.3.2 Shape Anisotropy

Shape anisotropy is due to the formation of uncompensated free poles at the surface of a magnetised material. These free poles generate the demagnetisation field, a field which tends to reduce the total magnetisation of the sample. The field is given by the following equation

$$\boldsymbol{H}_{\mathrm{D}} = -N_D \boldsymbol{M}_S \qquad \text{Eqn. 2-5}$$

where $\boldsymbol{H_D}$ is the demagnetising field, $\boldsymbol{M_S}$ is the saturation magnetisation, and $N_{\mathrm{D}}$ is the demagnetising factor. $N_D$ can vary between 0 and $4\pi$ and is a function of the shape of the material. The size of the demagnetising factor is inversely proportional to the separation of the free poles. Hence, in a sample whose dimensions are 5mm x 5mm x 2nm, it would be very difficult to magnetise the sample out of the plane. Demagnetisation fields are still important though as they will be high at the corners of a magnetised ferromagnetic sample with the above dimensions which is experiencing a reverse field. Thus, it is usually the corners that are the nucleation sites for the magnetic reversal process.

### 2.3.3 Stress Anisotropy

A further form of anisotropy is called stress anisotropy. If a magnetic field is applied then, due to the spin-orbit coupling, the crystallographic electrostatic field is changed, this affects the positions of the atomic sites and the dimensions of the material change. Correspondingly, the act of stress on a ferromagnetic material can vary the magnetisation of that material. However, no stress was applied to the samples during this project.

## 2.4 Antiferromagnets

### 2.4.1 Susceptibility of Antiferromagnets

The first papers published which studied antiferromagnets were authored by L. Néel [*Neel,1932*] and the work was based on susceptibility measurements. Figure 19 shows the temperature dependence susceptibly of an antiferromagnet ($\chi$). The first thing to note is that the susceptibility shows a maximum at a temperature that became known as the Néel temperature. Above this value the magnetic behaviour is paramagnetic in nature. This is proven by plotting the inverse of the susceptibility and noting that it is a straight line. However, in this region, the antiferromagnet does not behave as an ideal paramagnetic because of the influence of exchange interactions.

Below the Néel temperature the thermal energy is reduced to a point where these exchange interactions can take dominance. Here, the susceptibly reduces significantly, although never to zero.

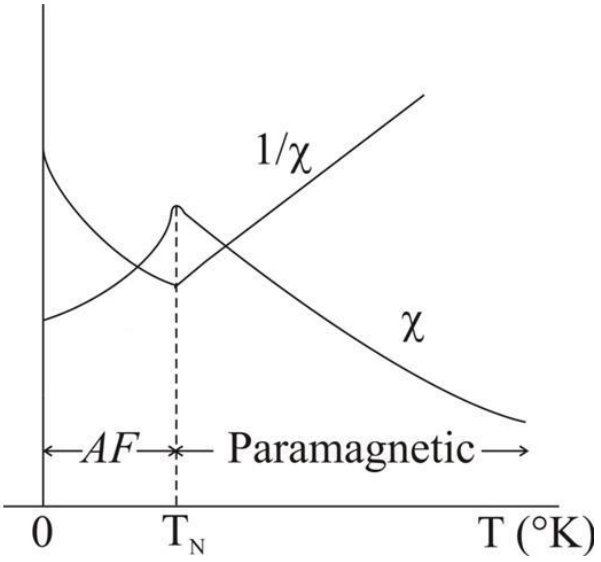


**Figure 19: Variation of χ with temperature as material changes from paramagnetic to antiferromagnetic [*Jiles,1991*].**

### 2.4.2 Sublattices of Antiferromagnets

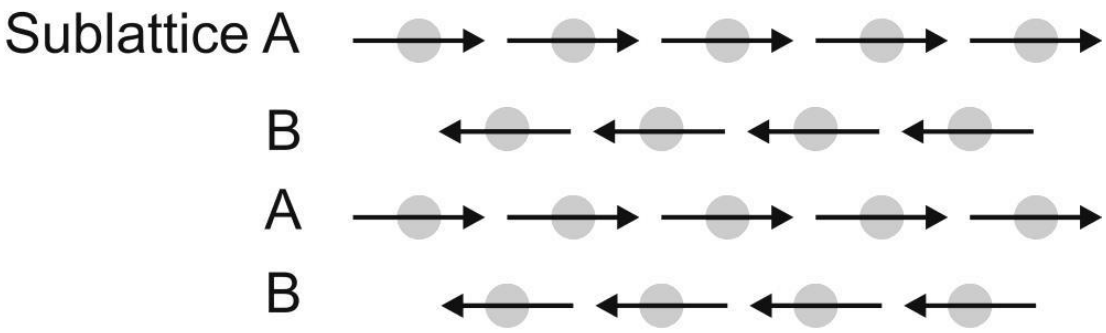


**Figure 20: Structure of sub-lattices in IrMn.**

Néel predicted what was causing this behaviour and he explained it as being due to adjacent magnetic sub-lattices arranging themselves in opposite directions, as in Figure 20. In terms of the molecular field, this can be explained as one sub-lattice acting on the other by the following equations

$$H_{mA} = -\gamma M_B \qquad \text{Eqn. 2-6}$$

and

$$H_{mB} = -\gamma M_A \qquad \text{Eqn. 2-7}$$

where $M_A$ and $M_B$ are the magnetisations of sublattice '*A*' and '*B*' respectively and $H_{mA}$ and $H_{mB}$ are the molecular fields experienced. The source of the negative sign in the equations can be linked back to the Beth-Slater curve where in certain circumstances the exchange integral is negative.

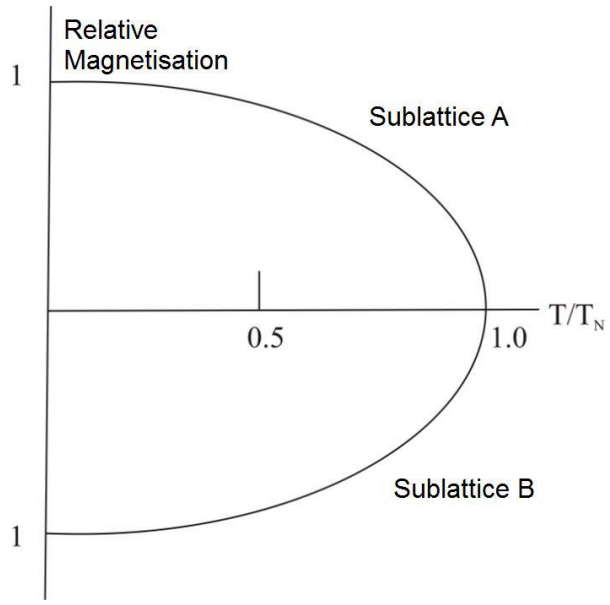


**Figure 21: Temperature variation of sub-lattice magnetisation [*Crangle,1991*].**

Figure 21 shows the temperature variation of the magnetisation of the sub-lattices. As can be seen, as the temperature decreases below the Néel temperature, the system tends towards a purely antiferromagnetic state at a rate which corresponds to the decrease in susceptibility as seen in Figure 19. However, in a real system zero susceptibility is never reached due to imperfections and impurities.

### 2.4.3 Spin Structure of Antiferromagnets

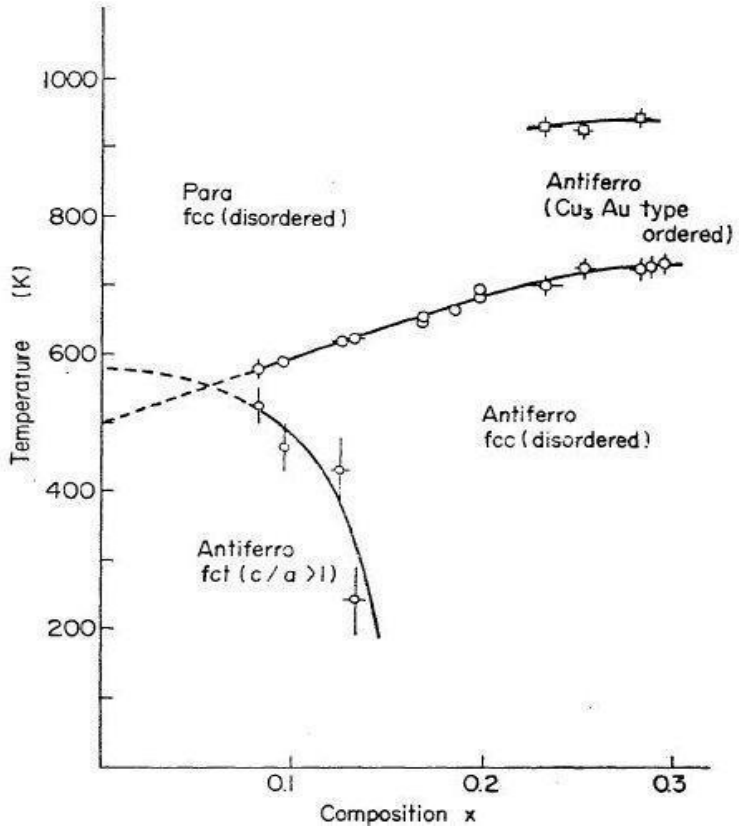


**Figure 22: Néel temperature for various phases of $Ir_xMn_{1-x}$ alloy system [*Yamaoka,1974*].**

In 1974 Yamaoka [*Yamaoka,1974*] carried out extensive characterisation of the Néel temperature of Iridium Manganese in it's different phases as a function of composition. The composition took the form of $Ir_xMn_{1-x}$ where x ranged from 0.1 to 0.3. The region of most interest is that where x varies from 0.2 to 0.3. The composition can take the form of either an ordered phase where the structure is shown in Figure 23 or it can take disordered phases shown in Figure 24. As can be seen from Figure 22, an increase in the percentage of Iridium gradually increases the Néel temperature, but the change from the disordered phase to the ordered phase significantly increases it.

The spin structure of the ordered phase takes up one form, whereas the spin structure of the disordered phase can take three different forms, 1Q, 2Q and 3Q. It is thought that different phases contribute differently to exchange bias effects and although neutron studies are able to identify the 2Q state, it is unable to separate the 1Q and 3Q states [*Sakuma,2003*].

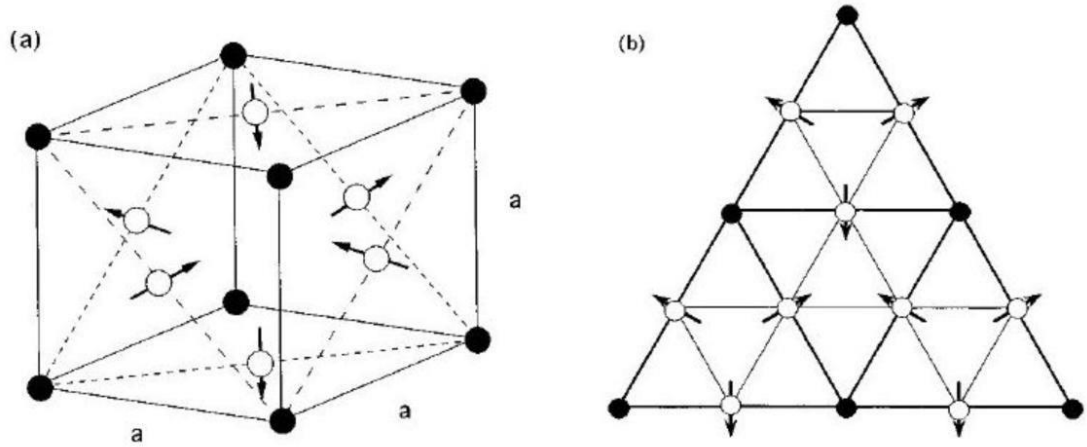


**Figure 23: Spin structure of ordered $IrMn_3$ phase** *(The black circles are Ir, the white circles indicate Mn)* **[*Tomeno,1999*].**

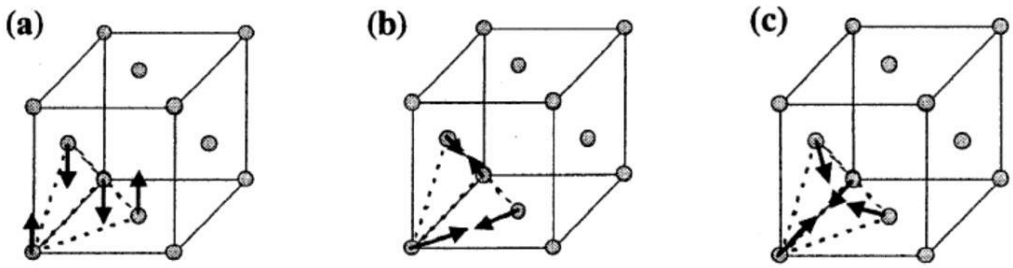


**Figure 24: 1Q (a), 2Q (b), 3Q (c), spin structures for IrMn disordered phase** *(The circles at the vertices locate the Ir, the face centred circles are Mn)* **[*Sakuma,2003*].**

Imakita [*Imakita,2004*] experimented with substrate heating of up to 200°C during deposition and annealing of up to 400°C post deposition. This resulted in a significant increase in the exchange bias and they attributed this to the presence of the ordered phase. All of this means that the state of the Iridium Manganese is highly dependent on its composition and the seed layer upon which it is grown, and there are probably a variety of phases present in any one sample. As it is impossible to carry out neutron diffraction on a single layered thin film, it is impossible to know exactly which form the spins take. This means that the research carried out in this area has to be done so in a more indirect manner.

# 3. Models of Exchange Bias

## 3.1 Early Models

### 3.1.1 Meiklejohn and Bean

It was in 1956 [*Meiklejohn and Bean,1957*] that the phenomenon of exchange bias was first reported. The group was growing Cobalt particles with an applied field in order to induce an easy axis. The process of extraction required the particles to be oxidised, however, when a hysteresis loop was taken they saw something unexpected (Figure 25), the hysteresis loop was no longer symmetric.

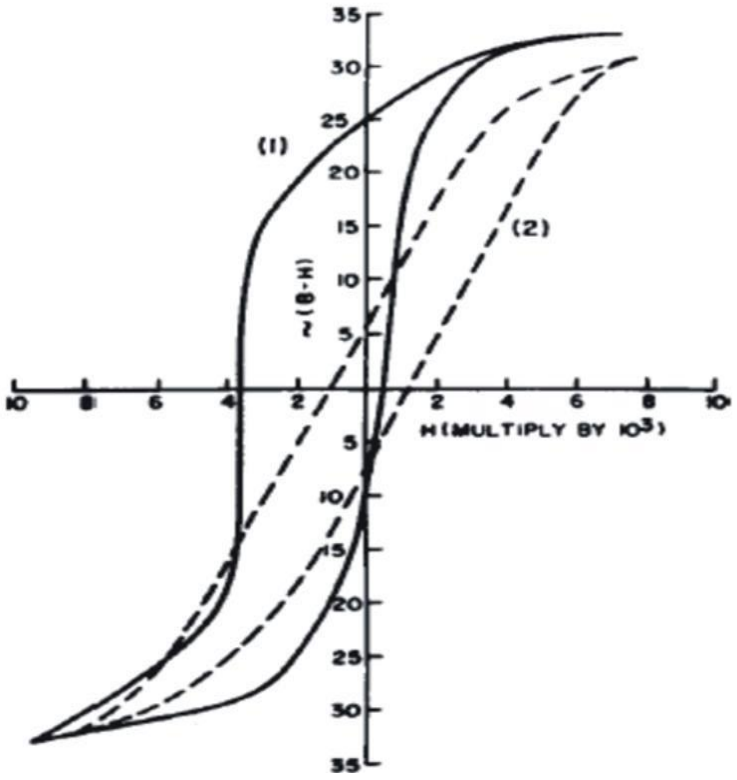


**Figure 25: Meiklejohn and Bean exchange biased loop [*Meiklejohn and Bean,1957*].**

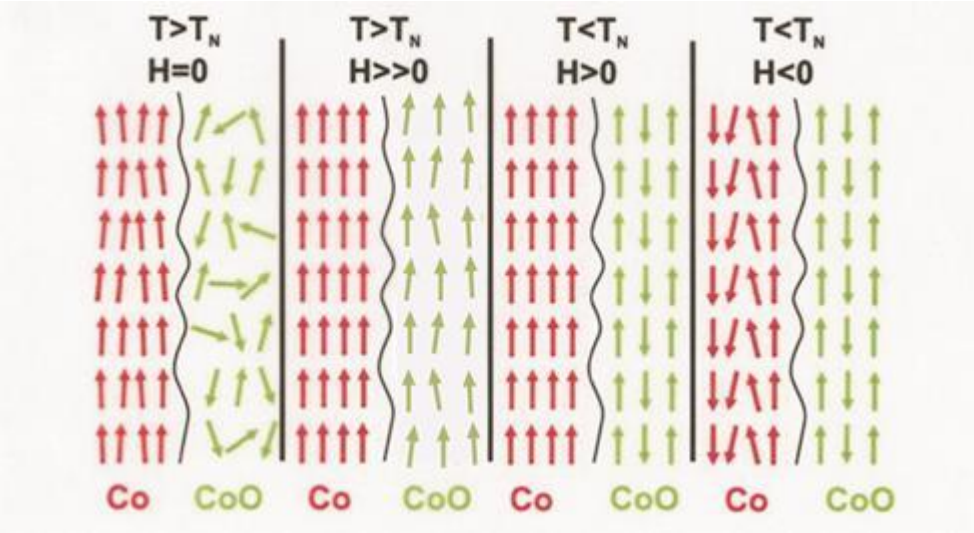


**Figure 26: Effect of field cooling Co, CoO particles.**

Figure 26 shows the experimental procedure for setting a sample in order for it to exhibit exchange bias. The sample is first heated above the Néel temperature of the antiferromagnetic Cobalt Oxide, which thermally activates it. If a large field is applied both the ferromagnetic and antiferromagnetic layer are aligned. As the sample is field cooled to below the Néel temperature the Cobalt Oxide settles into an antiferromagnetic configuration. Now the Cobalt Oxide is set, the field can be reversed which reverses the ferromagnetic Cobalt, but not the Cobalt Oxide.

Meiklejohn and Bean proposed a theory as to what might be producing this effect. Their model, although basic, was the first step towards gaining an understanding of exchange bias. They assumed that the interface between the ferromagnetic and the antiferromagnetic was perfectly smooth, the ferromagnet was in a single domain state and coupled to the antiferromagnet, and that when the ferromagnet reversed during measurement, all of the antiferromagnet spins remained fixed. They created an equation that predicted the energy per unit area of the exchange bias system.

$$E = -HM_S t_F \cos(\theta - \beta) + K_{AF} t_{AF} sin^2(\alpha) - J_{INT} \cos(\beta - \alpha) \qquad \text{Eqn. 3-1}$$

where $H$ is the applied field, $Ms$ is the saturation magnetisation of the ferromagnetic layer, $t_F$ is the thickness of the ferromagnetic layer, $K_{AF}$ is the anisotropy of the antiferromagnet, $t_{AF}$ is the thickness of the antiferromagnet and $J_{INT}$ is the interface coupling constant. The ferromagnetic and antiferromagnetic easy axis are assumed to lie along the same direction and the angles $\theta$, $\beta$ and $\alpha$ are defined as the angle between this axis and the applied field, ferromagnetic magnetisation and the antiferromagnetic magnetisation respectively (Figure 27).

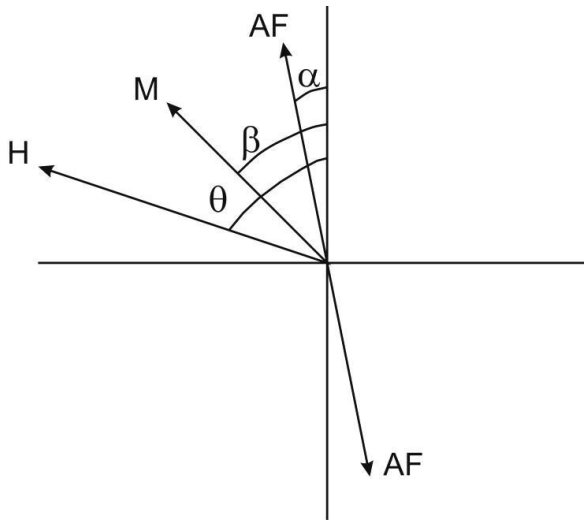


**Figure 27: Diagram of relative axis in AF.**

If the energy of the this equation is minimised it reduces to

$$H_{EX} = \frac{J_{INT}}{M_{FM} t_F} \qquad \text{Eqn. 3-2}$$

where $H_{EX}$ is the exchange bias. Unfortunately, the values of exchange bias predicted by this equation were out by about two orders of magnitude.

### 3.1.2 The Néel Model

The next main development of the understanding of exchange bias was to take into account the fact that the interface was not perfectly smooth. This was first introduced by Néel [*Néel,1967*] who suggested that there would be both compensated and uncompensated interface spins structures due to both antiferromagnet sub lattices being present at the interface (Figure 28). This spin structure would allow for irreversible changes in the interface and thus predicted the training effect. The training effect is where $H_{EX}$ reduces after repeated hysteresis measurements (see section 4.2.3). Unfortunately, the values predicted for this reduction by the model were again out by an order of magnitude. It also did not account for the effect where the value of the exchange bias would change with time.

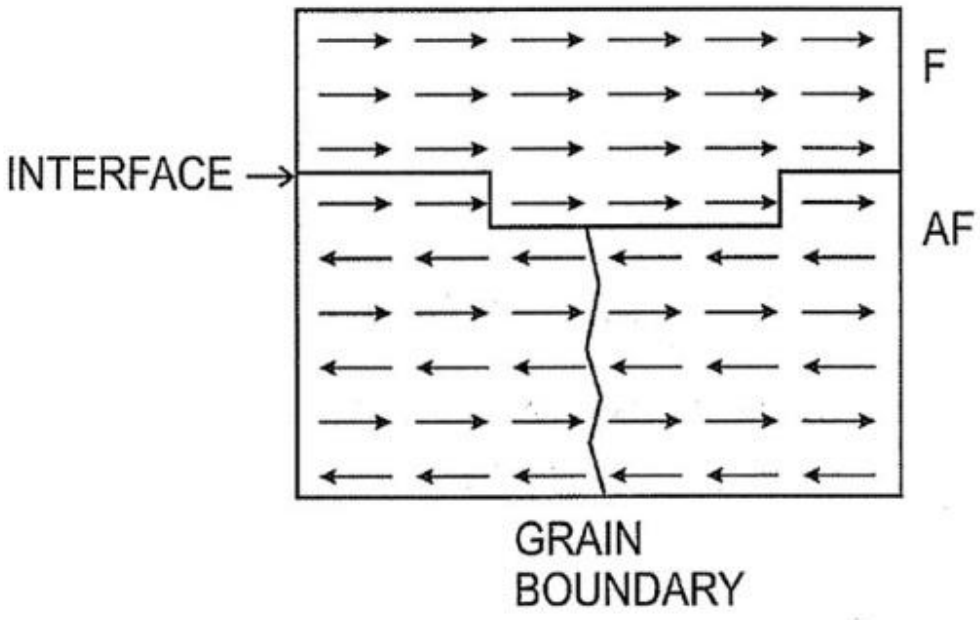


**Figure 28: Partially compensated interface due to roughness.**

## 3.2 Domain Models

There have been a series of models proposed which can be categorised as Domain Models. These all attempt to explain some of the properties of exchange bias by suggesting that there is a domain wall in the antiferromagnet. These domain walls have taken on a number of different forms, some have been parallel to the interface, some perpendicular and some cyclical. However, these models are mainly applied to single crystal systems where there is strong exchange coupling within the antiferromagnet and thus domain walls can form. The samples that were grown for this project are granular and the exchange coupling is thought to be very weak (see section 2.1.6). However, some of the work carried out using the domain model does have relevance to the polycrystalline samples used in this work.

In 2002, Shull [*Shull,2003*] published a paper which demonstrated an interesting interaction between the ferromagnetic layer and the antiferromagnetic layer. The samples were grown while a small field of 40 Oe was applied. This was done so as to induce a degree of magnetic order in the ferromagnet, but not fully saturate it. Therefore, domains were present in the ferromagnet during growth. After deposition, a magneto-optic indicator technique (MOIF) was used to map the ferromagnetic domains while no field was applied. If a field was then applied to the sample and then removed, it was seen that the domains had returned to their original positions. This was explained as the ferromagnet 'imprinting' its own domain structure on the antiferromagnet during deposition. After deposition, the state of the antiferromagnet therefore remained unchanged and, due to the exchange interaction between the layers, induced the ferromagnet to return to its original domain structure. This implies that antiferromagnetic domains can form.

### 3.2.1 Malozemoff's Random Interface Model

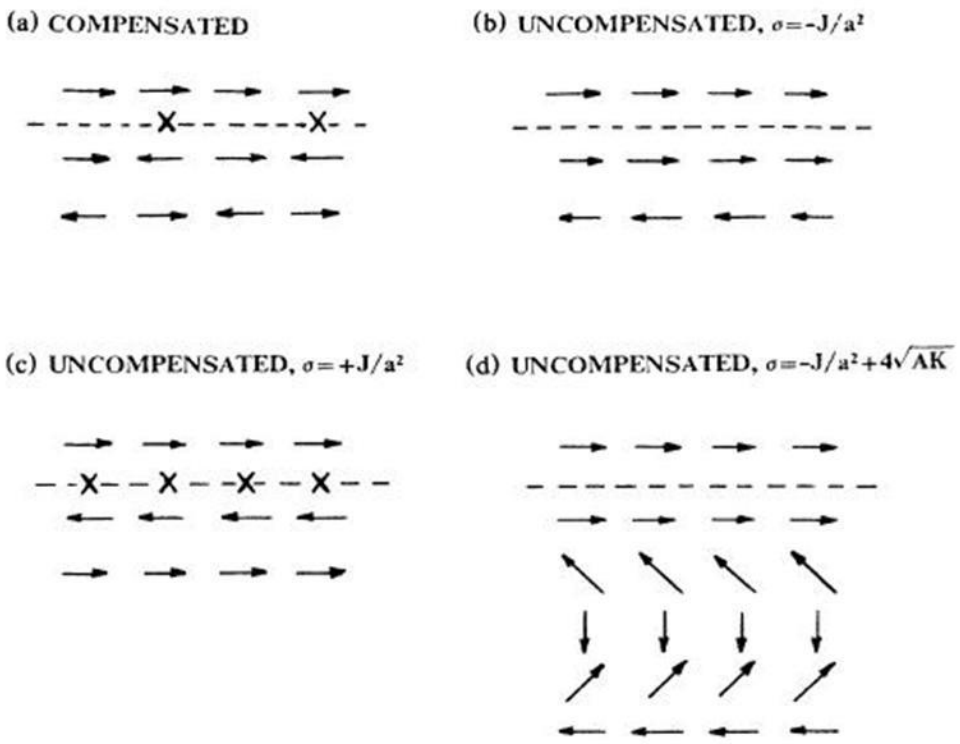


**Figure 29: Atomic moment configurations of an antiferromagnet - ferromagnetic system [*Malozemoff,1987*].**

Malozemoff incorporated the concept of random interface roughness which gives rise to a random field acting on the interface spins [*Malozemoff,1987*]. He suggested that the antiferromagnet broke up into domains whose size was determined by the competition between the exchange energy and the anisotropy energy. These domains can be seen in Figure 29 where the crosses shown represent a frustrated area of the interface. Image *b* is fully unfrustrated, image *a* is semi-unfrustrated, image *c* has a fully unfavourable interface, and image *d* shows how the energy state can be reduced by the formation of perpendicular domain walls in the antiferromagnet. To ensure the domain wall has a vertical incidence at the interface a hemispherical domain results (Figure 30).

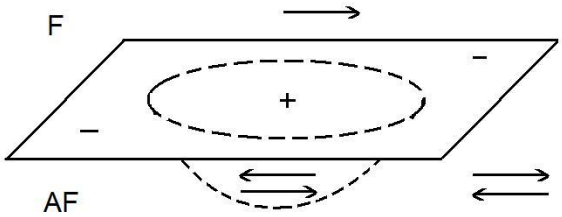


**Figure 30: Schematic of a hemispherical domain [*Malozemoff,1987*].**

The total energy of this hemisphere is equal to the interfacial energy plus the surface energy. The equilibrium size is given by

$$L \approx \pi \sqrt{\frac{A_{AF}}{K_{AF}}} \qquad \text{Eqn. 3-3}$$

where $L$ is the domain diameter, $A_{AF}$ is the exchange stiffness and $K_{AF}$ is the anisotropy of the antiferromagnet. This leads to

$$H_{EX} = \frac{2z\sqrt{A_{AF}K_{AF}}}{\pi^2 M_F t_F} \qquad \text{Eqn. 3-4}$$

as the expression for the overall exchange bias where $z$ is a dimensionless parameter describing the frustration of moments at the interface, $M_F$ is the magnetisation of the ferromagnet and $t_F$ the thickness of the ferromagnet.

This model was able to predict phenomena such as the training effect but did not take into account the size of the antiferromagnetic grains which is an important part of this study. For example, one of the assumptions was that the antiferromagnet was infinitely thick.

### 3.2.2 Domain State Model

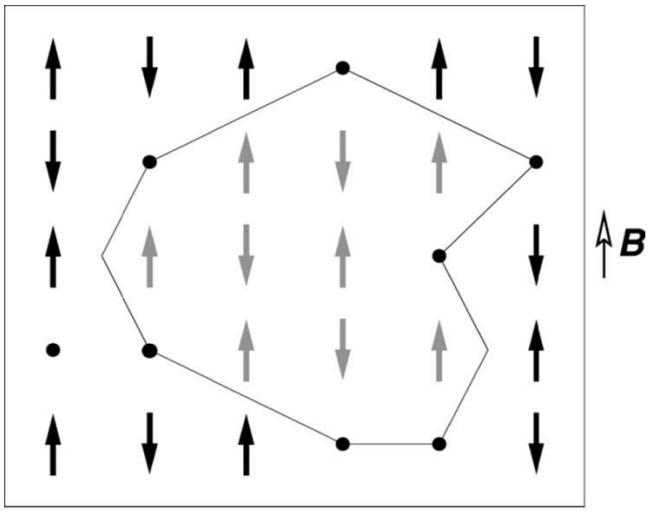


**Figure 31: Schematic of domain wall in AF.**

Nowak [*Nowak,2002*] produced more work that was based on domains forming in the antiferromagnet. The effect they were trying to explain was the increase in exchange bias when impurities were introduced into the bulk of the antiferromagnet. The theory saw domains forming in the bulk, as shown in Figure 31, where the black dots represent defects such as nonmagnetic ions or vacancies. Inside the line is one domain and outside of it is another. It can be seen that inside there are three uncompensated spins which would give the domain a net magnetization. This net magnetization then couples to the ferromagnet and results in exchange bias. The reason these impurities increase the exchange bias is because they reduce the energy required for a domain wall to form and so the domains form more readily. However, there is an issue that arises from this. The domain boundaries are represented as thin lines, implying that the domain walls are effectively one atom wide. The energy required to produce such a thin wall would make the formation of such domains highly unfavourable.

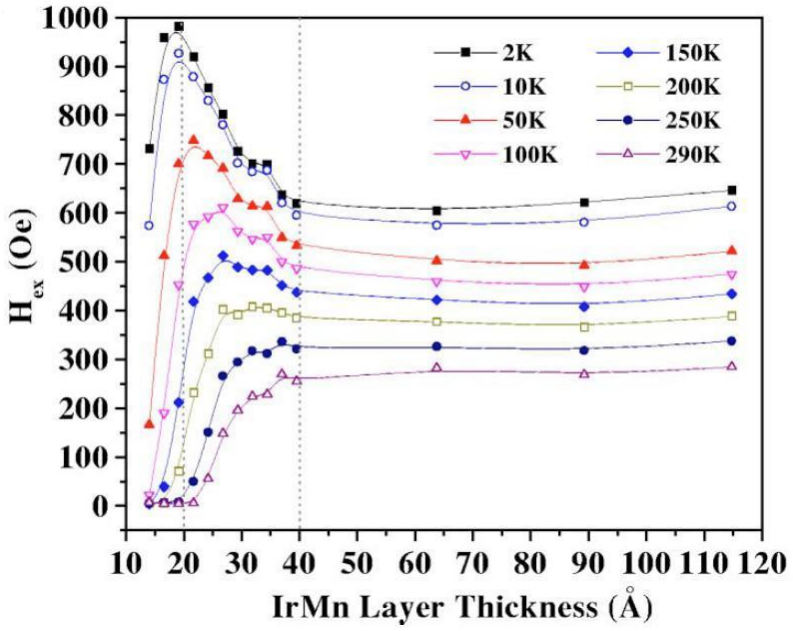


**Figure 32: IrMn thickness dependence of exchange bias field [*Ali,2003*].**

Ali [*Ali,2003*] produced a paper that was based on the domain state model whose experimental results are of relevance to the work presented in this thesis. Figure 32 shows the dependence of exchange bias on the thickness of the Iridium Manganese. The 8 different results are showing exchange bias effects at different temperatures, what is of interest, however, are the peaks shown at around 20Å. Ali attributed this peak to the ease with which a domain wall can form. At very low thickness there is not enough space for a domain wall.

'*Above this thickness the decline in $H_{EX}$ is caused by the fact that with increasing antiferromagnetic thickness it becomes more and more difficult to form domain walls since these are oriented perpendicular to the interface extending through the whole antiferromagnetic layer*'

### 3.2.3 The Model of Stamps

Stamps produced a topical review on exchange bias based on natural antiferromagnets [*Stamps,2000*]. It started off building a theoretical model from first principles based on energy stability. This led to a prediction of the coercive fields based on the interlayer exchange coupling (Equation 3-5 and Equation 3-6) and also to the well-known inverse relationship between exchange bias and ferromagnetic thickness (Equation 3-7).

$$H_{C1} = \frac{2K_F + J}{Mt_F} \qquad \text{Eqn. 3-5}$$

$$H_{C2} = \frac{2K_f - J}{Mt_F} \qquad \text{Eqn. 3-6}$$

$$H_{EX} = \frac{J}{Mt_F} \qquad \text{Eqn. 3-7}$$

$H_{C1}$ and $H_{C2}$ are the coercive fields, $J$ is the interlayer exchange and $K_F$ is the anisotropy of the ferromagnet

Next Stamps' paper moved onto calculating the energy in a twisted domain wall within a ferromagnetic chain. It then considered a chain of antiferromagnetic coupled moments connected to the ferromagnetic chain by an exchange energy. This represented the interface of the bilayer and by twisting these chains, partial domain walls could form. An interesting artefact of this partial domain wall was that the ferromagnet could align perpendicular to the antiferromagnetic easy axis. In this situation extra terms have to be considered in the energy equation, but by doing so it is possible to predict exchange bias in a fully compensated system. The

model then extended to more complex situations where both sublattices are present at the interface (Figure 33). However, the samples used in this project are not natural antiferromagnets, nor single crystal, but instead are granular.

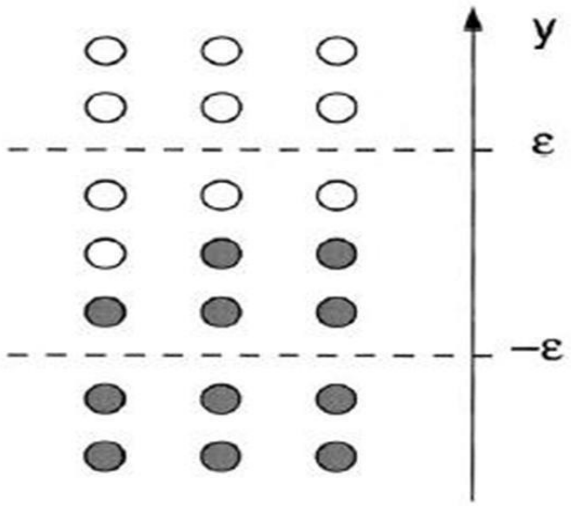


**Figure 33: Interface region of ferromagnet and antiferromagnet [*Stamps,2000*].**

### 3.2.4 The Model of Stiles and McMichael

Stiles and McMichael's model bridges the concept of domain models and the granular models as it assumes a granular antiferromagnet which contains a domain wall [*Stiles and McMicheal,1999(a),(b),2001*]. Their model is based on the following equation

$$\frac{E}{Na^2} = \frac{-J_{net}}{a^2}\left[\hat{M}_{FM}\cdot\hat{m}(0)\right] + \frac{J_{sf}}{a^2}\left[\hat{M}_{FM}\cdot\hat{m}(0)\right]^2 + \frac{-\sigma}{2}\left[1-\hat{m}(0)\cdot(\pm\hat{u})\right] \qquad \text{Eqn. 3-8}$$

where $E$ is the energy of a grain coupled to the ferromagnet, $N$ is the number of spins at the interface, $a$ is the lattice constant, $J_{net}$ is the direct coupling, $J_{sf}$ is the spin-flop coupling, $\sigma$ is the energy of a 180 degree domain wall in the antiferromagnet, $\boldsymbol{M}_{FM}$ is the direction of the ferromagnet magnetisation, $\boldsymbol{m}(0)$ is the net sublattice magnetisation direction at the interface and $\pm\boldsymbol{u}$ are the two easy directions of the uniaxial anisotropy in the antiferromagnet. The first term describes the direct coupling at the interface and is a reduced value from the standard exchange integral. The second term is the spin-flop coupling. A spin-flop transition occurs in an antiferromagnet when, due to a weak anisotropy, the two magnetic sublattices in the presence of an applied field rotate perpendicular to both the applied field and easy axis of the material. Koon [*Koon,1997*] had borrowed this term to describe the interfacial exchange coupling that occurs when there is a perpendicular orientation between the magnetic moments of the ferromagnet and antiferromagnet. The third term is the energy of the partial domain wall which is wound through an angle.

Figure 34 shows an antiferromagnetic grain with a ferromagnetic layer on the top. As the direction of magnetisation of the ferromagnet is rotated, a partial domain wall is wound up in the antiferromagnet. The manner of the coupling between the ferromagnet and antiferromagnet is assumed to be both direct and spin-flop. Unlike some of the domain wall models where the domain wall is assumed to be infinitely thin which then implies an infinitely large anisotropy, the domain wall width here is more realistically of finite thickness.

The model of Stiles and McMichael suggested that there were a number of complex processes taking place during the measurement of a hysteresis loop. Initially, some of the grains would go through reversible transitions as the field was reversed and some would go through irreversible transitions. There was also a difference in the reversal process for the case of the field increasing and the field decreasing. When the field is increasing, the ferromagnet is exerting a torque on

the antiferromagnet, whereas when the field is decreasing it is the antiferromagnet exerting a torque on the ferromagnet.

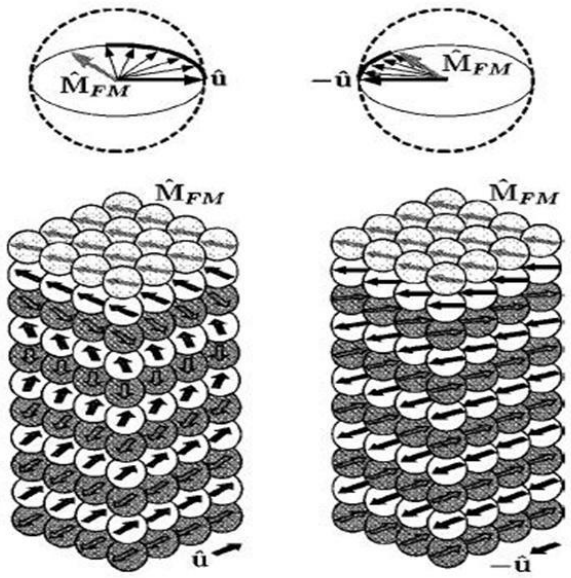


**Figure 34: Two configurations of an antiferromagnet grain coupled to a ferromagnet layer [*Stiles,1999*].**

There are a number of assumptions in the model, some of which can be applied to the materials used in this thesis, and some which cannot. One of the assumptions was that the ferromagnet was coupled to independent grains and the stability of these grains was temperature dependent, this is shared with the model proposed by O'Grady. Another assumption was that, although there could be a twisted domain wall in the antiferromagnet, the grains could not be multidomain. One of the differences is that Stiles and McMichael assumed a perfectly flat interface and this, unfortunately, does not allow for the possibility of spin clusters, which is the main topic of this work.

## 3.3 Granular Models

### 3.3.1 The Thermal Fluctuation Aftereffect Model

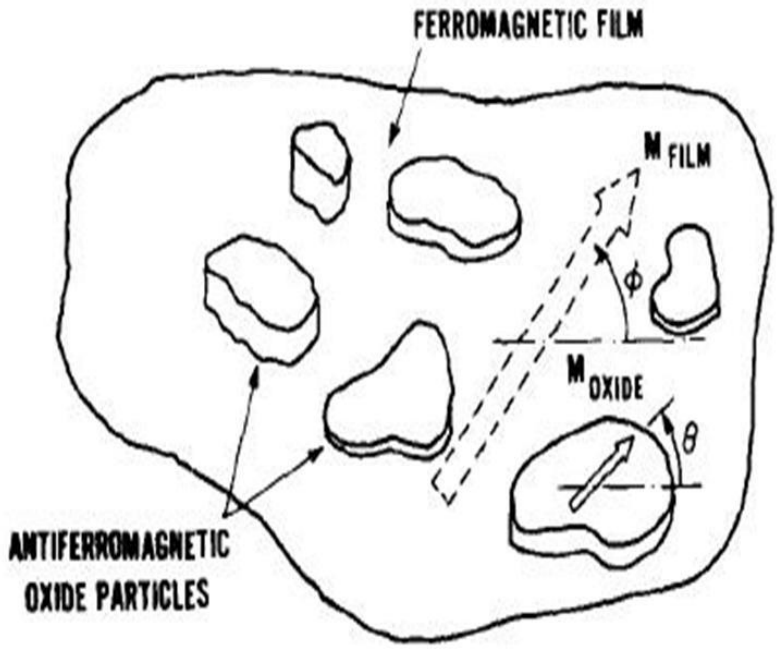


**Figure 35: Antiferromagnet particles coupled to underlying ferromagnet [*Fulcomer,1972*].**

While the various domain models were being developed, Fulcomer and Charap developed the Thermal Fluctuation Model [*Fulcomer and Charap,1972*] based on Stoner-Wohlfarth theory [*Stoner,1948*]. The main difference between this and the domain state models at the time was that this work was based on the assumption that the antiferromagnet is an assembly of non-interacting particles. The actual samples used to compare the theory with experiment were oxidised Nickel Iron films where the oxide was in the form of small discrete particles whereby no interaction between them was possible (Figure 35). It also attempted to explain some of the time dependent effects in terms of thermal activation which was an approach that the domain state models were not taking.

One of the interesting measurements they took was how the exchange bias would vary with temperature. It was found that the exchange bias would decrease as temperature increased up to a value they called the blocking temperature ($T_B$), at which point the exchange bias would reduce to zero. The curious aspect of this was that this temperature was noticeably lower than the Néel temperature. Their explanation for this was that the Blocking temperature had been reached when the largest antiferromagnetic grain had become randomly oriented. They made one assumption that is particularly important in the context of the O'Grady model;

'*We assume that the distribution of the area, thickness and contact fraction is such that all areas are equally probable up to some maximum area and that there are no larger particles, and further that the distribution of thickness and contact fraction are of a similar nature.'.*

Section 4.1.4 will detail how *O'Grady's* model differs from this. Further studies were carried out using the thermal fluctuation model. Some were able to predict the exchange bias and coercivity as a function of temperature [*Grimsditch,2003*], others investigated Nickel Iron / Iron Manganese systems [*Nishioka,1996*] and Cobalt/ Chromium Manganese Platinum systems [*Nishioka,1998*] and some even predicted the temperature dependence of the blocking temperature [*Xi,2005*]. Again, none of these systems is appropriate to the work carried out in this project as they do not relate to polycrystalline samples whose grain size follows a log normal distribution.

### 3.3.2 Calculations of Van der Heijden

An extension of this model was carried out by van der Heijden [*van der Heijden,1998*] Here, instead of just measuring the exchange bias as a function of temperature, they measured it as a function of time at various temperatures with the sample having the ferromagnetic layer reversed (Figure 36). They found that the decease of exchange bias increases with temperature and they interpreted it as a thermally assisted reversal of magnetic domains in the antiferromagnetic layer. There was even reversal of the exchange bias. In some ways this experiment is a precursor to the work of *O'Grady* (section 4.1).

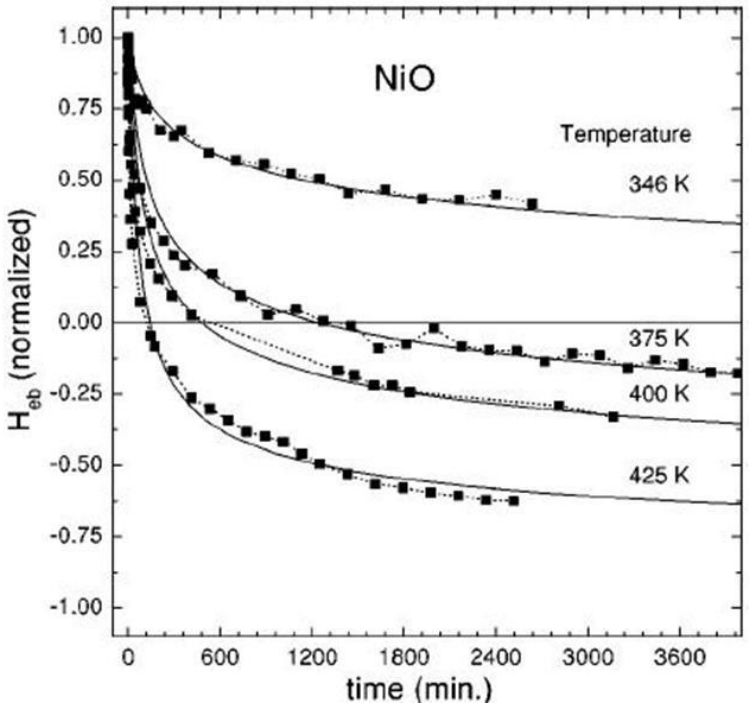


**Figure 36: Time dependence of exchange bias [*van der Heijden,1998*].**

Like Fulcomer and Charap, Van der Heijden modelled the system as non-interacting single domain antiferromagnetic particles and, like Fulcomer and Charap, there was agreement between theory and experiment.

# 4. The York Model

## 4.1 Theory

### 4.1.1 Introduction

As has already been said, the spin-valve had found great use in the industry of magnetic recording along with the exchange bias effect that occurred when an antiferromagnet is grown next to a ferromagnet. Given the usefulness of exchange bias it was only natural for the magnetic recording industry to fund research into how its effect could be optimised Thus, great numbers of research papers were produced investigating it [*Mauri,1987, Malozemoff,1987, Stiles and McMichael, 1999, Nowak,2002*]. Although the exchange bias effect itself was relatively easy to replicate, researching into exactly how it came about provided a number of challenges. The first one is the fact that it has no net moment so it cannot be examined by a conventional magnetometer. Only by examining its effect on a ferromagnet can anything be deduced about it. The second problem was that it was not easy to make reproducible measurements. Until this problem was solved, gaining a deeper understanding was always going to be a challenge.

### 4.1.2 Thermally stable temperature.

Generating reproducible results was the first challenge that *O'Grady et al.* tried to overcome [*O'Grady,2009*]. Given the fact that exchange bias reduces if the sample is heated up, thermal stability is clearly of importance so the first step is to insure that the bilayer is thermally stable throughout the measurement. To test this, the sample is first set in a field of 5000 Oe at $225^0$C for 90 minutes and then field cooled to the measurement temperature. The training effect is removed, a hysteresis loop is taken, and then the sample is held at the measurement

temperature for 30 minutes. A second loop is then taken and if there is a variation between the two, it can be assumed that the antiferromagnet is not thermally stable. The process is then repeated at decreasing temperatures until a thermally stable temperature is reached, and this is called the temperature of no thermal activation ($T_{NA}$). Once this has been established, all further measurements are then taken at this temperature.

### 4.1.3 Median Blocking Temperature.

As has been said, if the sample is heated up and then cooled back down to the measurement temperature, the exchange bias reduces. The concept of heating up the sample in a reverse field was then thought of and some interesting effects were then seen. It was found that it was actually possible to systematically vary the amount of exchange bias in controlled way. The temperature of no thermal activation is found and the sample is first set in the usual manner. Then, under a reverse field, it is heated up by $25^0$C, held there for 30 minutes, field cooled, and another measurement is taken. Once this done, it is found that the exchange bias has reduced.

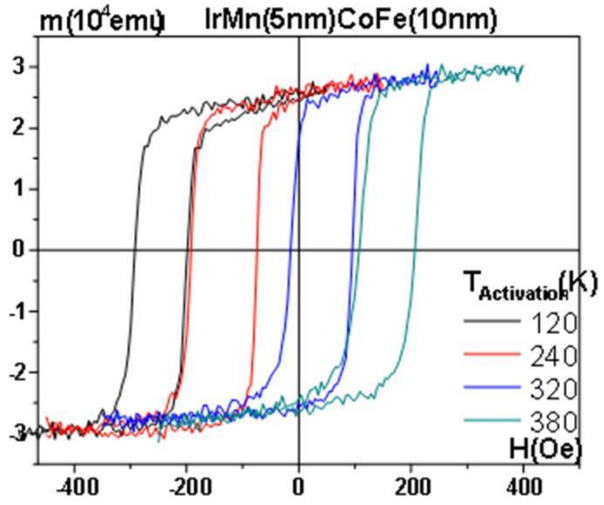


**Figure 37: Hysteresis loops showing varying exchange bias.**

Figure 37 shows what happens if this is then repeated for increasing temperatures. As can be seen, it is now possible to fully reverse the antiferromagnet. The temperature the sample is heated up to is called the activation temperature ($T_{ACT}$). This procedure was carefully documented and is shown in Figure 38 [*Vallejo-Fernandez,2010*].

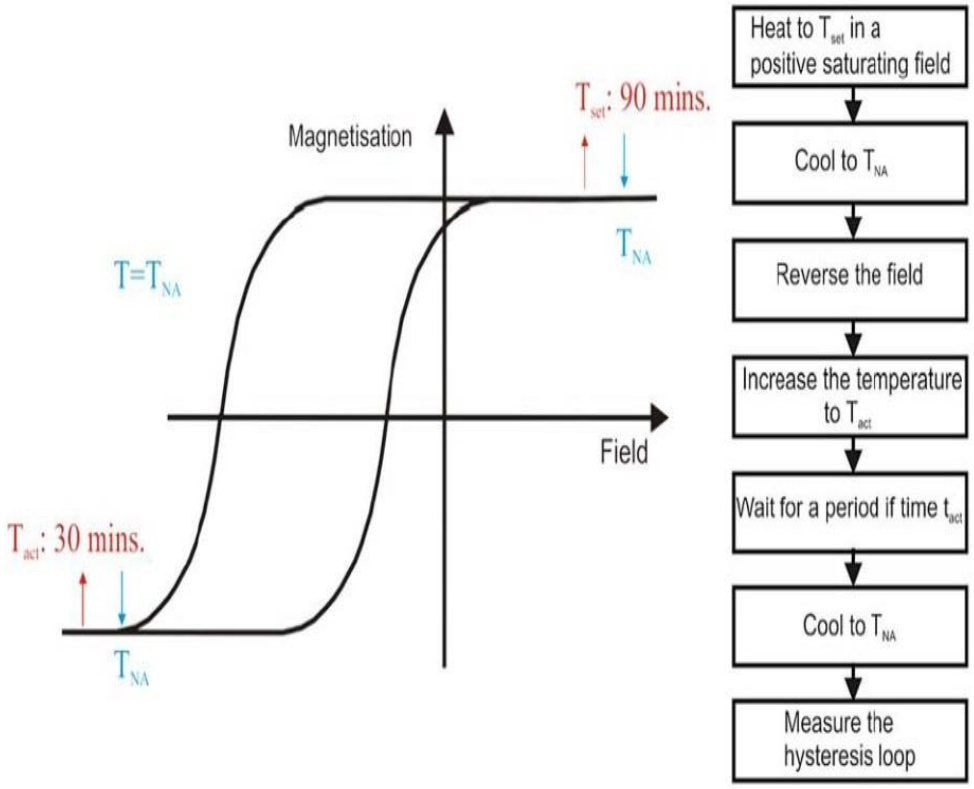


**Figure 38: Schematic of York protocol [*Vallejo-Fernandez,2010*].**

Having carried out this procedure, it is then possible to plot the exchange bias as a function of the activation temperature (Figure 39). With this graph, it is possible to make a number of assertions as to the character of the antiferromagnet which is producing the exchange bias effect.

One of the elements of this data, which is used shortly, is the activation temperature at which the exchange bias becomes zero, this is now called the median blocking temperature (<$T_B$>). This graph can be compared to the traditional blocking temperature measurement, where the sample is heated up and cooled down in the absence of a field (Figure 40) [*O'Grady,2009*].

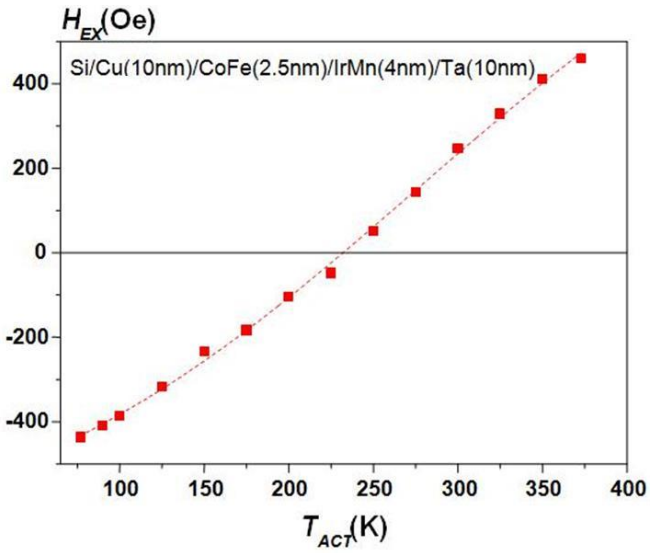


**Figure 39: Curve showing how <$T_B$> is experimentally derived.**

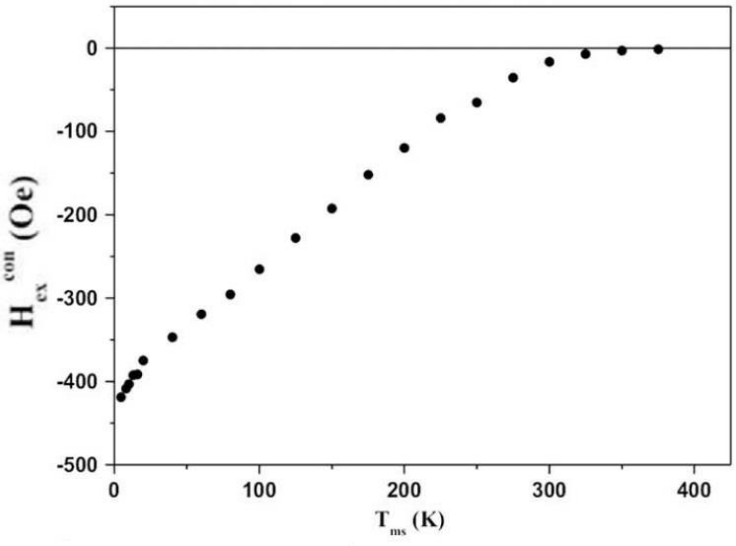


**Figure 40: Conventional Blocking Temperature Measurement [*O'Grady,2009*].**

### 4.1.4 Grain Volume Distribution

What has just been described is how characteristics of the antiferromagnet can be found out by the use of magnetometry. This section introduces the idea of imaging it by using a transmission electron microscope (see section 5.4 for more details). As has already been said, Fulcomer and Charap [*Fulcomer and Charap,1972*] assumed that the exchange bias was proportional to the fraction of antiferromagnetic grains that were orientated in a certain direction. In 1976, Granqvist [*Granqvist,1976*] conducted detailed grain size distributions on evaporated ultrafine metal particles and came to the following conclusion;

*'Size distributions have been investigated in detail, and consistently the logarithm of the particle diameter has a Gaussian distribution to a high precision for the smallest sizes.'*

(small sizes were defined as being below 20nm). Van der Heijden [*Van der Heijden,1998*] performed transmission electron microscopic analysis on the diameters of the grains of the antiferromagnet and also discovered that they followed a log normal distribution. Similar work was carried out by O'Grady *et al.* which agreed with this. A log normal distribution can be described by two parameters, its mean and its standard deviation. A variable is log normally distributed if its log follows a normal distribution

$$\boldsymbol{f(lnD)d(lnD)} = \frac{\mathbf{1}}{\sqrt{\mathbf{2}\pi}\boldsymbol{\sigma}}\boldsymbol{exp}\left[-\frac{\left(\boldsymbol{(lnD)}-\boldsymbol{\mu}\right)^{\mathbf{2}}}{\mathbf{2}\boldsymbol{\sigma}^{\mathbf{2}}}\right]\boldsymbol{d(lnD)} \qquad \text{Eqn. 4-1}$$

where D is the grain diameter, $\mu$ is the mean of *lnD* $\left(\overline{lnD}\right)$ and $\sigma$ is the standard deviation of *lnD* [*O'Grady,1983*].

The median grain volume, as shown in Figure 41, soon becomes significant. A grain is defined as an ordered region of antiferromagnet which shows up in a transmission electron microscope image as black, due to it obeying the Bragg condition of refraction (see section 5.4.3). When looking at the image in Figure 41, the grey areas are not considered to be grains.

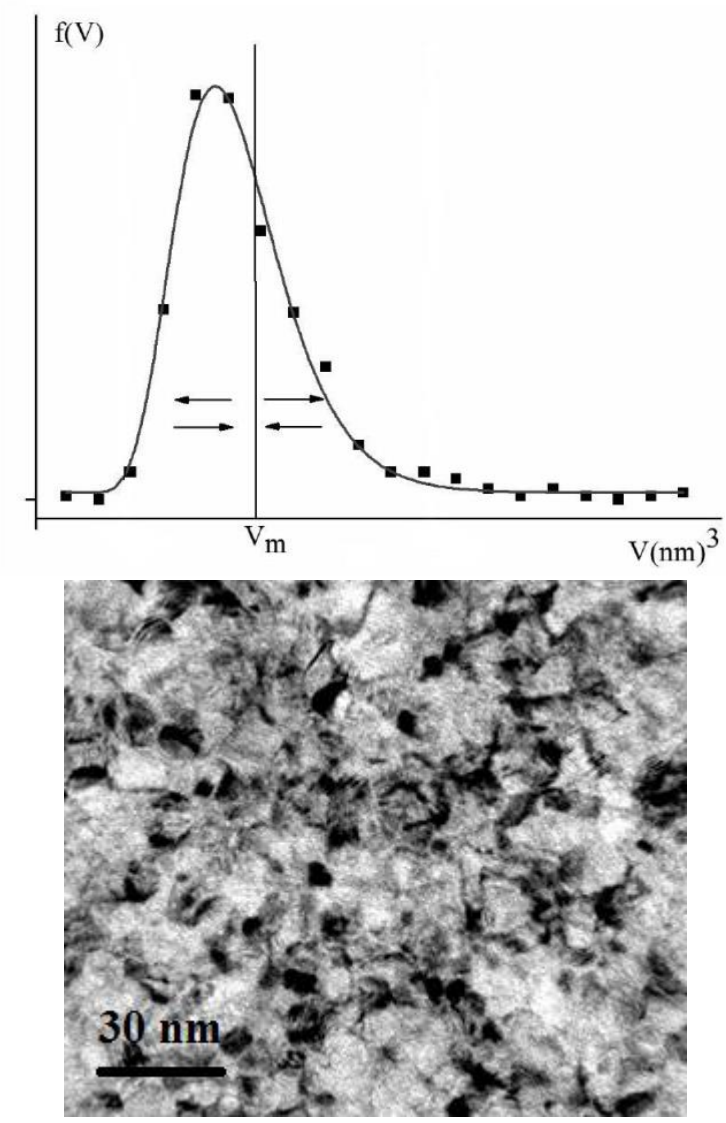


**Figure 41: Grain volume distribution showing $V_M$ and a TEM image.**

### 4.1.5 Mathematical Groundwork

In order to combine the grain size analysis with the magnetic measurements a number of assumptions are now made. The first is that the only region of the antiferromagnet that contributes to the exchange bias is that which is considered to be a grain. There is assumed to be no coupling between the grains (see section 2.1.6). The grains are assumed to be single domain, primarily due to their small size. The angular distribution of the grains both within the plane of the sample and out of the plane of the sample is not considered. There are no partial domain walls, or cyclic rotation of the magnetisation within the grain.

Once the grain has been defined in this way, based on the energy barrier equation from the Stoner-Wohlfarth theory, Equation 4-2 can be derived for a single domain particle.

$$\Delta E = K_{AF} V \left(1 - \frac{H^*}{H_K^*}\right)^2 \qquad \text{Eqn. 4-2}$$

where $\Delta E$ is the energy barrier of reversal for a grain, $K_{AF}$ is the anisotropy constant, $V$ is the grain volume, $H^*$ is the exchange field from the ferromagnetic layer and $H_K^*$ is the pseudo anisotropy field. $\frac{H^*}{H_K^*}$ is considered to be negligible for thin films [*Vallejo-Fernandez,2008*]. This means that Equation 4-2 reduces to Equation 4-3

$$\Delta E = K_{AF} V \qquad \text{Eqn. 4-3}$$

The reversal of the magnetic direction of the gain, when subject to heating, can now be evaluated with the application of the Néel-Arrhenius law

$$\tau^{-1} = f_O exp\left[\frac{\Delta E}{k_B T}\right] \qquad \text{Eqn. 4-4}$$

where $\tau$ is the relaxation time, $f_O$ is the attempt frequency, $k_B$ is Boltzmann's constant, and $T$ is the temperature.

Before all of these concepts so far described can be tied together, one more equation needs to be introduced. It is known that the anisotropy of a grain is temperature dependent and has been assumed to take the following form [*Stiles,1999*]

$$K_{AF}(< T_B >) = K_{AF}(0).\left[1 - \frac{< T_B >}{T_N}\right] \qquad \text{Eqn. 4-5}$$

where $T_N$ is the Néel Temperature.

### 4.1.6 Calculation of Anisotropy

Now the various aspects of the work can be brought together and what follows is the most important part. When the sample is heated up in a reverse field to a low activation temperature, the smaller grains are reversed. As the activation temperature is increased, larger and larger grains become reversed and the exchange bias shifts across the axis. When the exchange bias has shifted so that the hysteresis loop is now symmetrical, half of the antiferromagnetic is oriented in one direction and the other half in the opposing direction.

It is known what this activation temperature was and also how long the sample was held at this value. Therefore, by application of the Néel-Arrhenius law, the energy barrier to reversal for the grain which has reversed at this temperature can be calculated. What now ties both the magnetometry and the microscopy together is the assumption that the volume of this grain is the median grain calculated from the grain size distribution. Eliminating $\Delta E$ from Equations 4-3 and 4-4 yields an equation that calculates the value of the anisotropy of the antiferromagnet at the median blocking temperature

$$K_{AF}(< T_B >) = \frac{k_B < T_B > \ln(t_{ACT} f_o)}{V_M} \qquad \text{Eqn. 4-6}$$

where $t_{ACT}$ is the setting time. Once the anisotropy of the antiferromagnet is known at the median blocking temperature, it can now be calculated for the other two important temperatures in the measurement, the setting temperature and the measurement temperature by using Equation 4-5. An important term in this equation is $T_N$, in bulk materials it is quoted as 690K [*Nogues,1999*] however it is thought that this value could be lower in thin films.

### 4.1.7 Calculation of Largest Settable Grain and Smallest Stable Grain.

Once the anisotropy of the antiferromagnet is known, more detail can be added to Figure 41 in order to generate Figure 42. Equations 4-7 and 4-8 are used to calculate the volume of the largest grain that can be set during the setting process and the smallest stable grain during the measurement;

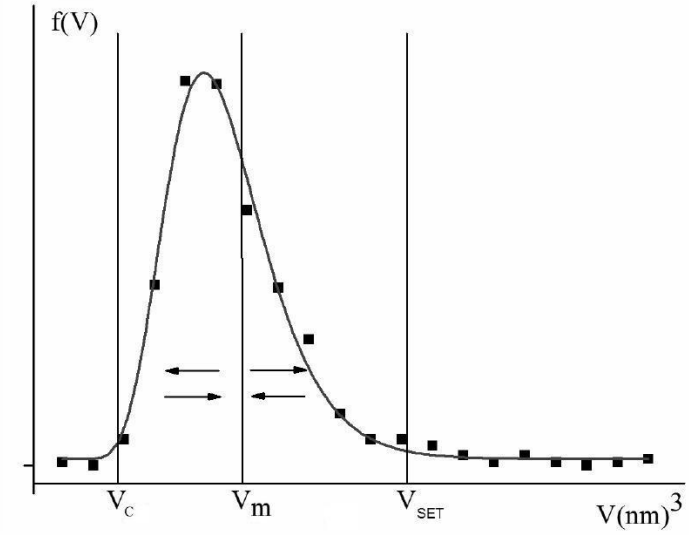


**Figure 42: Equal volumes of the AF set in opposite directions.**

$$V_{SET} = \frac{k_B T_{SET} \ln(f_O . t_{SET})}{K_{AF}(T_{SET})} \qquad \text{Eqn. 4-7}$$

$$V_C = \frac{k_B T_{MS} \ln(f_O . t_{MS})}{K_{AF}(T_{MS})} \qquad \text{Eqn. 4-8}$$

where $V_{SET}$ is the largest settable grain, $T_{SET}$ is the setting temperature, $t_{SET}$ is the setting time and $V_C$ is the smallest stable grain during measurement, $T_{MS}$ is the measurement temperature and $t_{MS}$ is the measurement time. The grains that are larger than $V_{SET}$ are thought to be randomly oriented, and so can be ignored in their contribution to the exchange bias. The grains that are smaller than $V_C$ are thought to be unstable during the measurement so, again, their contribution to the exchange bias is also deemed to be zero (see Figure 43).

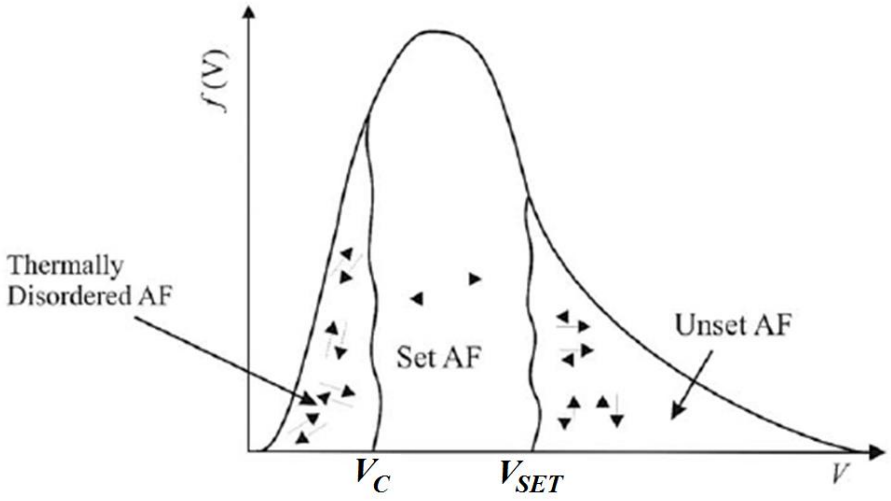


**Figure 43: Grain Size Distribution [*O'Grady,2009*].**

### 4.1.8 Calculation of Maximum Exchange Bias.

The two limits seen in Figure 43 define the settable fraction of the antiferromagnet that contributes to the exchange bias and the following equation can be written.

$$H_{EX}(T_{MS}) \propto \int_{V_c}^{V_{SET}} f(V)dV \qquad \text{Eqn. 4-9}$$

For a given anisotropy, the upper and lower limits are constant. However, the amount of antiferromagnet that falls within these limits can be changed by either varying the thickness of the layer in the sample, or by varying the grain size distribution (Figure 44).

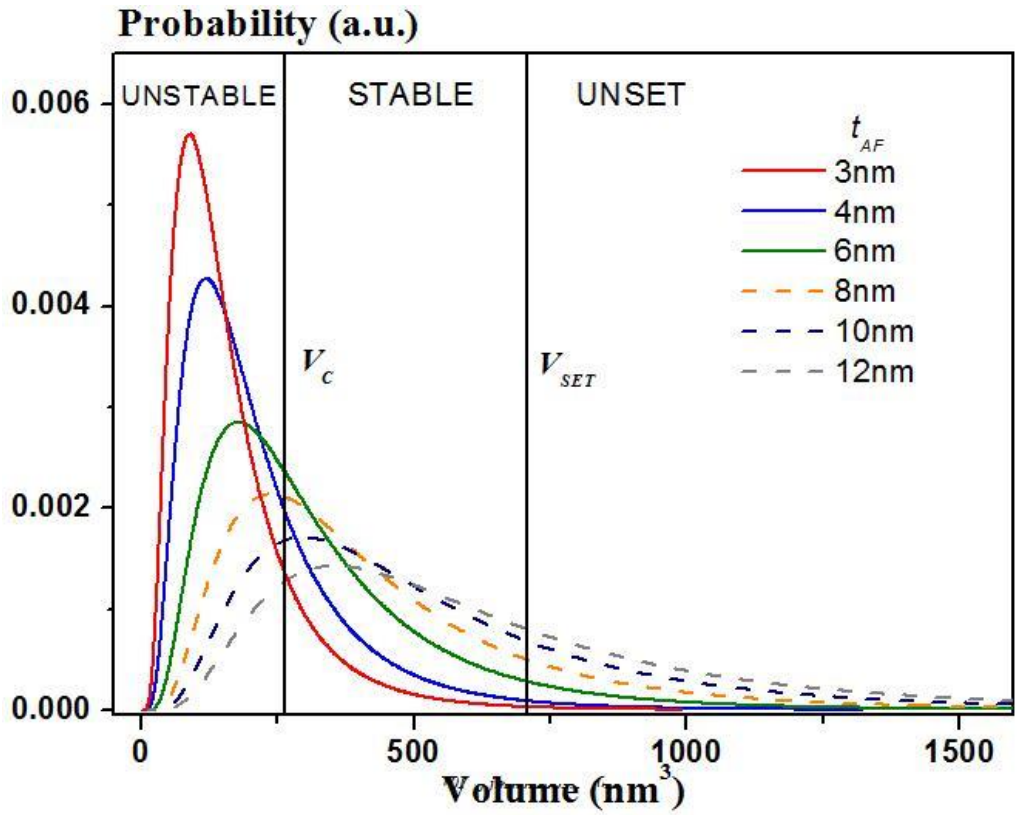


**Figure 44: Variation of grain size distributions [*Vallejo-Fernandez,2008(b)*].**

Therefore, Equation 4-9 is able to predict the variation of exchange bias for both varying the thickness of the antiferromagnet and varying grain size, as seen in Figure 45 and 46. Figure 45 can actually be compared to Figure 32 from earlier. The differences though are that the experimental data produced by Ali [*Ali,2000*] only showed a peak when the temperature was reduce to below 200K and it was at a much higher antiferromagnetic thickness of 25nm. The variations of exchange bias as a function of either antiferromagnetic thickness or grain size diameter have all been calculated by evaluating the volume of the antiferromagnet that falls within the settable limits.

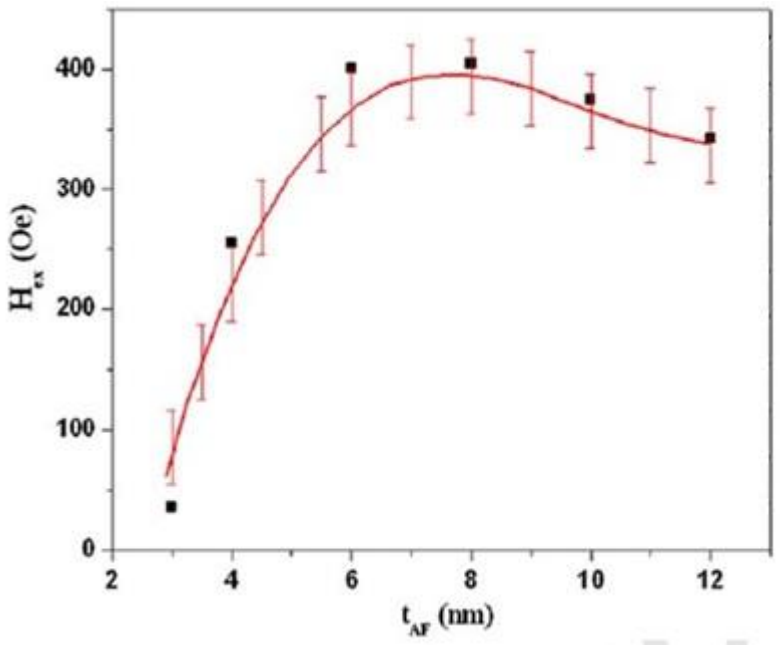


**Figure 45: Exchange bias verses antiferromagnet layer thickness [*Vallejo-Fernandez,2008(b)*].**

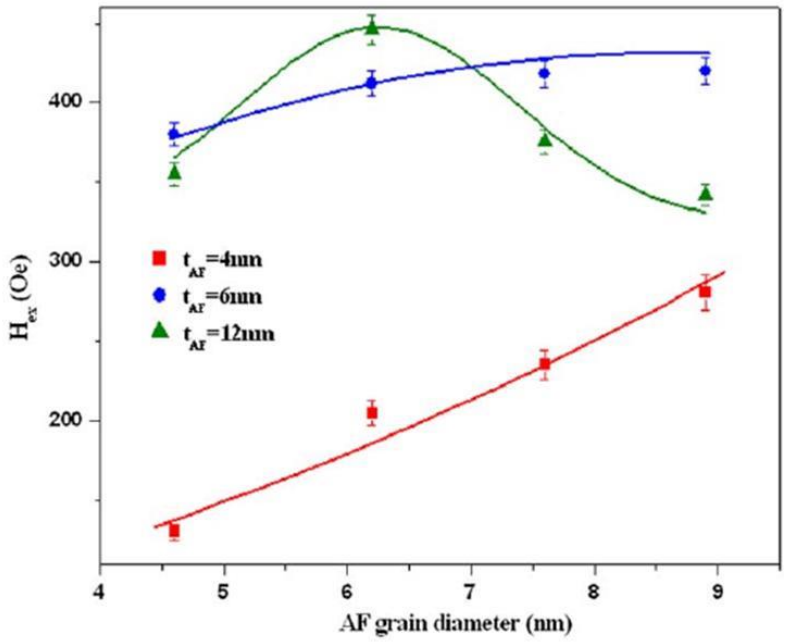


**Figure 46: Exchange bias as a function of grain diameter for various antiferromagnetic thicknesses [*Vallejo-Fernandez,2008(b)*].**

### 4.1.9 Interface effects

After having come up with a model of the bulk of the antiferromagnet the nature of the interface in between the Iridium Manganese and the Cobalt Iron was postulated. In order to continue with the uncoupled, independent granular concept of the bulk of the antiferromagnet, the idea of interfacial spin clusters was conceived. Essentially, the interfacial spin clusters are thought to sit on top of the grains (Figure 47). They behave semi-independently, take the same diameter as the grain on which they sit and consist of N spins, where N ranges from 10 to 50 [*O'Grady,2009*].

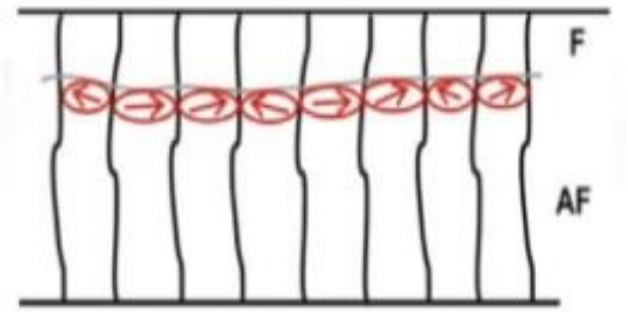


**Figure 47: Interfacial Spin Clusters.**

The effect of the interfacial spin clusters are described in a modified version of Equation 4-9 whereby they are represented by a $C^*$

$$H_{EX}(T_{MS}) = C^* \int_{V_c}^{V_{SET}} f(V)dV \qquad \text{Eqn. 4-10}$$

Their effects on the value of the exchange bias and coercivity are subject to a detailed investigation in section 6.

### 4.1.10 York Model Evaluation

There are some simplifications made in the model in order to help it work. As has already been said, the angular distribution of grains within the plane is not considered. Maybe the assumption could be made that there is an equal distribution at all angles. However, there is a magnet suspended above the sample during deposition in order to induce an easy axis. The easy axis and hard axes can be seen if the sample is placed, by mistake, in the wrong direction in a magnetometer. But whether this means all grains are now aligned in the direction of the easy axis is not known.

If one was to perform a grain size analysis on the image in Figure 42, there are actually not that many grains that would be counted as there are only a few clearly distinct grains. This means that the large grey and white areas are disregarded in the model. The distance between the grains does mean there is little chance of there being any interaction between them, so they can be considered as discrete. However, it still remains that a majority of the sample is assumed to have no contribution in the calculated exchange bias.

There is also an interdependence introduced when the values of $V_C$ and $V_{SET}$ are then derived by the value of $V_M$. If the assumption that the exchange bias during the median blocking temperature measurement is equal to zero when the median grain reverses was inaccurate, then $V_C$ and $V_{SET}$ could still be calculated and theoretical data obtained, despite being the wrong values.

There are further issues with the limits of $V_C$ and $V_{SET}$ as well. In order to create a theoretical line that fits the data, the measurement time is reported as being 100 seconds [*O'Grady,2009*]. This is not the case, as the measurement time is at least 1200 seconds and sometimes up to 3600. Also, if the model is disregarding a large portion of the sample's contribution to the exchange bias, this would lead to an increase in the calculated value of the anisotropy. This is seen when comparing the anisotropy value to other work [*Carey,2001*]. Such a high value is also somewhat in conflict with the polycrystalline nature of the samples.

## 4.2 Experimental Aspects

This section is an overview of the work that has been carried out based on the model explained in section 4.1 and there are three main topics. The first describes what happens by varying the seed layer of the antiferromagnet. The second describes what happens if impurities are introduced to the antiferromagnet. The third investigates the training effect.

### 4.2.1 Texture

The samples used for this research were Si (100) / seed (5nm) / IrMn (10nm) / CoFe (3nm) / Ta (10nm). The different seed layers used were Ruthenium, Copper and Nickel Chromium. Ruthenium and Copper were used as they are known to have a close lattice match to Iridium Manganese (Table 1), and Nickel Chromium was used as it was recommended by Seagate.

The composition of the Nickel Chromium used was $Ni_{60}Cr_{40}$ and is known to be non-magnetic [*Jette,1934*]. 5nm of seed layer was chosen because work carried out by Tsunoda [*Tsunoda,2006*] showed that the effect of the seed layer thickness on the antiferromagnetic texture increased up to that value but there was little variation above it. 10nm of Iridium Manganese was chosen as it has been found by O'Grady *et al* that this thickness of Iridium Manganese is stable at room temperature, which means measurements can be taken without the need for liquid Nitrogen cooling. 3nm of Cobalt Iron was chosen as this gives the magnetometers a large enough signal to be measured without compromising the values of exchange bias. Tantalum was the last layer to be deposited because although it does oxidise, once it has it acts as a good capping layer.

| *Material* | *Structure* | *Lattice Constant* | | *d(111)/d(0001)* | *Lattice Mismatch to IrMn* |
|---|---|---|---|---|---|
| | | a(Å) | c(Å) | | (%) |
| IrMn | FCC | 3.78 | - | 2.67 | 0 |
| Ru | HCP | 2.70 | 4.67 | 2.70 | 1.2 |
| NiCr | FCC | 3.56 | - | 2.52 | -5.8 |
| Cu | FCC | 3.61 | - | 2.56 | -4.4 |

**Table 1: Lattice constants of IrMn and seed layer materials [*Peng,2009*].**

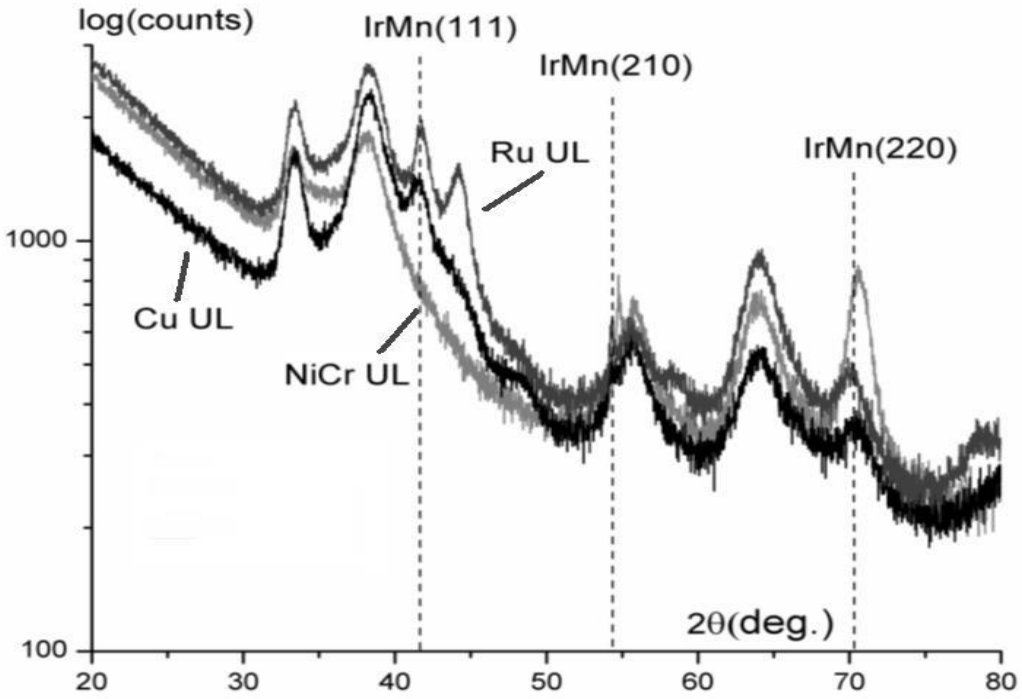


**Figure 48: Grazing angle scans for samples with NiCr, Ru and Copper [*Aley,2008(a)]*.**

The samples were characterised using X-rays diffractometry and magnetometers. Figure 48 shows the results of a grazing angle scan. The primary section of interest is the Iridium Manganese (111) region where 2θ is around 40 degrees. The interesting result is that Nickel Chromium does not show a peak whereas Ruthenium and Chromium do. The geometry of the grazing angle is such that

crystal planes parallel to the substrate do not diffract, this means that the (111) diffraction of Ruthenium and Chromium are actually from crystals out of plane. This result therefore implies that the Nickel Chromium seed layer significantly increases the number of crystals whose (111) plane is parallel to the substrate.

Previous to this work, Fecioru-Moraiu [*Fecioru-Moraiu,2007(a)*] had also carried out investigations into the effects of seed layers. Initially they deposited Iridium Manganese on amorphous Cobalt Iron Boron and found there to be no exchange bias. They then inserted increasingly thick layers of Nickel Iron in between the Cobalt Iron Boron and Iridium Manganese and found that the exchange bias correspondingly increased. They also performed X-ray diffraction which confirmed increased crystallinity.

A full set of magnetic measurements were taken of the samples which followed the procedure described in section 4.1 (Figure 49). As can be seen from the results, the Ruthenium and Copper seeds layers show a greater degree of symmetry than the Nickel Chromium. This implies that they undergo a full reversal of the antiferromagnet, whereas the Nickel Chromium is not fully reversed by 500K. The two other aspects of the results is that after initial setting, the Ruthenium sample has a noticeably lower exchange bias than the other two samples and that the sample grown on Nickel Chromium has a significantly higher median blocking temperature.

A further measurement of the Nickel Chromium sample was carried out using a higher setting temperature (Figure 50). As can be seen on this occasion the antiferromagnet is successfully reversed and aligned, also the measurements almost precisely overlap. It can be seen that the increase in the initial setting temperature does not increase the initial exchange bias. The most probable reason for this is that there is a 500 Oe magnet suspended one cm above the substrate during deposition. The purpose of this is to induce an easy axis during the growth of the sample. What may also happen is that, despite Iridium Manganese being an

antiferromagnet, during its growth the newly arriving atoms are subject to the magnetic field. The result is that Iridium Manganese is effectively fully set during deposition.

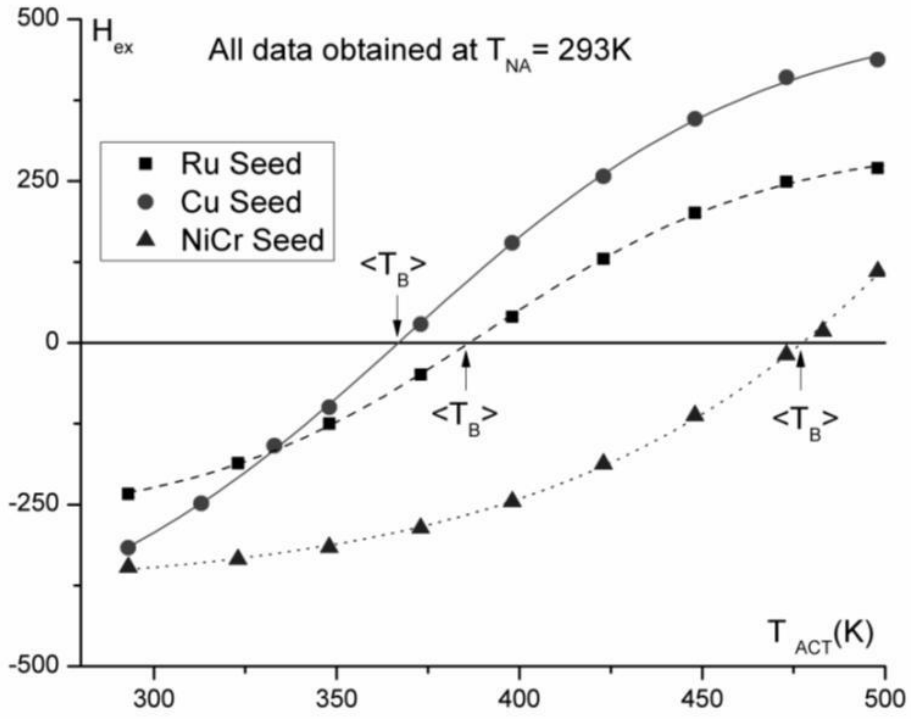


**Figure 49: Thermal activation measurements to determine $<T_B>$ for samples with Ru, Copper and NiCr seed layers [*Aley,2008(a)]*.**

There is also a second important conclusion to draw from the fact that the points overlap. When looking at the blocking curves in Figure 49, the fact that the Iridium Manganese is not fully reversed by the end of the experiment might make one mistrust the value of the median blocking temperature. Given that this remains constant confirms its value.

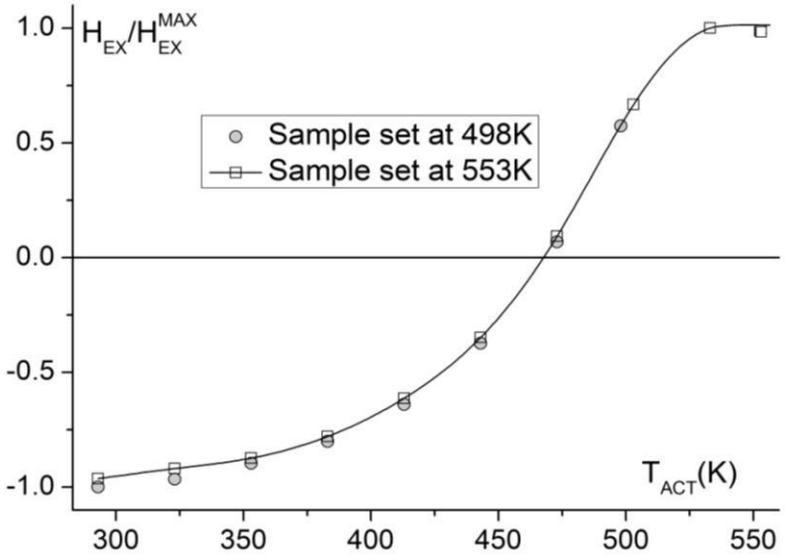


**Figure 50: Blocking Curve where sample was set at 498K and then at 553K.**

| Seed Layer | $D_{vm}$ (nm) ±0.5nm | $V_{vm}$ *(nm3)* | *σ (lnD)* | $<T_B>$ (K) ±2K | $H_{EX}$ (Oe) ±5Oe | $K_{AF}$ (erg·cm-3)×$10^7$ |
|---|---|---|---|---|---|---|
| NiCr | 3.9 | 119±25 | 0.42 | 477 | 350 | 2.9±0.6 |
| Ru | 6.0 | 283±40 | 0.38 | 386 | 233 | 0.69±0.1 |
| Cu | 10.7 | 899±100 | 0.37 | 367 | 315 | 0.20±0.02 |

**Table 2: Summary of results for seed layer experiment.**

The X-ray diffractometry results suggest that that Nickel Chromium seed layer promotes (111) in-plane orientation. Table 2 combines the blocking temperature measurements along with grain size analysis and anisotropy calculations and gives some more insight into the three samples. The most surprising value in the table is the median grain size of Nickel Chromium. If the grain size distribution of all three samples were the same, then the improved (111) orientation in the Nickel

Chromium would result in an increased anisotropy and, in turn, would result in a corresponding increase the value of median blocking temperature.

However, the median grain diameter, and therefore the median grain volume of the Nickel Chromium sample is significantly smaller than the other samples, especially the Copper. So, although the median blocking temperature of Nickel Chromium is only 10% higher than the other samples, the anisotropy is much greater.

There have been other methods used to measure the anisotropy of the antiferromagnet in thin films. In 1987 Mauri [*Mauri,1987*] used an in situ Kerr rotational measurement to study the coupling between the antiferromagnetic and ferromagnetic layers. He derived a relationship from the equations that describe the energy per unit surface of the interface as an exchange bias system

$$H_{EX} = \frac{t_{CR} K_{AF}}{t_F M} \qquad \text{Eqn. 4-22}$$

where $t_{CR}$ is the thickness of the antiferromagnetic layer above which there is a sharp onset of exchange bias, $t_F$ is the thickness of the ferromagnetic layer and $M$ is the saturation magnetisation. The value obtained from this for the anisotropy of Iron Manganese was given as 1.35 x $10^5$ ergs / $cm^3$. Carey performed anisotropy calculations on Nickel Chromium and Iridium Manganese based on an Arrhenius-type model where the grains were assumed to be able to reverse independently. The values were found to be 5x$10^5$ and 2x$10^6$ ergs / $cm^3$[*Carey,2001*]

### 4.2.2 Composition

The samples used for this research were Si (100) / NiCr (5nm) / Ru (5nm) / [IrMn] (1-x  Copper x (10nm) / CoFe (2nm) / Ta (3nm). There is a variation in the seed layer from the previous set of samples because now two different seeds layers are used. This was done in order to take advantage of characteristics from both.

The Nickel Chromium was used to induce a high level of (111) in-plane crystallinity as shown in the previous section. However, using only Nickel Chromium as a seed layer meant that the median grain size was very small, which resulted in it being more difficult to perform a measurement of the grain size distribution.

The consequence of adding the Ruthenium on top of the Nickel Chromium was to increase the median grain size from around 3nm to about 6nm. Again, 10nm of Iridium Manganese was chosen so that the antiferromagnet was stable at room temperature.

The Iridium Manganese was then doped with Copper. This was because Copper (a = 3.61Å) and Iridium Manganese (a = 3.78Å) have similar lattice constants, this means that the Iridium Manganese can be diluted without introducing significant lattice strain. The impurities were introduced to the sample by modifying an Iridium Manganese target (Figure 51).

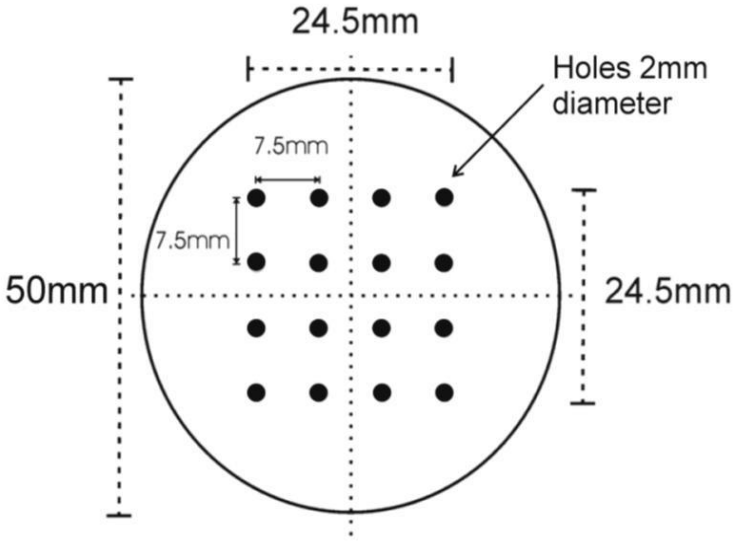


**Figure 51: Schematic of the target designed for sputtering IrMn with varying Copper impurity level.**

Holes were drilled into the target so that small pieces of Copper could be inserted which would introduce an unknown quantity of Copper. To determine this, a separate sample was grown which stopped after the Iridium Manganese layer and a scanning electron microscope with an energy dispersive X-ray spectroscopy system was used.

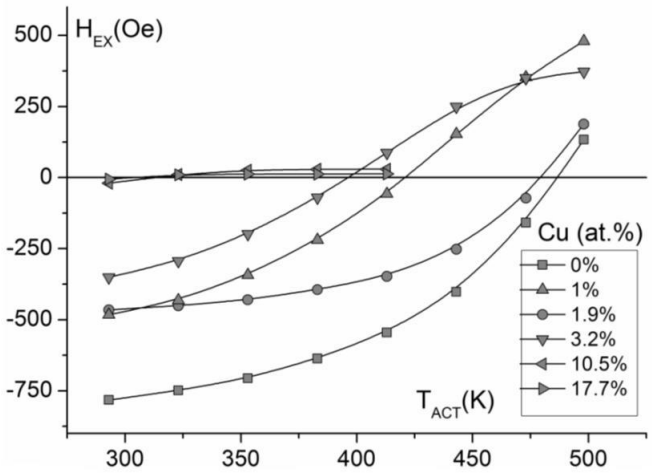


**Figure 52: Results of thermal activation measurements for varying Copper impurity levels *[Aley,2008(b)]*.**

Figure 52 shows the blocking temperature measurements taken of the 6 different samples with varying levels of doping. Clearly, the exchange bias is severely reduced for the samples with 10.5 at.% and 17.7 at.% which suggests that the level of impurity is so high that the antiferromagnetic nature of the Iridium Manganese broke down. However, the other four samples show an unusual behaviour where the 1.9 at.% has a very similar form to the 0 at.% and the 3.2 at.% has a very similar form to the 1 at.%. If it is assumed that the doping of each of the samples has resulted in a relatively uniform distribution of the dopant, then a possible explanation is that the antiferromagnet is going through various different phases as it increases. This is possible as pure Iridium Manganese can take up a number of different phases as described in section 4.2.3.

| Copper Impurity (at.%) | $D_{vm}$ (nm) ±0.5nm | ln(D) | $\langle T_B \rangle$ (K) ±2K | $K_{AF} \times 10^6$ (ergs/cc) | $H_{EX}MAX$ (Oe) ±5Oe |
|---|---|---|---|---|---|
| 0 | 6.4 | 0.40 | 486 | 12±2 | 782 |
| 1.0 | 5.4 | 0.37 | 421 | 11±2 | 483 |
| 1.9 | 6.0 | 0.48 | 479 | 12±2 | 465 |
| 3.2 | 5.16 | 0.49 | 396 | 10±2 | 351 |
| 10.5 | 5.58 | 0.44 | 314 | 5.3±1 | 20 |
| 17.7 | 5.70 | 0.39 | 304 | 4.8±1 | 5 |

**Table 3: Summary of compositional analysis, grain size analysis and thermal activation measurements.**

Table 3 shows the median diameters along with the blocking temperatures. This shows that the grain diameters are relatively constant, which is good as it means that the samples are more comparable. There is also a clear decrease in the exchange bias as the doping level is increased. This indicates that the Copper doping is disrupting the exchange bias effect of the antiferromagnetic grains. The

decrease in anisotropy also suggests that the antiferromagnetic nature is also being reduced.

Previous to this work, Fecioru-Moraiu [*Fecioru-Moraiu,2007(b)*] had also carried out investigations into the nonmagnetic dilutions in the antiferromagnet. On this occasion, their results were completely different. Upon dilution, they initially witnessed an increase in the exchange bias, as opposed to only a decrease in the work of Aley. However, there is an explanation for the difference,. The samples used in the work of Fecioru-Moraiu were grown by molecular beam epitaxy, and the average grain size was around 65nm. In the work carried out by Aley, the samples were grown by deposition and the average grain size was 6nm. In epitaxially grown materials, domain wall in the antiferromagnet can easily form and, thus, their behaviour varies significantly.

### 4.2.3 The Training Effect

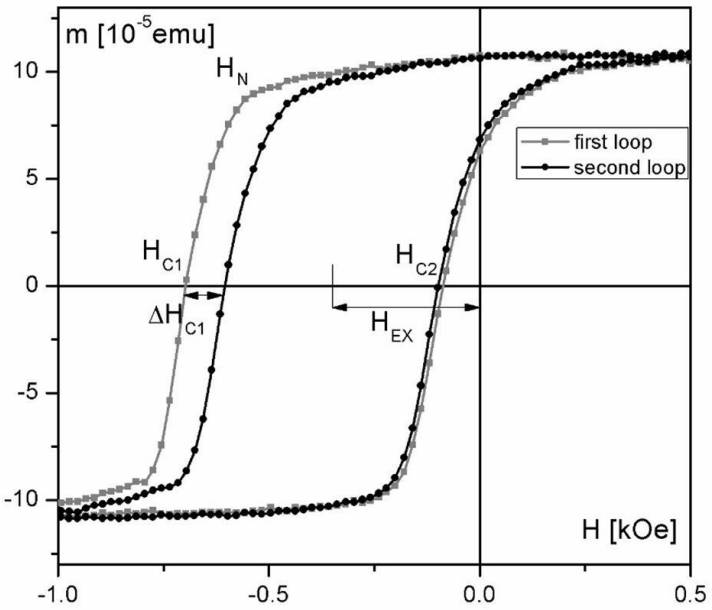


**Figure 53: Hysteresis loops showing the training effect [*Kaeswurm,2010*].**

This section describes the experimental aspects of the training effect in exchange bias systems. Figure 53 shows two hysteresis loops that show the training effect which is where the left hand side of the loop varies with subsequent cycling.

The sample was a standard Cu (5nm) / IrMn (10nm) / CoFe (3nm) / Ta (5nm) exchange bias bilayer with the measurement taken at room temperature. The figure shows how $H_{EX}$, $H_N$, $H_{C1}$, $H_{C2}$ and $\Delta H_{C1}$ are defined, where $H_{EX}$ is the exchange bias, $H_N$ is the nucleation field which is the field required to nucleate the first reversed domain, $H_{C1}$, is the left hand coercivity, $H_{C2}$ is the right hand coercivity and $\Delta H_{C1}$ is the training effect.

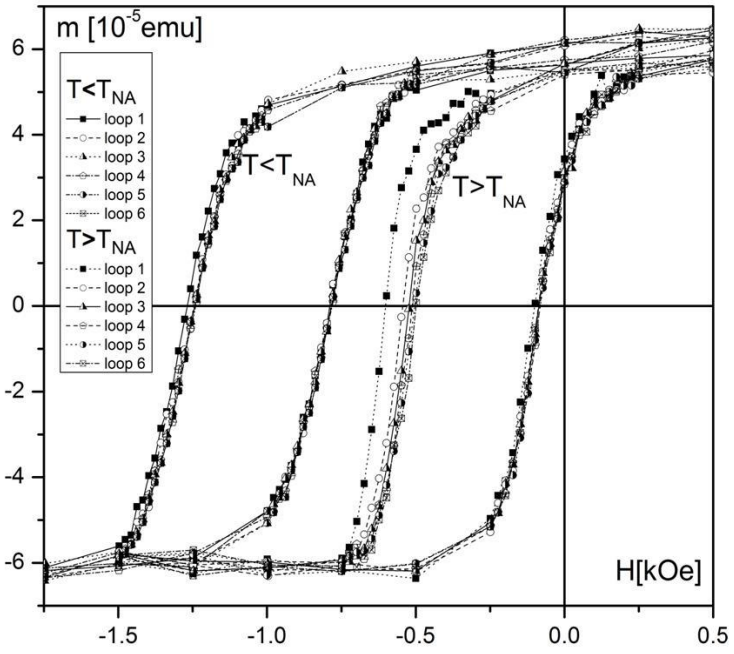


**Figure 54: Training effects measured above $T_{NA}$ and below $T_{NA}$.**

Figure 54 shows hysteresis measurements taken with the same sample as in Figure 53. However, where Figure 53 was merely demonstrating what the training effect is, this investigates it more thoroughly and it does so in two ways. Firstly, the training effect is investigated for a number of loops. Secondly, one set of

measurements is taken below $T_{NA}$ and another set is taken above $T_{NA}$. $T_{NA}$ is defined as the temperature of no thermal activation, which is the temperature where the antiferromagnetic layer of the sample remains stable throughout the course of the measurement.

This implies that by taking subsequent hysteresis loops below this temperature, any variation in the loop is not due to the antiferromagnetic grains thermally relaxing. When the loops are taken above this temperature then the sample is not thermally stable and, as can be seen from the results, there is a noticeable change in $\Delta H_{C1}$. This is due to changes in the bulk as some of the grains thermally relax.

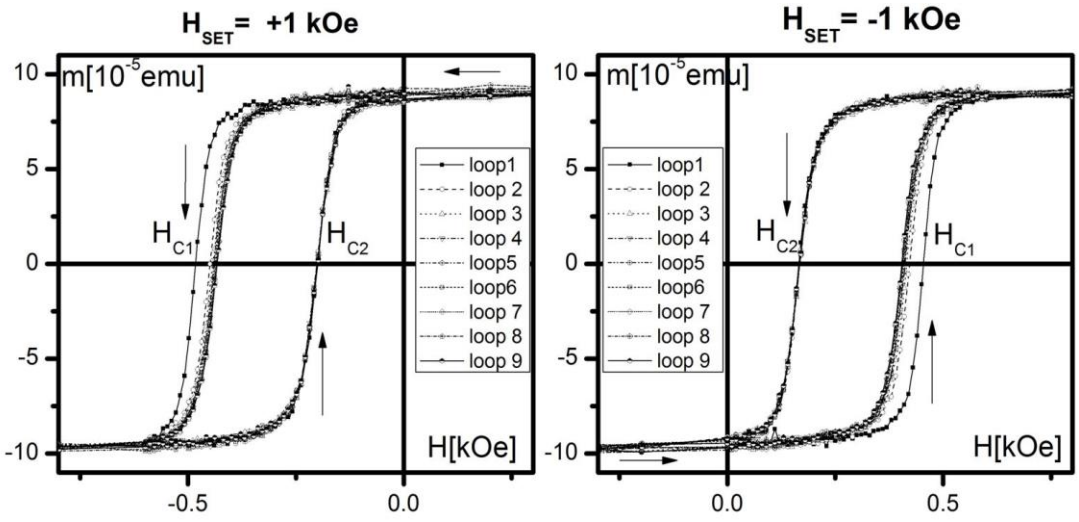


**Figure 55: Experimental results showing the effect of reversing the setting field.**

Figure 55 again shows hysteresis loops taken of the previous sample, except on this occasion the setting field had its direction reversed. Although simple, this demonstrates the axial symmetry of the training effect. The actual value of $\Delta H_{C1}$ in the positive field was 73 Oe, and in the negative field was 64 Oe. This slight difference could just be down to an error in the measurement due to the non-central location of the sample in the magnetometer, or it might suggest a slight asymmetry is the coercivity along this axis due to the sample being polycrystalline.

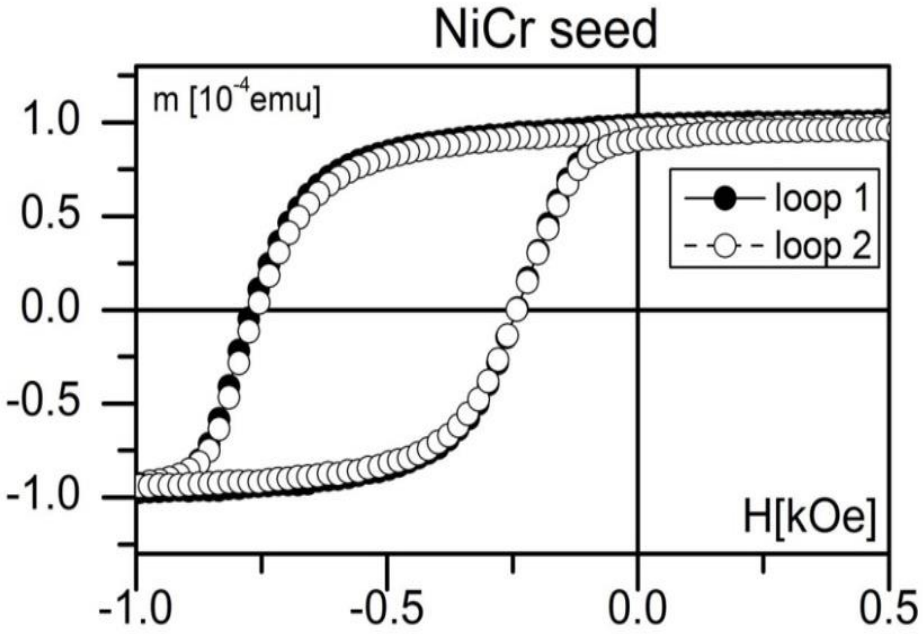


**Figure 56: Training effect from using a NiCr seed layer.**

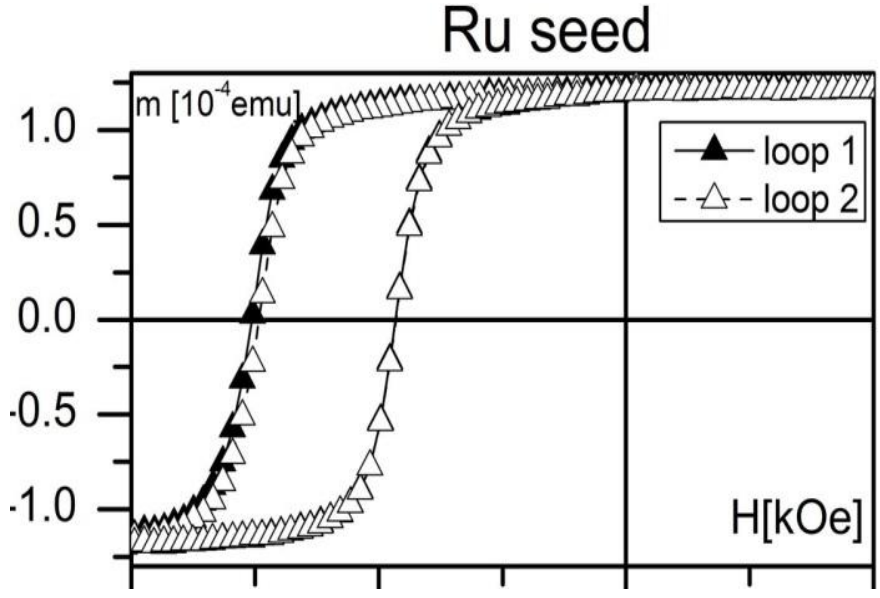


**Figure 57: Training effect from using a Ru seed layer.**

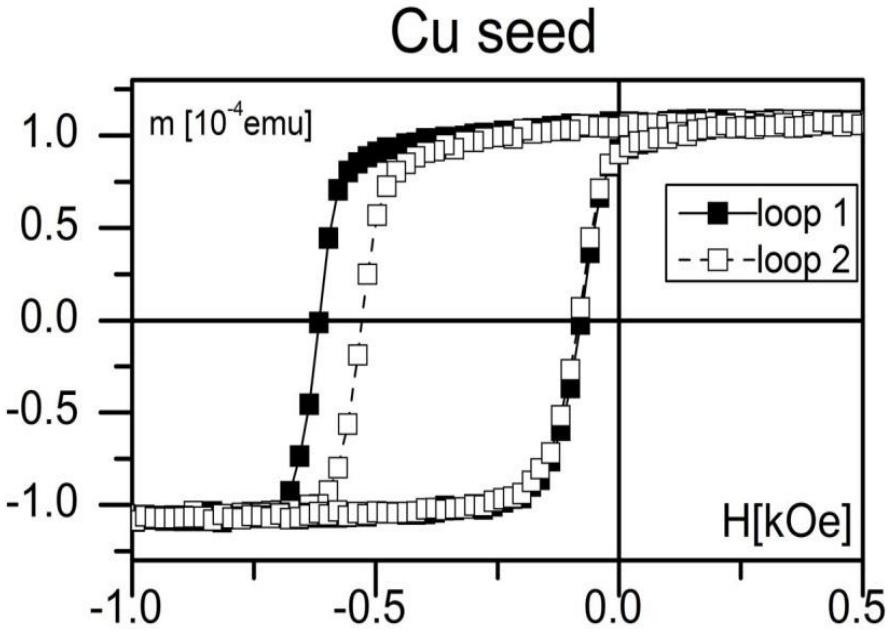


**Figure 58: Training effect from using a Cu seed layer.**

Figure 56, Figure 57 and Figure 58 show the variation in training when the seed layer in changed from Copper to Ruthenium and Nickel Chromium. As explained in Section 4.2.1, these different seed layers significantly change the crystallography of the Iridium Manganese and this clearly has a major impact on the training effect. These results are also shown in Table 4. The training effect is usually a relatively small one so the consequence of varying the seed layer has a very significant effect.

| Seed | $D_m$(nm) | $<T_B>$ [K] | $K_{AF}(293)[x10^7$ ergs/cc] | $\Delta H_{C1}(293)$ [Oe] |
|---|---|---|---|---|
| NiCr | 3.9±0.5 | 477±5 | 2.9±0.2 | 6±2 |
| Ru | 6.0±0.5 | 386±5 | 0.7±0.1 | 38±2 |
| Copper | 10.7±0.5 | 367±5 | 0.2±0.1 | 100±2 |

**Table 4: Median grain size, blocking temperature, anisotropy and training effect of three different seed layers.**

The value of exchange bias is known to vary as the inverse of the thickness of the ferromagnetic layer. As far as the training effects goes, there is a clear decrease as the thickness increases, however, if this is taken as a percentage of the exchange bias then the opposite trend is seen (Table 5).

| $t_F$ [nm] | $<T_B>$ [K] | $K_{AF}$ (293) [x$10^6$ergs/cc] ±0.05 | Loop 1 | | Loop 2 | | $\Delta H_{C1}$ | $\Delta H_{C2}$ | $\Delta H_{C1}/H_{C1}$ (n=2) |
|---|---|---|---|---|---|---|---|---|---|
| | | | $H_{C1}$ [Oe] | $H_{C2}$ [Oe] | $H_{C1}$ [Oe] | $H_{C2}$ [Oe] | | | |
| 3 | 315 ±5 | 4.59 | -915 ±20 | -300 ±20 | -795 ±20 | -320 ±20 | -120 ±25 | 20 ±28 | 0.15 ±0.04 |
| 4 | 312 ±5 | 4.54 | -555 ±20 | -221 ±20 | -490 ±20 | -233 ±20 | -65 ±25 | 12 ±21 | 0.13 ±0.04 |
| 8 | 290 ±5 | 3.94 | -242 ±5 | -95 ±5 | -220 ±5 | -95 ±5 | -22 ±7 | 0 ±7 | 0.10 ±0.03 |
| 12 | 220 ±5 | 2.61 | -160 ±2 | -45 ±2 | -145 ±2 | -45 ±5 | -15 ±3 | 0 ±3 | 0.10 ±0.02 |

**Table 5: Variation of training effect as a function of ferromagnetic thickness.**

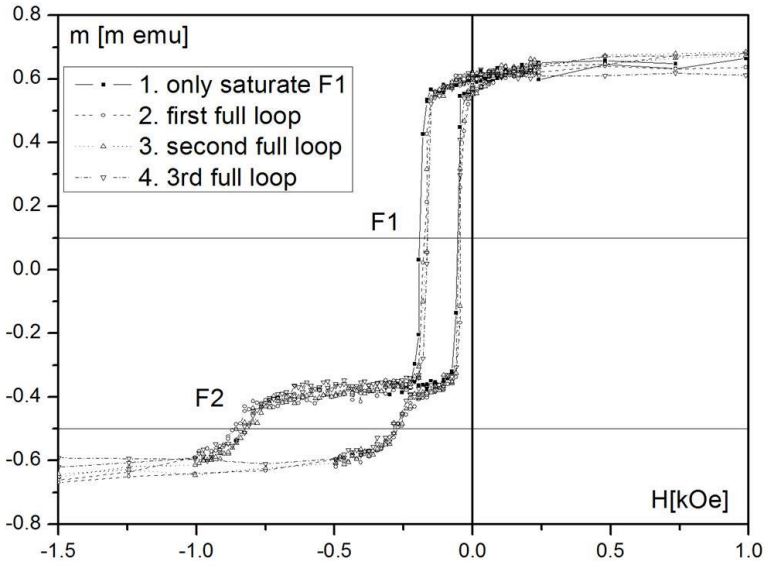


**Figure 59: Trilayer measurements showing training [*Kaeswurm,2011*].**

Hoffman [*Hoffmann,2004*] came up with an explanation of the training effect. He suggested that before the first loop was taken, the magnetisation of the antiferromagnetic sublattices lay perpendicular to each other, but after the first loop, they aligned antiparallel. This would require a change in the state of the bulk of the antiferromagnet. Figure 59 shows the results of measuring a tri layer [*Kaeswurm,2011*]. Due to the split nature of the loop, it is possible to reverse only one of the ferromagnetic layers. If this is done, the training effect can be removed for that layer. However, this does not remove the training effect of the opposite layer. Therefore, the conclusion to be drawn from this experiment is that there is not in fact a change in the properties of the bulk of the antiferromagnet but rather the interface.

# 5. Experimental Techniques

## 5.1 Sample Growth

### 5.1.1 Thin Film Growth

Sputtering was first observed in 1853 by R.R. Grove [*Grove,1852*] while he was investigating the electrical conductivity of gases and has advantages over other deposition methods, such as molecular beam epitaxial (MBE) growth because of its high growth rate. The vast majority of sputtering machines are magnetron sputterers. An Argon plasma is generated above a target which is at a negative potential of several hundred volts. A magnetic field is also applied which confines the plasma and results in an enhanced collision probability with more efficient sputtering. However, the field has strong flux lines which results in the plasma being highly concentrated on certain parts of the target. This means there is an area of the target which is eroded at a much high rate and leads to the characteristic race track erosion profile. The substrate is held at around 4cm above the target, although this can be varied (Figure 60).

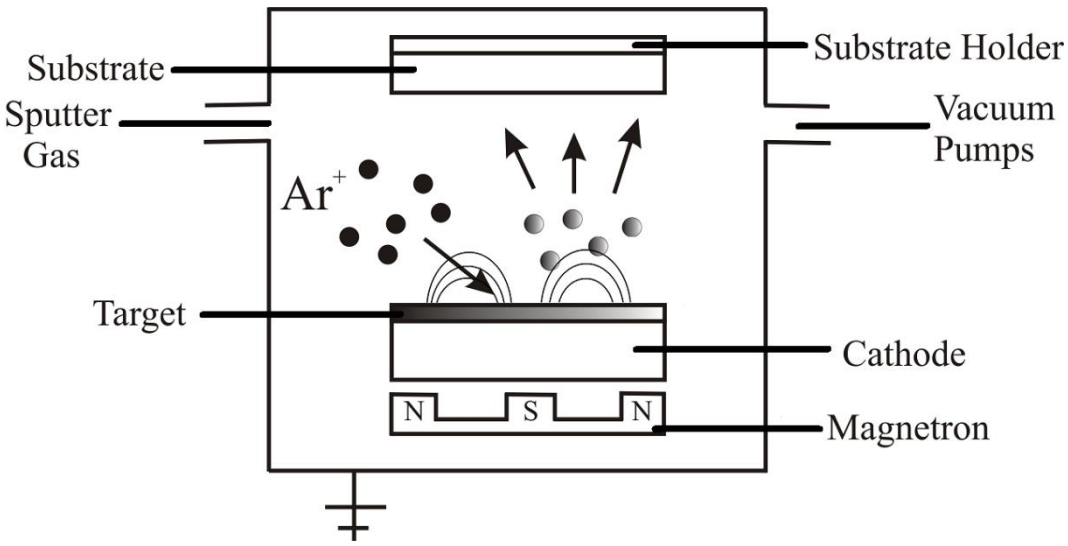


**Figure 60: Schematic of magnetron.**

If a compound target is used which has atoms of significantly different sizes, then they will sputter at a different rate. However, when the target becomes particularly rich in one type of atom, its rate of sputtering increases so an equilibrium is achieved. This process does have one consequence which is that a new target has to be 'conditioned' before use. This means it has to be exposed to plasmas for up to 30 minutes before sputtering so that the surface can reach its ideal state.

### 5.1.2 HiTUS Sputtering

The samples studied for this research were grown by using a sputtering system called a HiTUS. The name HiTUS stands for High Target Utilisation and comes from the fact that unlike a magneton sputterer, which uses only a small fraction of the target, up to 95% is used (Figure 61). As can be seen, the system consists of a side arm where the plasma is generated remotely. The Argon plasma is generated by a helically wound three turn antenna which is powered by a 13.56 MHz, 2.3 kW RF power supply. There is also a matching unit between the power supply and antenna to ensure that the power supply experiences a constant load.

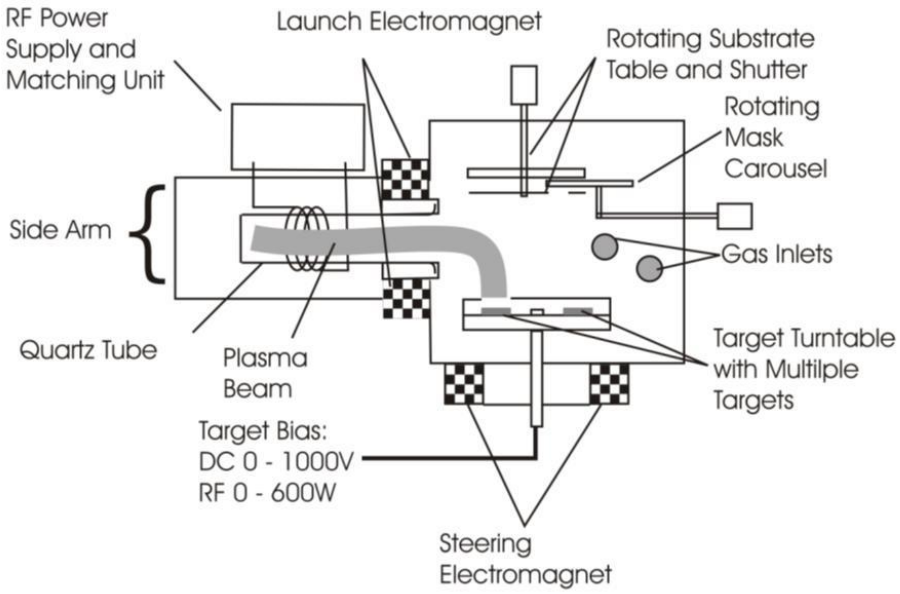


**Figure 61: Schematic of HiTUS sputtering system [*Vopsaroiu,2005(a)*].**

The plasma is launched into the main chamber by virtue of the launch electromagnet and is then guided onto the target by the steering magnet, of strengths 500 Oe and 50 Oe respectively. The $Ar^+$ ions follow a chiral path along the field lines generated by the magnets and are contained by the coupled magnetic flux lines between the magnets, with the resulting beam having a 6 cm cross sectional diameter. Due to the plasma being generated remotely, a density of $10^{12}$ – $10^{13}$ ions/cm$^3$ can be achieved as opposed to a conventional magnetron system which only reaches $10^{10}$ ions/cm$^3$ under the same working conditions [*Vopsaroiu,2005(a)*].

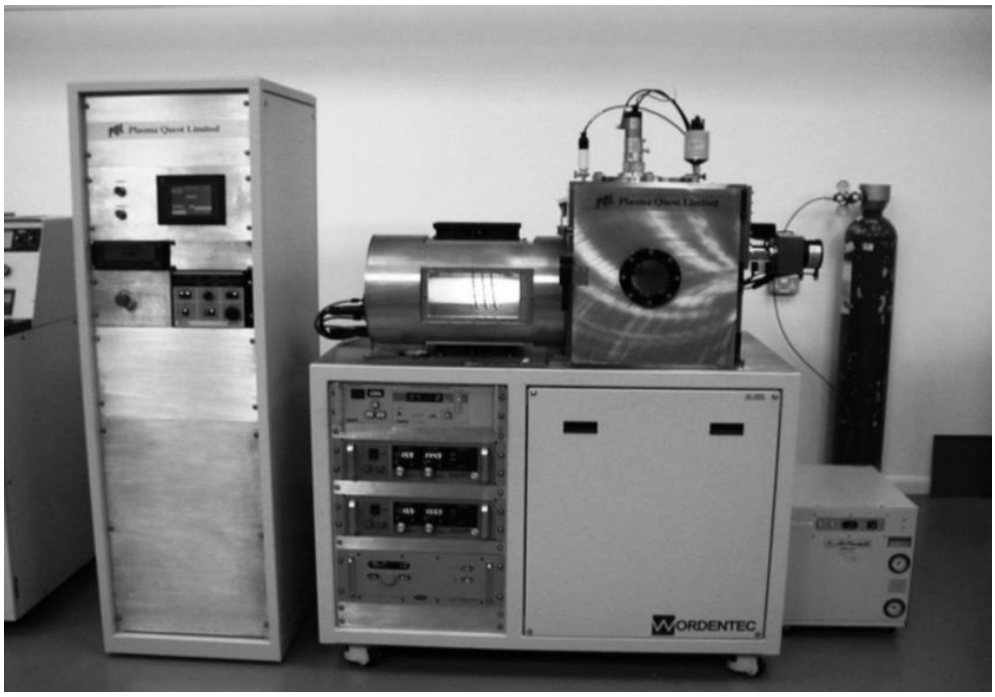


**Figure 62: Photo of HiTUS sputtering system.**

A negative bias is then applied to the target and, as can be seen in Figure 63, the target current saturates at around 100V. This means that potentials of up to 1000V can be applied to the target without affecting the plasma density, and varying this actually becomes the primary method of controlling the grain size of the sputtered films. The substrate is held 20cm above the target, this means the beam of

impinging atoms is very uniform across and results in the sample having a very flat surface.

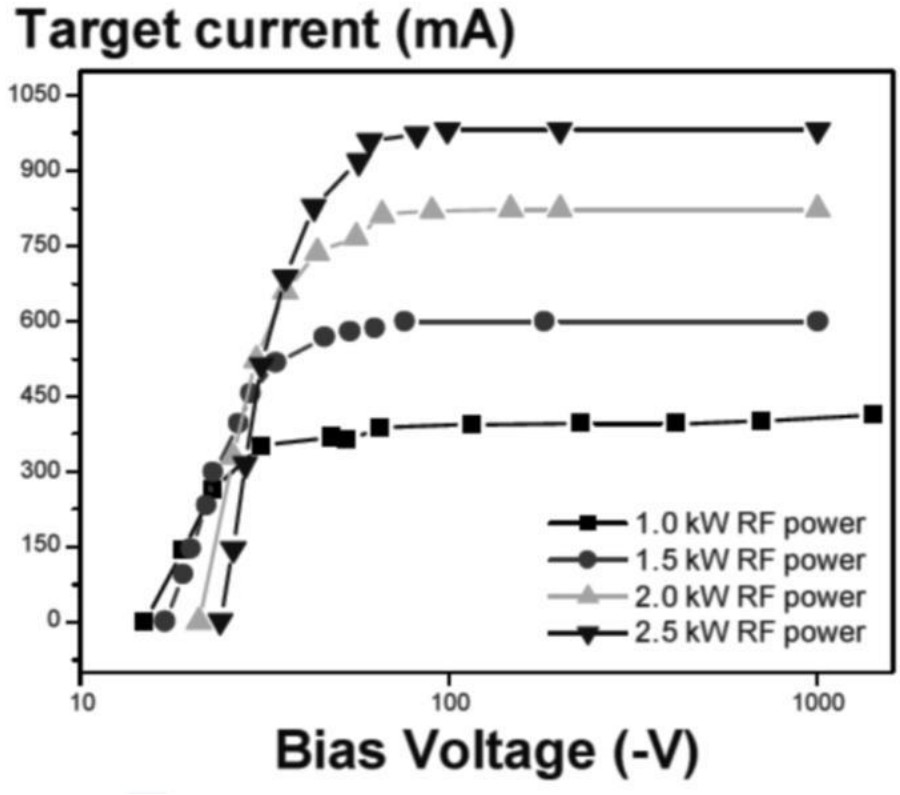


**Figure 63: Target current versus bias voltage [*Vopsaroiu,2005(b)*].**

### 5.1.3 Control of Grain Size

There are three different ways in which the rate of sputtering can be varied, either increase the radio frequency power, increase the process pressure, or increase the voltage applied to the target (see Figure 64, Figure 65 and Figure 66). The first two of these methods result in a change in the density of the plasma. The third, however, only increases the energy of the plasma. Although varying the RF power gives the widest range of grains sizes, the stress such changes put on the matching unit can be avoided by only varying the bias voltage, so this is how the grain sizes were controlled.

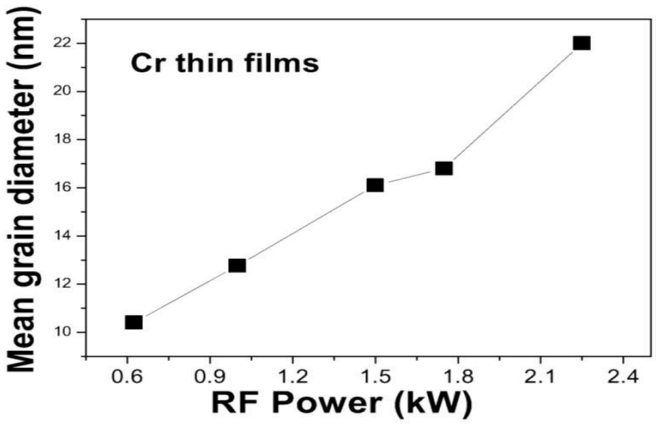


**Figure 64: Mean diameter as a function of RF power [*Vopsaroiu,2004*].**

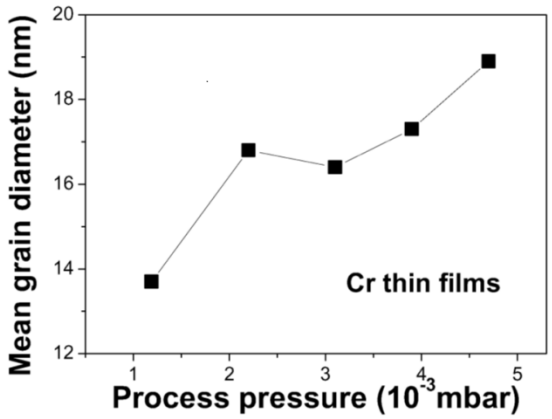


**Figure 65: Mean diameter as a function of process pressure [*Vopsaroiu,2004*].**

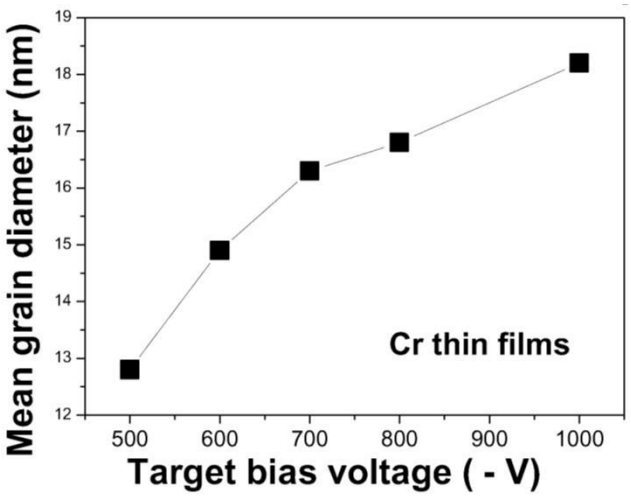


**Figure 66: Mean diameter as a function of bias voltage [*Vopsaroiu,2004*].**

Although it has been shown that the target bias voltage gives some control over the mean grain diameter, the actual growth mechanism is not fully understood. The system's growth rate monitor confirms that the higher the bias voltage, the faster the rate of deposition, and this results in larger grains.

It is believed that the variation of growth rate could be related to crystal symmetry. The crystals which form at a higher growth rate show a higher level of symmetry, therefore adjacent crystals are then more likely to fuse together. X-ray diffraction has also confirmed that the larger crystal do show greater crystallinity.

The growth rate is monitored by an INFICON XTM/2 Deposition Monitor. This comprises of a quartz crystal that is subject to an a.c. voltage which causes it to oscillate. This rate of oscillation will vary as material is deposited upon it according to the following equation

$$\frac{M_F}{M_Q} = \frac{(\Delta F)}{F_Q} \qquad \text{Eqn. 5-1}$$

where $M_F$ is the change in the mass due to deposition, $M_Q$ is the original mass of the quartz crystal, $\Delta F$ is the change in frequency of the crystal and $F_Q$ is the uncoated resonant frequency of the crystal [*Sauerbrey,1957*]. The crystal rate monitor cannot be located directly next to the substrate so a tooling factor is incorporated in the calculation to take this into account.

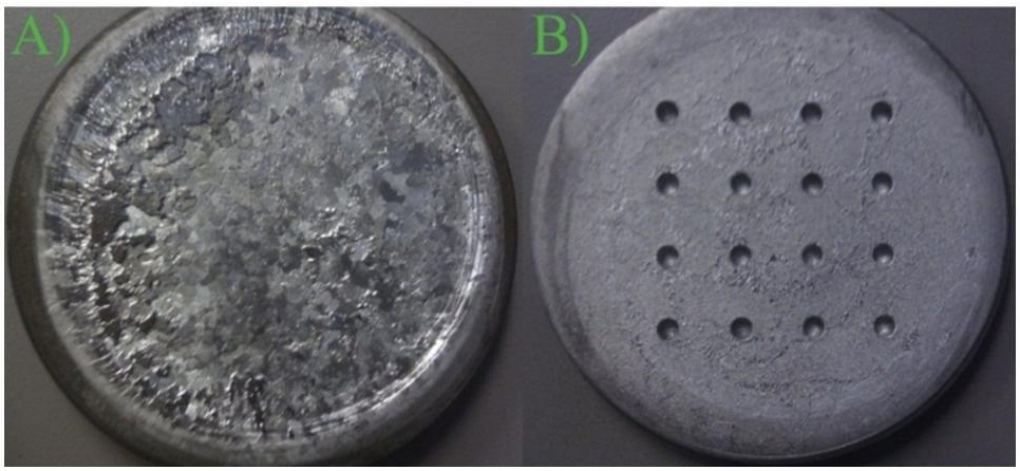


**Figure 67: Picture of normal and composite target.**

It is possible to introduce impurities into a deposited layer in a controlled manner. This is done so that the effect of these impurities on, for example, the anisotropy of Iridium Manganese can be investigated (section 4.2.2). Figure 67 shows an array of 16 holes that were drilled into a target, small pegs of pure copper can then be inserted into the holes. The concentration of impurities within the sample can be determined by using Energy Dispersive X-ray Analysis (EDX).

### 5.1.4 Pressure and Regeneration

The whole chamber and side arm is pumped down to a base pressure of less than $5x10^{-7}$ mbar by three different pumping systems which are used sequentially. The first is a rotary pump, the second a turbo pump, and the third is a Helium cryopump. For deposition, however, a process pressure of around $2x10^{-3}$ mbar is used (see Figure 65 for effects of varying this value). This pressure is maintained by a Mass Flow Controller which is set to 10sccm. During deposition, the opening to the Helium cryopump is set to a 'half open state' where the aperture is large enough for a low pressure to be maintained, but not so large that plasma can enter into it. If this occurs and the cryopump warms up to above 20K, then a 2 hour regeneration process needs to be carried out so that it can return to is operating temperature of ~ 10K.

## 5.2 Vibrating Sample Magnetometer

### 5.2.1 Principles of Operation

The concept of a vibrating sample magnetometer (VSM) was first proposed by Foner in 1956 [*Foner,1956*]. It is based upon Faradays electromagnetic law of induction where if a magnetic sample experiences a changing magnetic field then an electromotive force (emf) is produced which is proportional to the magnetic moment of the sample. The equation, takes the following form

$$emf = -N\frac{d\varphi}{dt}m \qquad \text{Eqn. 5-2}$$

where $N$ is the number of turns in the coils, $\Phi$ is the magnetic flux and $m$ is the moment. The original design used a speaker to generate the oscillations at a set frequency. This is usually chosen to be around 81 Hz so there is as little electrical interference from mains frequencies as possible. The amplitude of oscillation can be anywhere between 0.1 to 2 mm. The sample is then vibrated within a field which is as uniform as possible. To ensure this, accurate centring procedures must be followed.

### 5.2.2 Layout of Components

For a non-vector system four detection coils are placed either side of the sample. They are wound in series opposition so the electromotive force induced in the coils by external stray magnetic fields cancel each other out, whereas that induced by a sample with in them add together. There is also a reference sample near the

top of the oscillating sample holder which is also placed between two more detection coils. This is done so that changes in vibration amplitude and frequency can be accounted for.

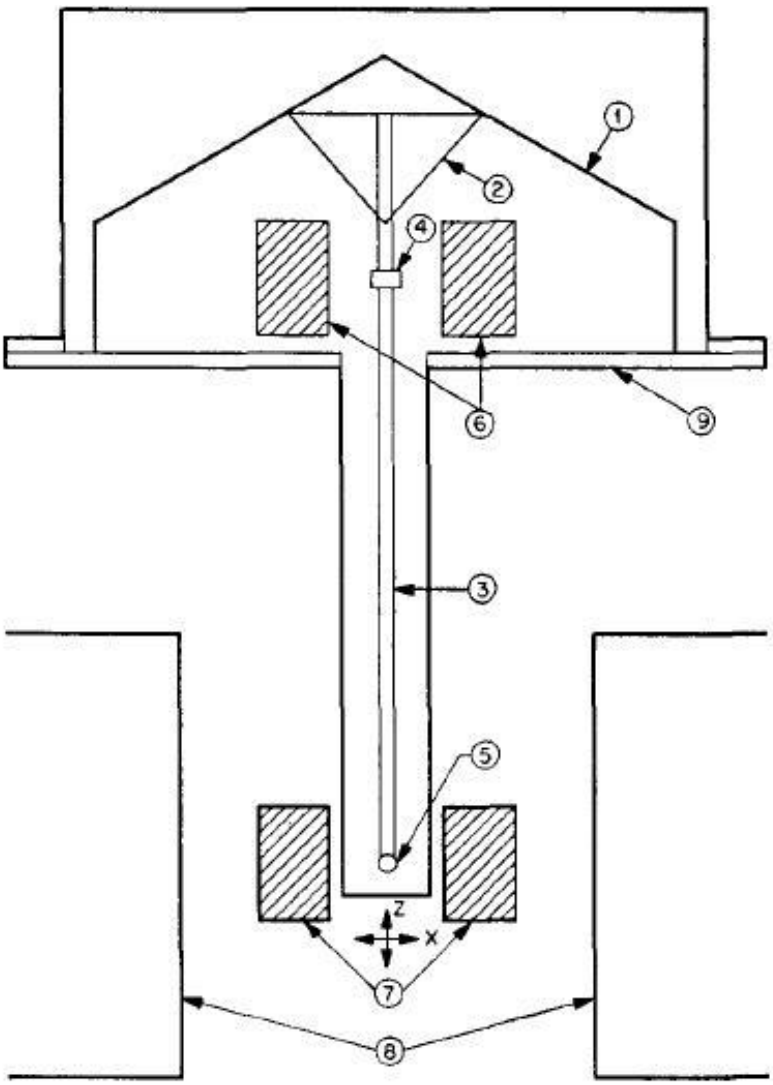


FIG. 1. Simplified form of vibrating-sample magnetometer. (1) loud-speaker transducer, (2) conical paper cup support, (3) drinking straw, (4) reference sample, (5) sample, (6) reference coils, (7) sample coils, (8) magnet poles, (9) metal container.

**Figure 68: Schematic of VSM [*Foner,1956]*.**

### 5.2.3 Calibration

Calibration of such an instrument is complex since during operation there are a number of different interacting systems. For example, it is important to accurately know the magnetic field being applied, however, this means the Hall probe and gaussmeter being used must first be calibrated against external references. Once this is done a calibration sample can be used to calibrate the actual moment measured.

Different calibration samples have different advantages. A Nickel sample easily reaches saturation magnetisation which then remains constant for a wide range of fields. The disadvantage is that the total moment is much larger than the moments measured in the thin films produced in this project. To successfully calibrate very small moments, a Pauli paramagnet is used such as Palladium, which has a number of useful characteristics. By accurately measuring the mass of the sample, its susceptibility can be calculated and, as its magnetisation is proportional to the field being applied, a range of small calibration values can be obtained. This susceptibility is largely temperature independent at measurement conditions, also Palladium does not corrode.

It is preferential for the calibration sample to be of a similar size and shape to the samples that are to be measured, this is so that each sample experiences the same demagnetising field effects. Once the magnetometer has been calibrated with the calibration sample, a further measurement has to be taken of just the sample holder so that this contribution can be subtracted from the final measurement.

### 5.2.4 Microsense Model 10

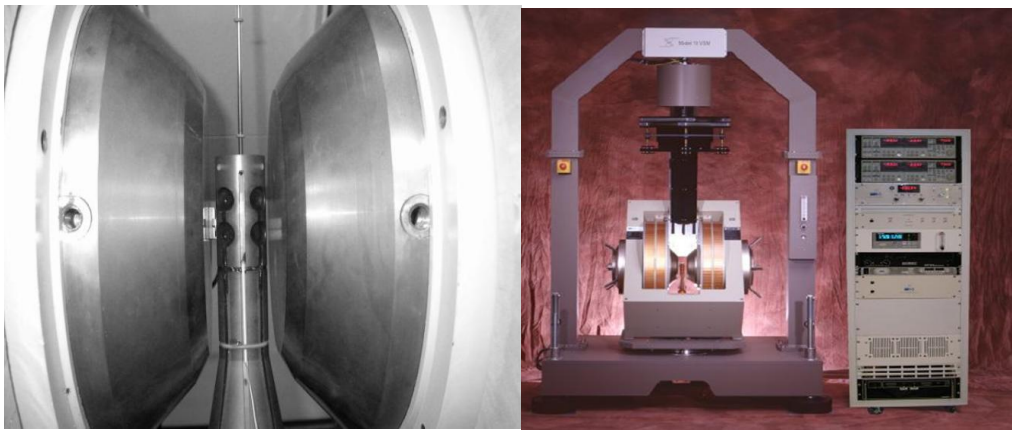

**Figure 69: Pick up coil configuration of Microsense Model 10.**

The vibrating sample magnetometer used for the measurements in this project was a Microsense Model 10 which, although based on the same basic principles, is significantly more advanced than earlier models. Rather than four measurement coils, there are eight placed orthogonally to the sample (Figure 69), this means that vector measurements can be made with an accuracy of better than +/- 1.5%. The magnets are located on a rotating plate which gives them +/- 540$^{o}$ freedom, finding the easy axis of a sample can therefore be carried out simply. The sample chamber has a temperature range of 100 K to 770 K with a stability of +/- 1K, the value of which is determined by a Proportional Integral Differential controller (PID).

In a PID, the first term relates to the difference between the set point temperature and the actual temperature; the second term sums the difference between the set point temperature and actual temperature over time; the third term is related to the rate at which the actual temperature is approaching the set point temperature. This system, along with the sophisticated software, is the magnetometer's most

important capability for the purposes of the research performed in this work. Complicated measurements which require a variety of accurately known setting temperatures can be programmed to run for any duration of time. These procedures can be run over night, resulting in a high volume of measurements being produced.

## 5.3 Alternating Gradient Force Magnetometer

### 5.3.1 Principles of Operation

The concept of the first alternating gradient force magnetometer (AGFM) was thought of by Zijlstra [*Zijlstra,1970*] where a microscopic magnetic particle was attached to the end of a thin wire. A non-homogeneous magnetic field was applied and the deflection of the wire was observed by the means of a microscope. The idea was developed further in 1988 where a piezoelectric element, rather than a microscope, was used to measure the movement of the sample [*Flanders,1988*]. It operates according to the following principles. The force experienced by a magnetic sample is proportional to the gradient of the field applied (Equation 5-3)

$$F_x = m_x \frac{dH_x}{dx} \qquad \text{Eqn. 5-3}$$

where $F_X$ is the force, $m$ is the magnetic moment and $\frac{dH_x}{dx}$ is the gradient of the magnetic field. Clearly, if both the gradient of the applied field is known along with the force that is generated, then the magnetic moment of the sample can be deduced. Once placed in the magnetometer, the sample is subject to two fields. One is a large direct field and the second is a small alternating field. The small alternating field results in the oscillation of the sample which is a function of the force it experiences. This deflection is measured by the voltage of the piezoelectric element in the sample holder (Figure 70).

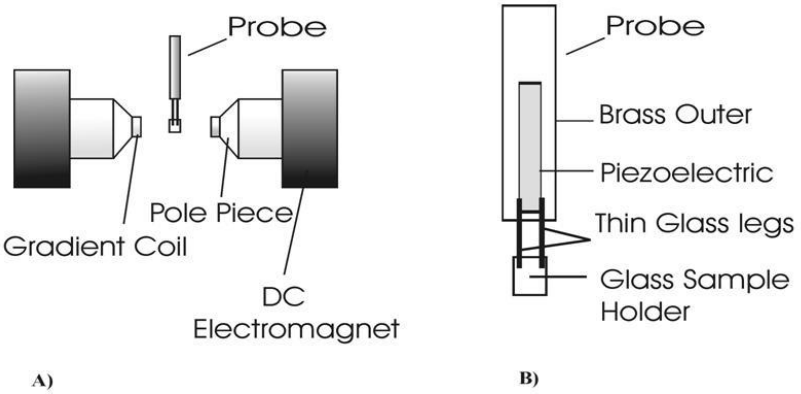


**Figure 70: AGFM Schematic** (*Figure a shows the location of the probe within the pole pieces, Figure b shows the layout of the probe itself*)**.**

Prior to the actual measurement being taken the fundamental resonant frequency ($f_o$) of the system has to be found. During this the large dc field is held constant and the small ac is field varied from 100Hz to 1000Hz until the resonant frequency is found. This is actually determined by which frequency has the highest Q factor, values can vary from 10 to 100 and can depend on an number of elements. Equation 5-4 describes the value of $f_o$ where *Y* is the Young's modulus, $\rho$ the density, *w* the width and *l* the length of the quartz legs of the probe.

$$f_o = \frac{1}{2\pi}\frac{w}{l^2}\left(\frac{Y}{\rho}\right)^{1/2} \qquad \text{Eqn. 5-4}$$

### 5.3.2 Advantages and Disadvantages of AGFM

The alternating gradient force magnetometer used for some of the magnetic measurements in this project was a Princeton Measurements Corporation Model 2900. The advantages of this apparatus are that this non-inductive method can be up to 100 times more sensitive than if the sample is vibrated in a conventional way and is much quicker than a super conducting interference device

magnetometer (SQUID). This means that it is useful for time dependent measurements and for sample screening. The disadvantages are its sensitivity is so high that back ground acoustic interference can result in noise in the measurement. The other restriction is that it is not an easy procedure setting it up to carry out temperature measurements, therefore the Model 10 VSM was primarily used.

## 5.4 Transmission Electron Microscope

### 5.4.1 Principles of Operation

The first transmission electron microscope (TEM) was invented by Knoll and Ruska in 1932 [*Knoll and Ruska,1932*] and in less than four years it was being produced commercially. They have been continually developed over the years and, despite high running costs, have found themselves to be an invaluable research tool. For an optical microscope the resolution, δ, is given by the Rayleigh criterion

$$\delta = \frac{0.61\lambda}{\mu \sin \beta} \qquad \text{Eqn. 5-5}$$

where $\lambda$ is the wavelength of the radiation, $\mu$ the refractive index of the viewing medium and $\beta$ is the semi angle of collection of the magnifying lens. With the use of green light this gives a resolution limit of around 300nm. By utilizing the wave properties of electrons and by applying the de Broglie relationship

$$\lambda = \frac{h}{mv} \qquad \text{Eqn. 5-6}$$

where $\lambda$ is wavelength, $h$ is Planck's constant, $m$ is the mass of a particle moving at a velocity $v$, a theoretical resolution limit for a 100-keV electron beam can be calculated to be around 0.004nm [*Williams,1996*]. Although this limit can never been achieved in reality, the JEOL JEM FS2200 Cs double corrected microscope in the York-JEOL Nano centre can achieve a resolution of 0.8 nm which gives sub atomic resolution. The limiting factor of the resolution is not, in fact, the wavelength of the electrons; rather it is the performance of the electron lenses. There are two main types of aberrations that occur, chromatic and spherical. Chromatic aberrations can be reduced by using an electron source with as narrow an energy spread as possible. Spherical aberrations have to be corrected by extra lenses.

### 5.4.2 Layout of TEM

The electron source for the microscope used in this project (*JEOL JEM – 2011*) was a thermionic gun using a $LaB_6$ filament. The filament is heated resistively to operating temperature and is held at a voltage of 100kV with respect to the anode. Surrounding the tip of the filament is a Wehnelt cylinder whose purpose is to help focus the emitted electrons. The electrons then pass through a condenser lens, the sample itself, and a number of other lens systems until they impinge on a fluorescent projection screen or digital camera. Electrons can be focussed by the use of electrostatic fields, however, in this microscope only magnetic lenses are used (Figure 71).

As has been mentioned before it is the quality of the magnetic lenses that determines the resolution of the instrument. The various issues that arise are spherical aberration, chromatic aberration and astigmatism. How successfully a microscope deals with these problems determines the quality of the instrument.

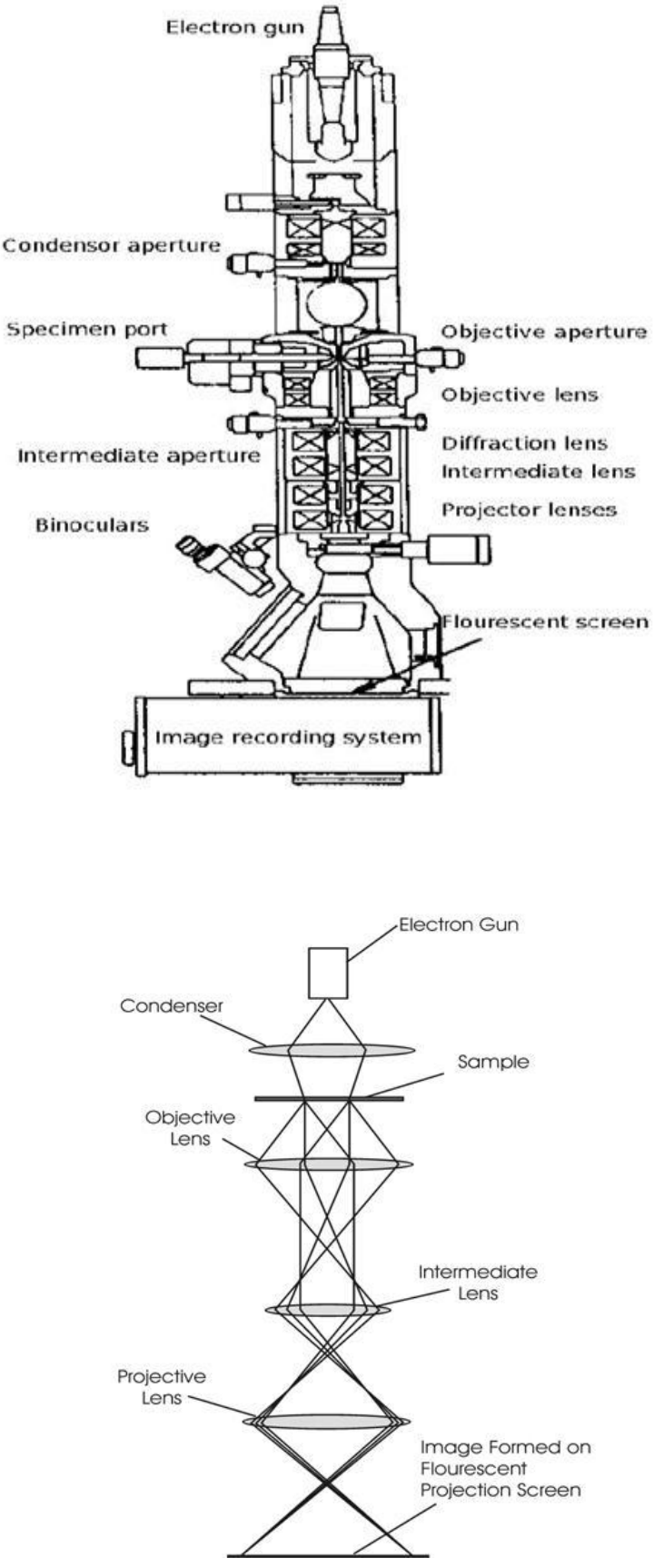


**Figure 71: TEM schematic and lens diagram [*Williams,1996*].**

### 5.4.3 Imaging Mode

There are many ways in which the electrons can be used to elucidate information from a sample. These include, amongst others, Electron Energy Loss Spectroscopy (EELS), High Angle Annular Dark Field Imaging (HAADF) and diffraction patterns. The primary method used for this project was bright field imaging which is the method most similar to a normal optical microscope. An image is formed of the sample which results from two different types of contrast.

The first is mass-thickness contrast, the other is Bragg diffraction. Mass-thickness contrast comes from the incident electrons being scattered by interactions with atomic electrons in the sample. The degree of scattering is a function of both the atomic number of the material and its thickness and is primarily used in non-crystalline samples.

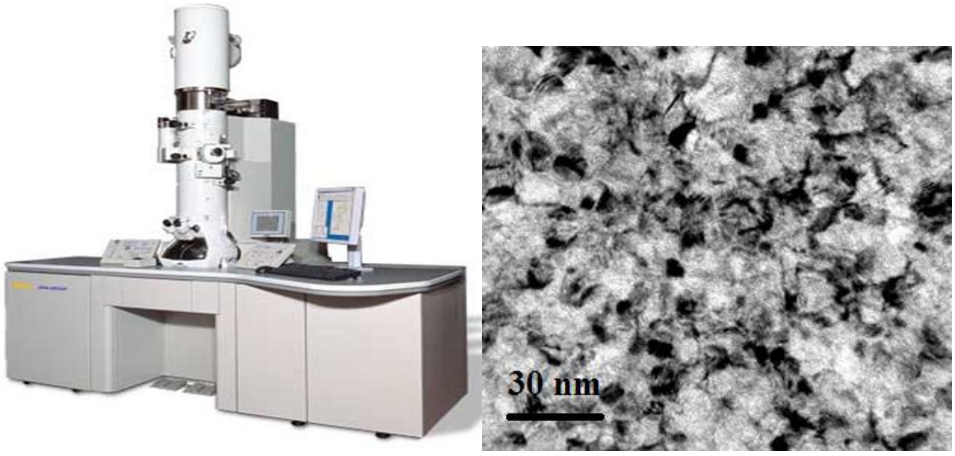


**Figure 72: Picture of JEOL JEM 2011 and a typical bright field image.**

The second contrast is by virtue of Bragg diffraction where the electrons are reflected off crystallographic planes according to Bragg's Law

$$N\lambda = 2dsin\theta \qquad \text{Eqn. 5-7}$$

where $d$ is the lattice spacing, $\theta$ the angle between the wave vector of the incident plane wave and the lattice planes, $\lambda$ the wave length and $n$ is an integer. Crystallographic regions will therefore be seen as dark areas on the image, whereas amorphous regions will appear brighter. This means that the images can be used to determine the size distribution of the crystallographic regions in the sample.

### 5.4.4 Dark Field

To achieve high quality pictures, various apertures can be inserted to limit the number of electrons that form the final image. Figure 73 shows how, if the electrons undergo Bragg diffraction, they are not included in the final image due to them being absorbed by the objective aperture.

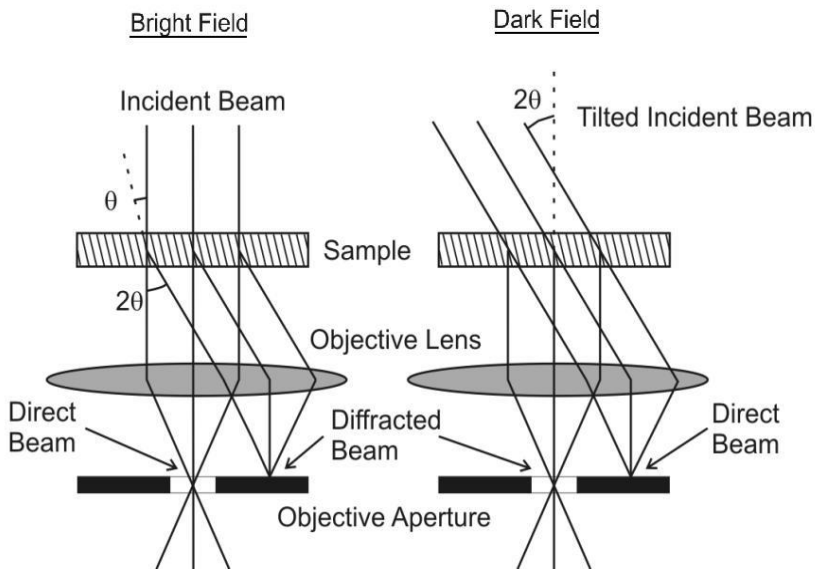


**Figure 73: Diagrams of bright field and dark field imaging set up [*Williams,1996*].**

However, if the objective aperture is placed so that only the diffracted electrons can pass through it, then a dark field image is obtained. Here, the amorphous regions appear dark and the crystallographic regions appear bright, similar to a negative. This technique can be used to confirm that the dark area being examined is, indeed, crystallographic. However, this method is not completely fail safe as the crystallographic orientation of the region does have to be in a direction such that the diffracted electrons do go through the aperture.

# 6. Results

## 6.1 Median Blocking Temperature Measurements

### 6.1.1 Introduction

The work by *O'Grady et al.* describes the effect of the bulk of the antiferromagnet on the exchange bias of polycrystalline thin film media. The primary aim of this work is to further understand the role of the interface, and more specifically, the interfacial spin clusters in these systems. During the course of this project attempts were made to investigate the magnetic nature of the spin clusters by use of neutron diffraction. Unfortunately, the equipment was not sensitive enough to detect them, therefore, other methods of characterisation have been employed. Like the bulk of the antiferromagnet, the interfacial spin clusters cannot be directly measured in a vibrating sample magnetometer. So, just like the bulk, their characteristics have to be inferred from their effect on the ferromagnet, and primarily the coercivity and exchange bias. However, there are two difficulties that present themselves here. The first is that of isolation. The challenge here is to work out how the effect of the interfacial spin clusters can be separated from the bulk. The second is that the effect of the clusters can sometime be very small. These two issues have to be solved before a reasonable characterisation of them can be achieved. The following chapter explains how these challenges have been overcome.

### 6.1.2 Sample Structure

The samples used throughout the following measurements are all very similar in nature, except for one set which needed a small change (Figure 74). There are all grown on a 5mm x 5mm silicon substrate in the HiTUS with a magnetic field of 500 Oe applied during deposition. This was done in order to induce a known direction of the easy axis, an advantage the HiTUS has over a magnetron

sputterer. 5 nm of Tantalum was deposited on the silicon, the purpose of this was to smooth out the rough surface of the silicon then on top of this, 5nm of Ruthenium was deposited. There are three main seeds layers that could be chosen, Copper, Ruthenium and Nickel Chromium. It has been shown that a Copper seed layer results in the lowest quality of crystallinity in the Iridium Manganese and the Nickel Chromium results in a much smaller medium grain size [*Aley,2008(a)*]. Therefore, as a compromise, Ruthenium was chosen and in order to maintain consistency was used in all measurements. As was mentioned in section 4.2.1, 5 nm was deposited as it has been shown that the crystallinity of the Iridium Manganese improves up to this thickness of seed layer but beyond this, no noticeable improvement is seen.

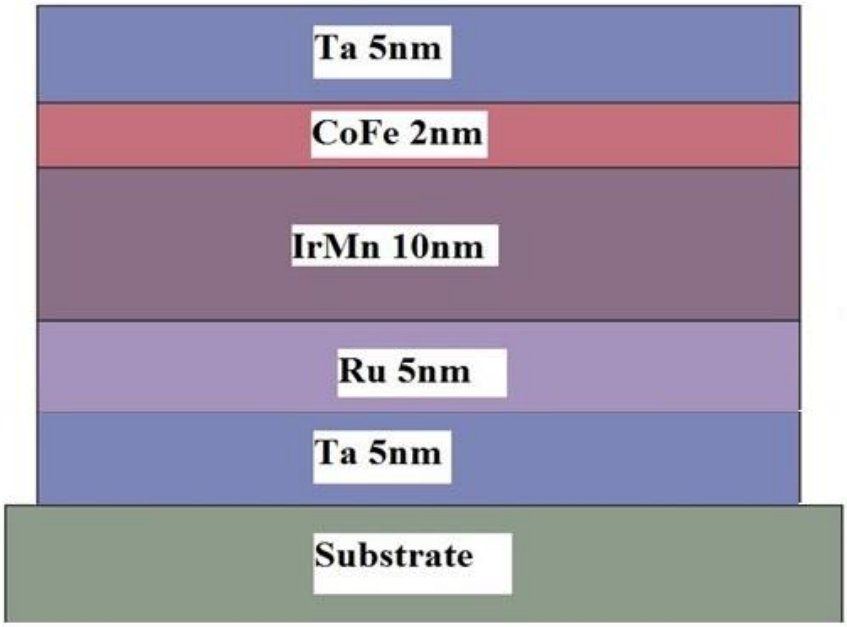


**Figure 74: – Structure of samples**

Iridium Manganese was used as the antiferromagnet because it is highly resistant to corrosion and is the choice of industry. However, there are some considerations to be made when choosing the thickness of the antiferromagnet. All of the subsequent measurements could be carried out again, but with varying thicknesses

of the antiferromagnet. The justification for this is simply that by reducing its thickness, the bulk effects are reduced and so the interfacial characteristics are effectively increased. There is a good argument here and, if time were not an issue, this might have been done. However, for these samples, a standard thickness of 10nm was chosen and used throughout the experiments. The reason for this is an attempt to solve the challenge posed earlier, which is to isolate the effects of the interface from the bulk. By using a 10nm thickness, the majority of the grains in the sample are stable at around room temperature and can be set in a known state without too much difficulty [*Vallejo-Fernandez,2007*]. If the bulk of the antiferromagnet can be set then any effects that are witnessed during an experiment can be attributed to the interface. This is not an exact method and bulk effects still need to be considered, but it is the decision that was taken before growing the samples and it was continued throughout, again, in order to maintain consistency.

In previous works that have been carried out on this topic by this research group, Nickel Iron was chosen as the ferromagnet [*Fernandez-Outon,2008*]. However, Cobalt Iron was chosen for these samples because its moment is four times higher and it is used in industry. The higher moment also becomes very significant in some of the later experiments. Various thicknesses could have been chosen in order to gain the same results, however, 2nm was primarily used throughout the experiments. The inverse relationship between the exchange bias and the thickness of the ferromagnet means the ferromagnetic layer should be as thin as possible. The Microsense Model 10 VSM can comfortably measure a 2nm Cobalt Iron layer, which results in an exchange bias of around 500 Oe. For the last set of measurements a Princeton magnetometer was used which had a lower sensitivity, and also the sample was placed inside a cryostat. Here, 2nm of Cobalt Iron was not enough to take the measured signal above the noise base so various thicknesses were experimented with and, in the end, 10nm was chosen as a balance between having a large enough moment along with a large enough exchange bias.

### 6.1.3 Sample Variation

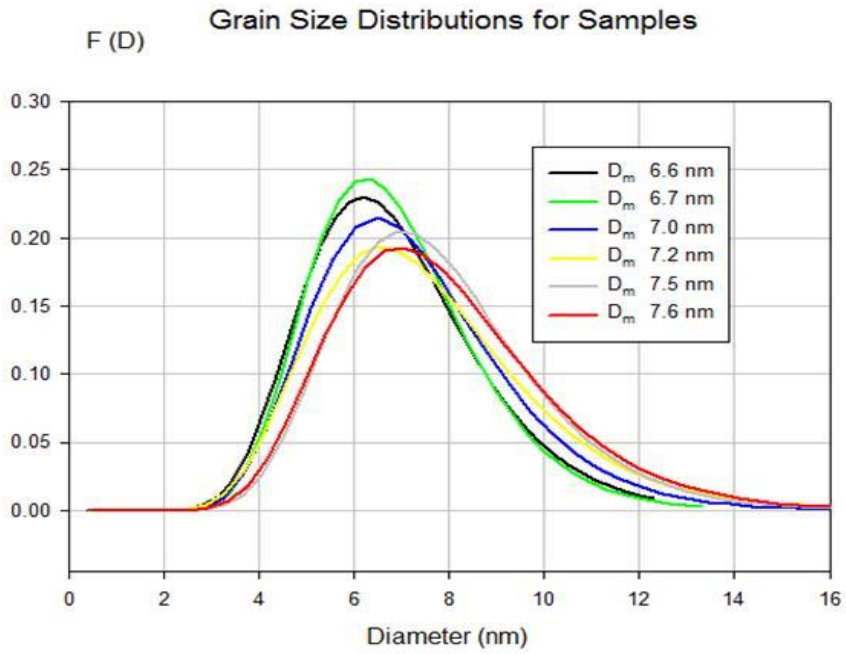


**Figure 75: Log normal distributions for the six samples [*Cramp,2012*].**

The previous section describes the common aspects of all the samples, this section briefly describes the variation within a set of samples. As was described in part 5.1.2, the HiTUS can be used to vary the grain size distribution, and as was described in section 4.1.4, this log normal distribution can be described by two parameters, its mean and its standard deviation. Although there is some control with regards to the mean grain size, there is no control over the standard deviation and what is produced has to be accepted in this. However, by varying the bias voltage applied to the target during deposition, the medium grain size can also be varied. Figure 75 shows the log normal distributions of the diameters for the first set of samples. As can be seen there is only a small increase in the diameter (~1nm), but this corresponds to a 30% increase in volume.

The assumption is now interfacial spin clusters sit on the grains and are of the same diameter. The hypothesis is then size dependent interfacial spin clusters effects can be seen, once isolated from bulk effects.

### 6.1.4 Blocking Temperature Distribution

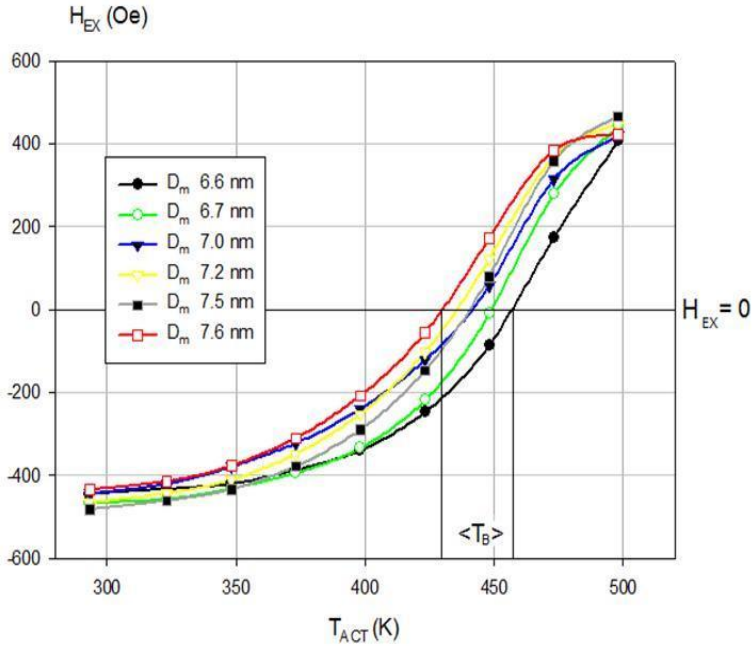


**Figure 76: Blocking temperature measurements [*Cramp,2012*].**

The grain size analysis performed in the previous section is a standard procedure carried out on all samples. The blocking temperature measurements described in this section are also standard procedures which are detailed in section 4.1. As can be seen from Figure 76, all of the curves have flattened off by around 300K which means the bulk of the antiferromagnet is stable at this temperature and justifies the earlier decision to use 10nm of antiferromagnet. If an experiment can now be devised which highlights the effect of the interfacial spin clusters, hysteresis loops can now be taken at room temperature safe in the knowledge that the bulk of the samples are stable and can therefore be ignored. Being able to do this can save a great deal of time, effort and resources. Having said that, the number of measurements actually carried out at room temperature throughout the rest of this chapter is in the minority. As can be seen from the graph, the curves have only just started to flatten out at room temperature and so, clearly, any further reduction in measurement temperature would be welcome.

### 6.1.5 Anisotropy Calculations

When the medium grain size values are combined with the medium blocking temperature values, the anisotropy of the antiferromagnet can be determined by application of Equation 6.1 as described in section 4.1.6

$$K_{AF}(< T_B >) = \frac{k_B < T_B > \ln(t_{<T_B>} f_o)}{V_m} \qquad \text{Eqn. 6.1}$$

Table 6 shows the median diameter, median volume, median blocking temperature and anisotropy values. The anisotropy values show a curious behaviour in that they decrease as the gain volume increases. Ideally, it should be a constant, however, it is calculated individually for each sample and, due to the variations in the crystallinity of each sample, the anisotropy varies. This decrease is not easily understood, one explanation is that there is a slight size dependence on the anisotropy. However, if this is the case, this variation in the anisotropy of the bulk has no effect on the rest of this work which concentrates on the interface.

| $D_M$ *(nm)*±0.1 | $\sigma_{lnD}$ ±0.01 | $V_M$ *($nm^3$)*±7 | $\sigma_{lnV}$ ±0.03 | $<T_B>$ (K)±5 | $K_{AF}$*(293K)* *(±0.5×$10^6$ ergs/cc)* |
|---|---|---|---|---|---|
| 6.6 | 0.27 | 342 | 0.81 | 456 | 1.1 |
| 6.7 | 0.25 | 352 | 0.75 | 448 | 1.0 |
| 7.0 | 0.28 | 385 | 0.84 | 440 | 0.9 |
| 7.2 | 0.30 | 407 | 0.90 | 434 | 0.8 |
| 7.5 | 0.27 | 442 | 0.81 | 439 | 0.7 |
| 7.6 | 0.28 | 454 | 0.84 | 430 | 0.6 |

**Table 6: Key parameters for the samples.**

### 6.1.6 Coercivity Variation

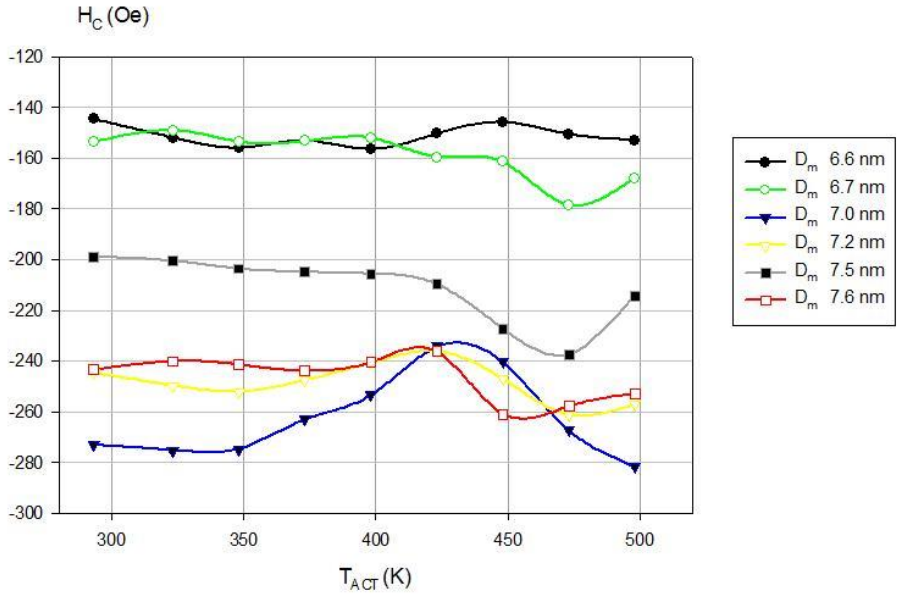


**Figure 77: Coercivity vs activation temperature.**

Although the blocking temperature measurements are not the core result of this section, it was possible to analyse the results slightly further than is usually performed. The key aspects of the blocking curves are the exchange bias and activation temperatures, yielding the median blocking temperature. However, a relatively simple analysis of the data gives the variation of the coercivity. This is examined in more detail in further experiments later on, so it is of some value to start considering it now. There is no real trend between the grain size and coercivity, however, it does show variations around the median blocking temperature. At this value, equal proportions of the antiferromagnet are set in opposite directions, hence the reduction of the exchange bias to zero. What is not known is the state of the interfacial spin clusters. It is assumed that they are also in a state where half are magnetically ordered in one direction and the other half in the opposite direction. The fact that some of the samples show an increase in coercivity at this point and some show a decrease is not fully understood. However, as will be examined later on, the coercivity is believed to be strongly related to the interfacial spin clusters and, therefore, the figure does seem to suggest that they go through a degree of re-ordering around the median blocking temperature.

### 6.1.7 Field Dependent Measurements

For the previous set of measurements, the field which was applied during the setting process was 2000 Oe. This was chosen in order to ensure that the ferromagnet was fully saturated and is clearly sufficient as it is possible, within the maximum limits, to set the exchange bias to any value desired. It has been known by industry for some time that if a large field of, for example, 50000 Oe is applied during the annealing process, the exchange bias of the pinned layer in the spin valve is increased. If this increase is sufficient, it can then lead to a reduction in the thickness of the antiferromagnet in order to reach the required amount of exchange bias. This then means the size of the read head can be reduced along with the amount of material used. The rest of section 6.1 is now going to give an explanation as to why this increase in setting field leads to an increase in exchange bias.

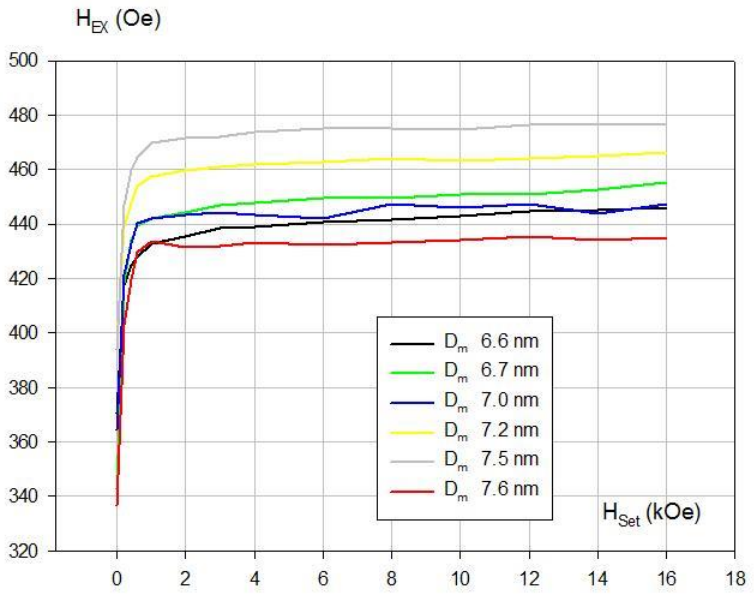


**Figure 78: $H_{SET}$ results.**

The samples used here were grown concurrently with the samples in the previous section and, therefore, experienced exactly the same growth conditions. They are not the same samples, however, as it has been found the subsequent measurements

can only be carried out once on a sample. The measurements can be repeated, but only with new samples, which suggests that some irreversible process occurs in them during the measurement.

The measurement procedure is to set the sample in a positive field for 90 minutes at 225$^{o}$C and then field cool the sample down to the measurement temperature of 30$^{o}$C, remove the training effect, and then take a hysteresis loop. This is then repeated for increasing sizes of setting field. 90 minutes and 225$^{o}$C were chosen to correspond to the standard setting time and temperature of previous work [*Vallejo-Fernandez,2008(d)*]. For some of the measurements the training effect was investigated, however, no correlation was seen between either setting field or grain size

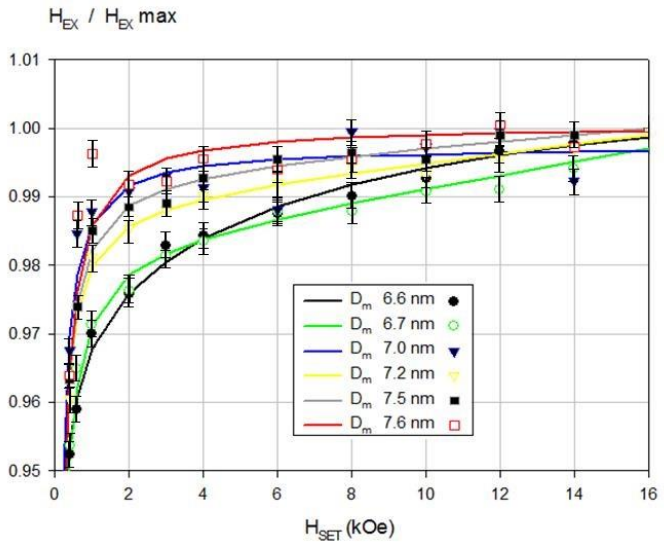


**Figure 79: Expanded $H_{SET}$ results [*Cramp,2012*].**

Figure 78 shows the raw data from the measurements and, given that there is no correlation between the maximum exchange bias and the grain size, there does not seem to be a great deal of value in them. However, if the measurements are normalised to the maximum exchange bias and the area of the graph where the exchange bias varies the most is expanded, then a grain size dependent trend can be seen (Figure 79). The lines in Figure 79 are guides to the eye.

### 6.1.8 Interfacial Spin Clusters

As has already been said, the field that needs to be applied to a ferromagnet in order to modify the state of the adjacent antiferromagnet is around 1000 Oe. The minimum amount can actually be less than that as all that is actually required is that the ferromagnet is saturated. The question that arises then is, why does the exchange bias continue to increase under a setting field greater than the ferromagnetic saturation value. There must be some component of the system that is responding to the magnetic field. Given that in the bulk of the antiferromagnet, each magnetic plane is compensated by an adjacent opposing one, and an antiferromagnet gives no magnetic signal in a magnetometer, what part of the bilayer is responding to the field. There must be some other part which has magnetic properties.

It has been suggested that at the interface between the antiferromagnet and ferromagnet, interface spin clusters form [*Baltz,2010*]. As these samples are polycrystalline and grown by sputtering, there will be both magnetic sublattices of the antiferromagnet present at the interface. There will also be a degree of diffusion between the layers during growth. This leads to region which consists of a mixture of both layers. What seems to happen, somewhat surprisingly, is that this region appears to take on its own characteristics and starts to behave semi-independently to both the ferromagnetic layer and the antiferromagnetic layer. It has been suggested [*O'Grady,2009*] that these interfacial spin clusters behave superparamagnetically, if so then they would demonstrate certain behaviours. The rest of this section is going to take this idea forward by modelling them as quasi-superparamagnetic particles and seeing if any parallels can be drawn between the experimental results and this hypothesis. If so, then some of their characteristics could possibly be described.

### 6.1.9 Superparagmagnetic Particles

For a standard paramagnetic system the magnetisation can be derived to be [*Culity, 1972*]

$$\frac{M}{M_S} = \coth a - \frac{1}{a} \qquad \text{Eqn. 6-2}$$

where $M$ is the magnetisation, $M_S$ is the saturation magnetism and $a$ is given by the following

$$a = \mu_B H/kT \qquad \text{Eqn. 6-3}$$

where $\mu_B$ is the Bohr magneton, $H$ is the applied field, $k$ is Boltzmann's constant and $T$ is the temperature. We will now consider an interfacial spin cluster which consists of $N$ spins. Because the diameter of them is so small (5 to 10nm), thermal fluctuations will overcome any inherent anisotropy within the cluster and result in it being demagnetised in the absence of a field. However, as soon as a field is applied, they will begin to align themselves in a manner that is similar to a paramagnet and so can, in certain circumstances, be modelled paramagnetically. But, rather than having the moment of a few Bohr magnetrons, if there are 50 spins in the cluster, the overall moment will be proportionally increased. Thus, as Bean and Livingston suggested [*Bean and Livingston,1959*], they could be considered to be superparagmagnetic. An important aspect of this system is, of course, the temperature. The measurements shown in this section of the results were taken at 300K, and this should be high enough for the clusters to demonstrate superparamagnetic behaviour. The measurements shown later on which were taken with liquid Helium suggests that at very low temperatures the clusters don't behave superparamagnetically. This corresponds to there being insufficient thermal energy in the system to overcome the inherent anisotropy within the cluster.

### 6.1.10 Superparamagnetism in interfacial spin clusters

In order to modify Equation 6-3 to represent superparagmagnetic behaviour all that needs to be added is an *N* on the numerator which represents the number of spins in a cluster. Figure 80 shows Equation 6-3 plotted as a function of *a*. As *a* is proportional to the applied field, if the temperature is kept constant, then the x-axis can be imagined to be the applied field. As can be seen, at low values of *a* there is a proportional relationship, but at high values the equation tends towards saturation.

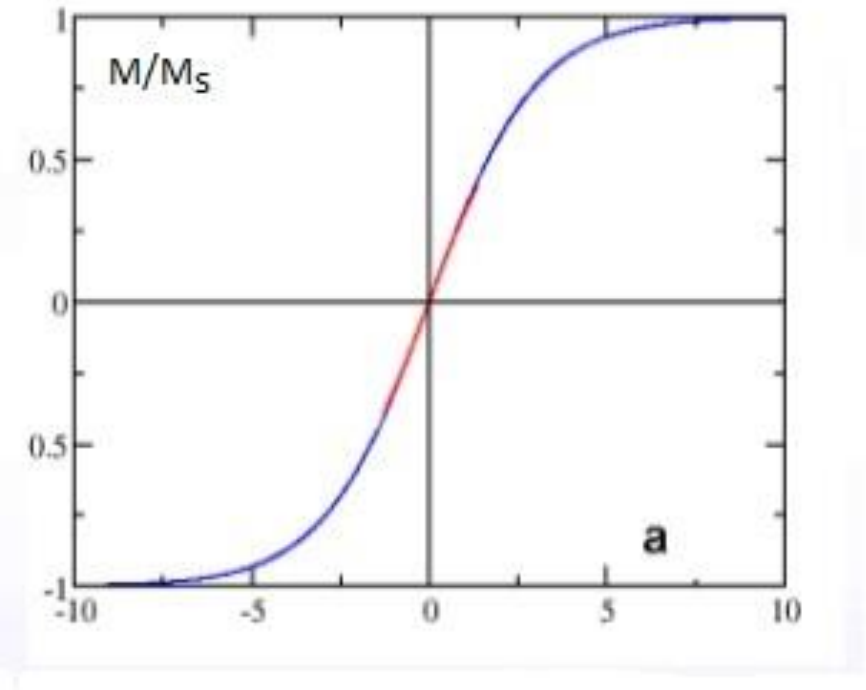


**Figure 80: Langevin function.**

After converting Equation 6-4 to a superparagmagnetic system, the next step is to modify it in order to work with interfacial spin clusters. There are two challenges here. The first is that due to the number of variables in the functions, a few assumptions have to be made in order to produce any kind of theoretical data. The second is that, unlike normal superparagmagnetic systems, these do not reduce

back to an unaligned state when the field is removed, instead, the order is 'frozen' in during the annealing process. Arguably, these two challenges are never truly overcome, and the model is being stretched somewhat. However, theoretical data can be obtained which at least suggests super-paramagnetic behaviour of the interfacial spin clusters.

The main difficulty in the first challenge is determining what *N* is and, therefore, what the saturation moment of an individual cluster is. Unfortunately, the nature and consistency of the cluster can only really be guessed. However, given the moment of Iron Cobalt is around 1400 emu/cc, if the clusters are a result of equal diffusion between the layers at the interface, then the moment of a cluster has been estimated to be 700 emu/cc. Even if this value is out by several factors, the final conclusion of this section will still hold. Next, an estimation of the thickness of the spin cluster is chosen. The presented data uses 1nm, although various thicknesses can easily be selected. Then the volume of the clusters can be considered by multiplying the grain diameter distribution function by the thickness. This will then solve Equation 6-2 for a given applied field and temperature (Equation 6-4)

$$\frac{M}{M_S} = \int_0^\infty \left( coth \frac{M_S V H}{kT} - \frac{kT}{M_S V H} \right) f(V) dV \qquad \text{Eqn. 6-4}$$

Various changes and modifications can be made to the constants that are entered into this equation. However, there is always one common aspect to all the data which is generated, and that is that the median grain diameters of the samples have been accurately determined along with the values of the standard deviation. If the distributions of the six samples are then entered in the function, curves can be generated, which are discussed in the next section.

### 6.1.11 Fitting the Theoretical data to the experimental results

Once the theoretical curves have been generated, it can be immediately seen that the samples with the larger grain sizes tend towards saturation more quickly than the smaller ones (Figure 81).

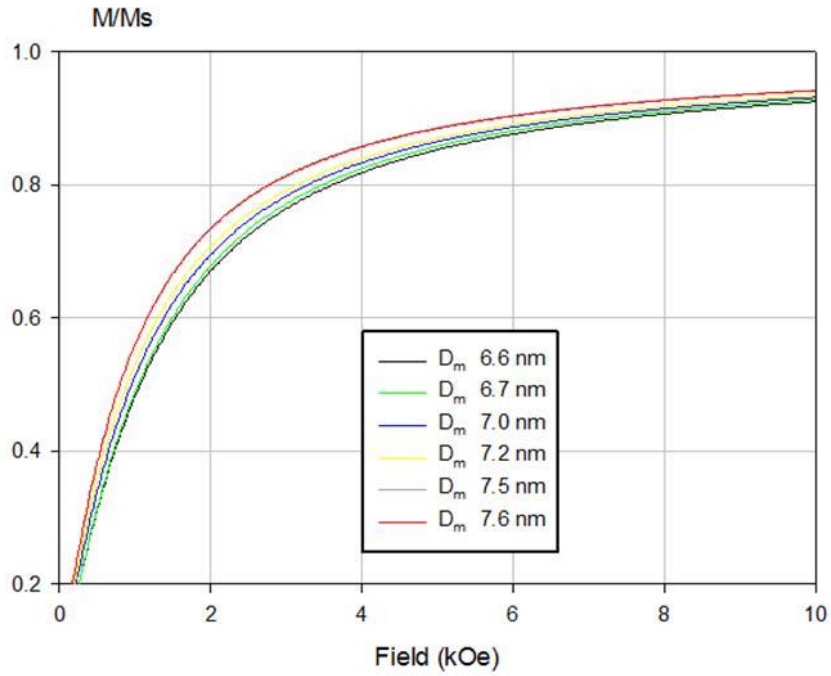


**Figure 81: Theoretical results.**

Also, as can be seen from Figure 81, the theoretical magnetisation of a purely superparagmagnetic system starts from zero. In the actual samples, the superparamagnetic state is represented as a frozen in order in the exchange bias. However, the exchange bias is not determined solely by the interfacial spin clusters, rather, it is a combination of both the bulk and the interface, and the bulk is significantly more dominant, hence, this initial zero value is not reflected in the experimental results. In Figure 79, which shows the experimental results, 6 lines

were added which were merely guides to the eye. Having just explained the theory behind how superparamagnetism can be applied to the interface spin clusters, it is now possible to superimpose the superparagmagnetic curves from Figure 81 onto the experimental data from Figure 79. When looking closely at the data in Figure 79, it can been seen that in two of the samples there is a greater degree of noise in the measurements than in the other 4, as a result, it is much more difficult to fit a good theoretical line through them. Therefore, the theoretical lines have only been fitted to 4 of the samples. However, the fit shown in Figure 82 is good and does confirm that a superparamagnetic model can be applied.

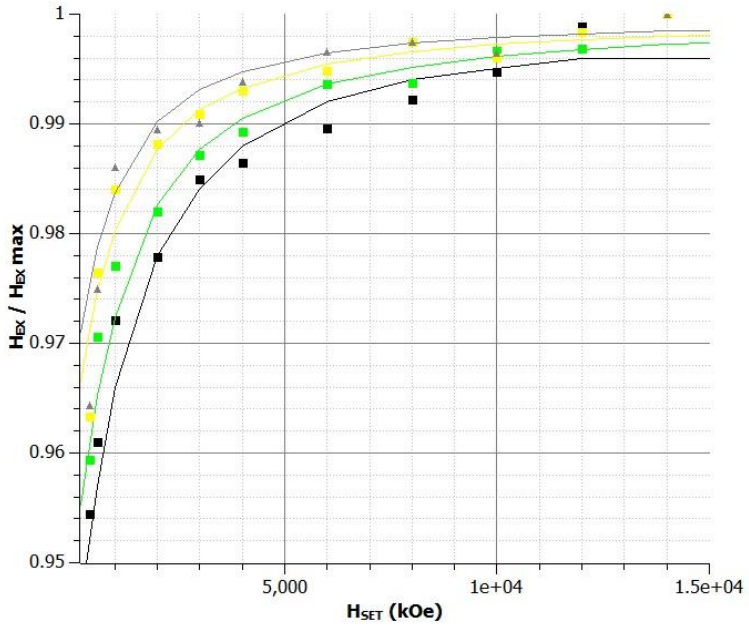


**Figure 82: Fit of superparamagntic curve over experimental results.**

It is possible that at low fields they follow the low field proportional relationship of the Langevin function. Unfortunately, it is difficult to test and verify this because at low fields the bulk itself is varying its state and so its effects will dominant in this region.

## 6.2 Effect of varying Measurement Temperature

### 6.2.1 Experimental Procedure

The intention of the next set of measurements was also try to isolate the effect of the interfacial spin clusters so that they could be investigated. The procedure was to carry out a standard blocking temperature measurement and then repeat it, but with a lower measurement temperature. This was done for measurement temperatures of 303K, 273K, 223K and 173K and was performed on three samples of differing grain sizes with the same structure as the previous measurements. After taking images with a transmission electron microscope the median grain size diameters were found to be 7.2 nm, 7.3nm and 7.8 nm (Figure 83), now called small grains, medium grains and large grains for the rest of this discussion.

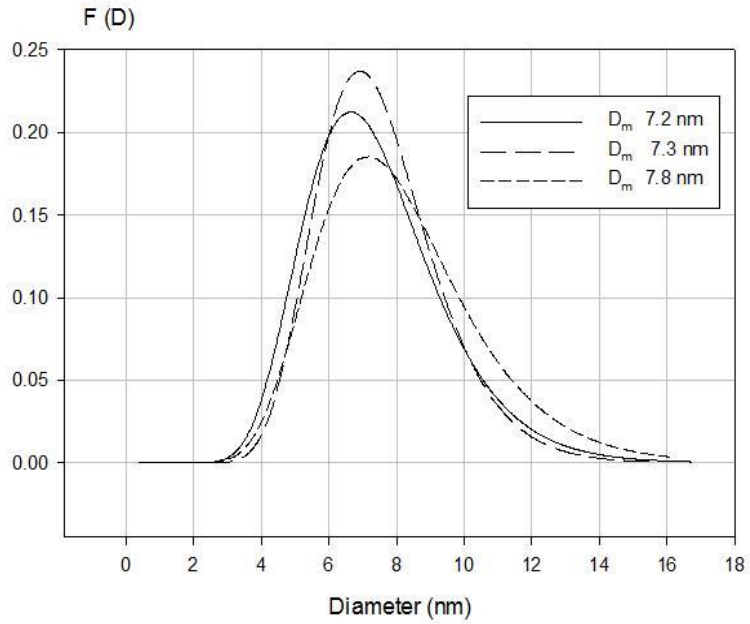


**Figure 83: Log normal distributions for the three samples.**

Carrying out a normal blocking curve with 12 points takes over 16 hours. The initial idea was to take measurements at 4 different measurement temperatures for 6 different samples, this amount of measurement time would have impacted other

research so reductions were made. The first step was to reduce the number of samples measured to three, the second was to consider reducing the number of points in a blocking curve.

For each sample, a complete blocking curve was taken at a measurement temperature of 303K. Part of the reason for this was to insure that the sample was behaving properly, but the main reason was to determine the medium blocking temperature. For subsequent measurements, the measurement temperature was reduced, which would have, in effect, added more points to the curve. Instead, only three points were taken at the lowest temperatures, then three more at or around the medium block temperature. This was decided upon because the main area of interest in this investigation was what was happening to the curve at the lower temperatures. However, it was also worth checking that the medium blocking temperature was remaining constant, despite lowering the measurement temperature.

### 6.2.2 Blocking Curves

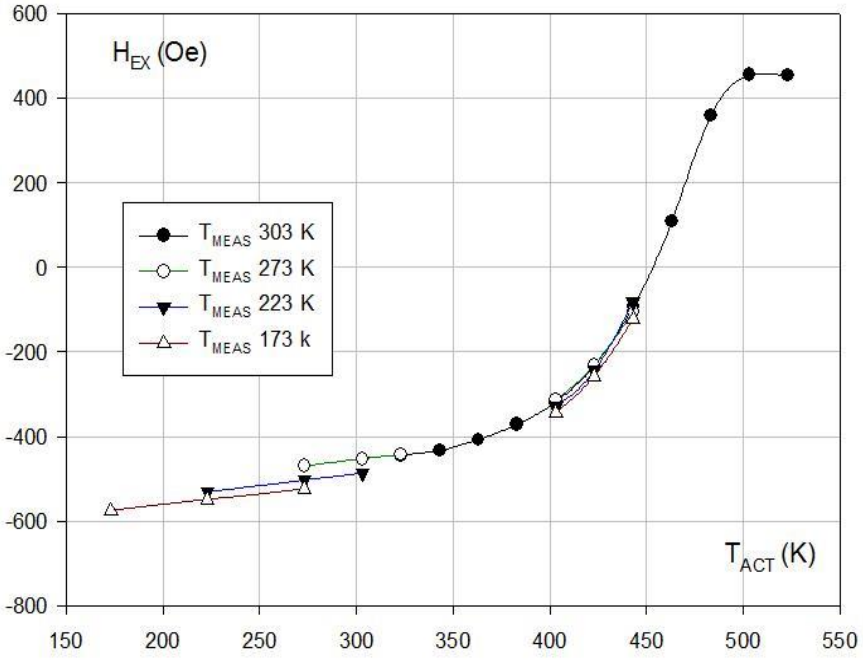


**Figure 84: $H_{EX}$ vs $T_{ACT}$, median grain diameter 7.2 nm.**

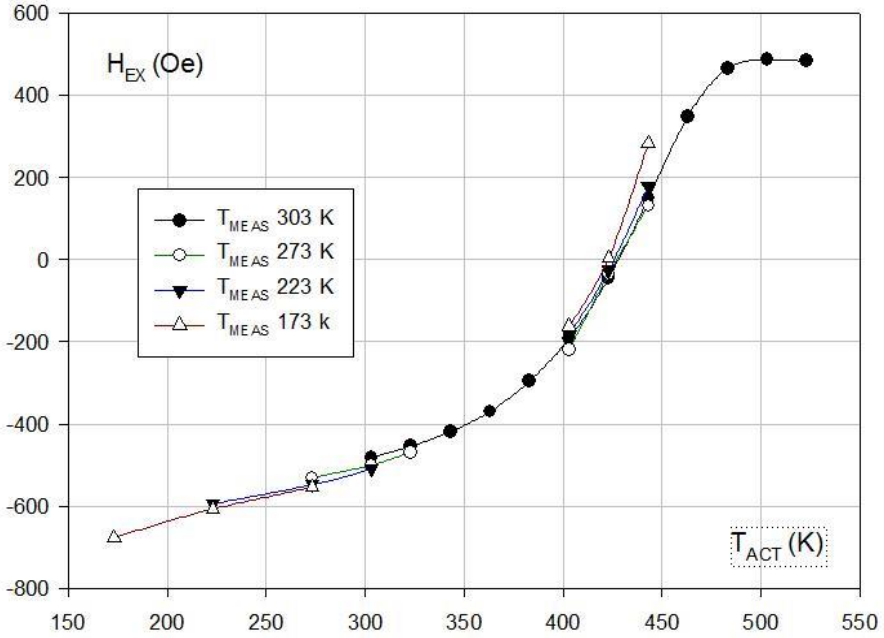


**Figure 85: $H_{EX}$ vs $T_{ACT,}$ median grain diameter 7.3 nm.**

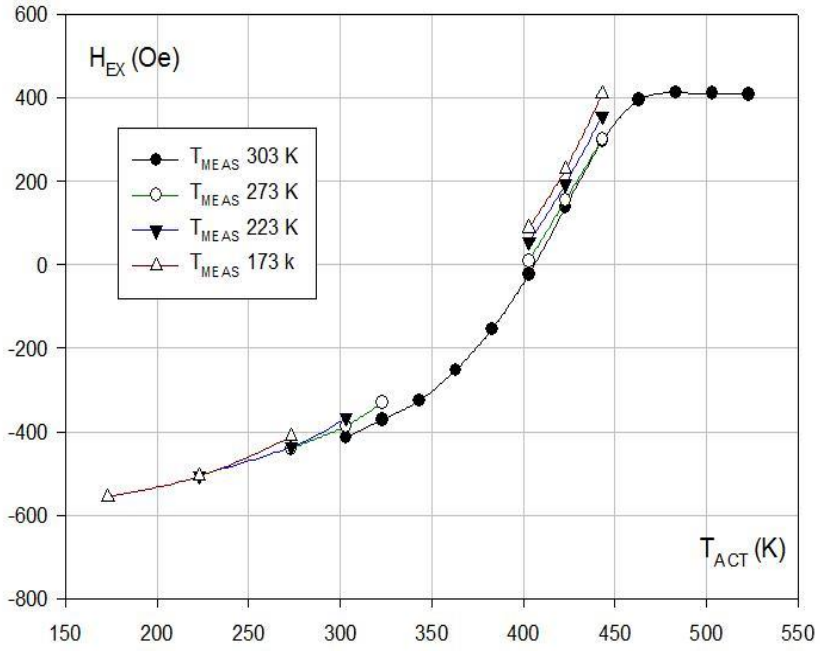


**Figure 86: $H_{EX}$ vs $T_{ACT,}$ median grain diameter 7.8 nm.**

The first trend that can be seen from the blocking curves is how quickly the exchange bias reaches reverse saturation (Figures 84, 85 and 86). From the figures, the larger the grains the sooner a complete reversal is reached. This is counter intuitive to the work described in section 4.1, for, according to grain size distributions, the sample with the smaller grains should reach saturation at a lower activation temperature. One explanation for this is that the smaller grains are less well formed and therefore do not have a constant anisotropy for a given size. This means the larger grains are better behaved and so reach saturation at a lower activation temperature

The blocking curves for the 7.3nm grain sizes show that the median blocking temperature remains constant despite reducing the measurement temperature. This is of great importance. At the median blocking temperature, half of the settable fraction of the antiferromagnet is in one direction and the other is in the opposite, which is a property of the bulk. This successfully shows that the behaviour of the bulk remains the same, despite the change in the measurement temperature. It also shows that some of the points in the curve can be missed out without determent. Unfortunately, for the smaller and larger grain sizes, the median blocking temperature was missed, however, there is still sufficient overlap of data for the above conclusion to hold.

As has been said before, the bulk of the antiferromagnet can be considered stable if the blocking curve has flattened off. As seen in these results, the curve is relatively straight for all samples at around 300k. However, what was then hoped was that at lower temperatures there would be a noticeable variation in the behaviour between the samples of different grain sizes. Unfortunately, no such variation could be seen and the subtle effects of the interface clusters in this data remained hidden.

### 6.2.3 Theoretical Fit of Blocking Curves

Although the effect of the interfacial spin clusters could not be seen in the blocking curves, it is possible to take the evaluation of this data further in the context of the model that was described in chapter 4. According to the work of *O'Grady et al.*, the blocking curve produced by the magnetic measurements is a result of the reversal of the antiferromagnetic grains as seen in the grain size analysis. Therefore, given the grain size analysis, it should be possible to predict what the magnetic blocking curve will look like.

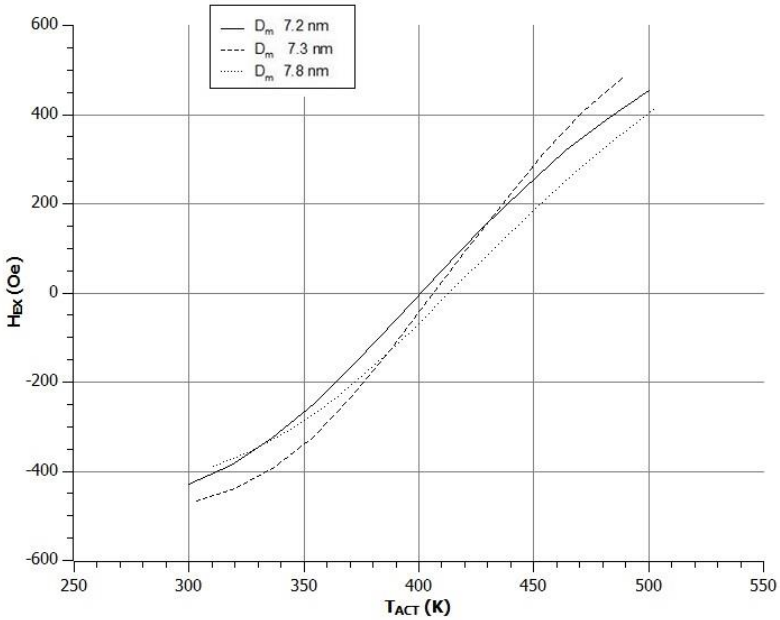


**Figure 87: Theoretical curves evaluated from grain size distribution.**

Figure 87 shows what the theoretical blocking curve looks like based on the grain size analysis given in Figure 83. The theoretical line produces a fully reversible system as the model is based on values that are defined by the median grain size and the activation temperature at which the exchange bias has become zero. As per what should be expected, the sample with the smaller grain sizes does indeed have a lower blocking temperature. This corresponds to the smaller grains having a lower energy barrier to reverse over. There is a mild curvature of the lines which

is due to the peak of the grain size about which the median volume is defined. However, this is not nearly as pronounced as in the experimental data, and there is no levelling off at the highest and lowest activation temperatures.

The lack of curvature in the theoretical lines is not easy to explain. It can reasonably be assumed that due to the polycrystalline nature of the antiferromagnet, for each grain size, there is actually a distribution of anisotropies. But, this would result in a less curvature in the experimental data not more. However, this difference between theory and experiment does now give good insight into what is going on. If the model proposed by *O'Grady et al.* is taken at face value, then the extra curvature of the experimental data suggests that the anisotropy of the antiferromagnet not only has a temperature dependence, but it also has a grain volume dependence as well and the nature of this grain volume dependence is such that the larger grains increase in anisotropy. An explanation that fits in here is that the larger grains are better structured and have a higher degree of crystallinity than the smaller ones. Unfortunately, it would prove very challenging to measure this subtle change.

The lack of the levelling off in the theoretical lines is a natural consequence of the maths behind them. What is now interesting is considering what, in the samples themselves, might be causing the levelling off in the experimental results. Clearly, from the grain size analysis, there is not an abrupt point where suddenly there are no larger grains. But, from the experimental data, the samples become fully reversed at a fairly distinct point, and there is a clear trend where the samples with the largest grain sizes level off sooner than the smaller ones. According to the model, the samples with the smaller grain sizes should level off sooner than with the larger grains and, if the magnetic measurements can be based on the grain size analysis, there should be no distinct levelling. The problem with the lack of curvature in the theoretical data can be explained away without too much difficulty, however, this levelling off is far harder to explain and is an aspect of the model which could do with some more investigation.

### 6.2.4 Coercivity Curves

Although this is labelled as section 6.2.3, in some ways, here starts the second part of the results chapter because from now on, the discussion will focus on coercivity and the role that spin clusters might take in this aspect of exchange bias.

As has been the case for all of the previous measurements, the coercivity was also determined. Throughout the blocking curves in Figures 84, 85 and 86, the coercivity remained relatively constant. So, in order to simplify the results, Figures 88 is a summary of how the coercivity varies as a function of median grain size and measurement temperature. As can be seen for all the samples, as the measurement temperature decreases and the grain size increases, the coercivity increases. The possible reasons for this will be discussed shortly, but first, there will be a brief over view of the common explanations for what causes coercivity in exchange bias systems.

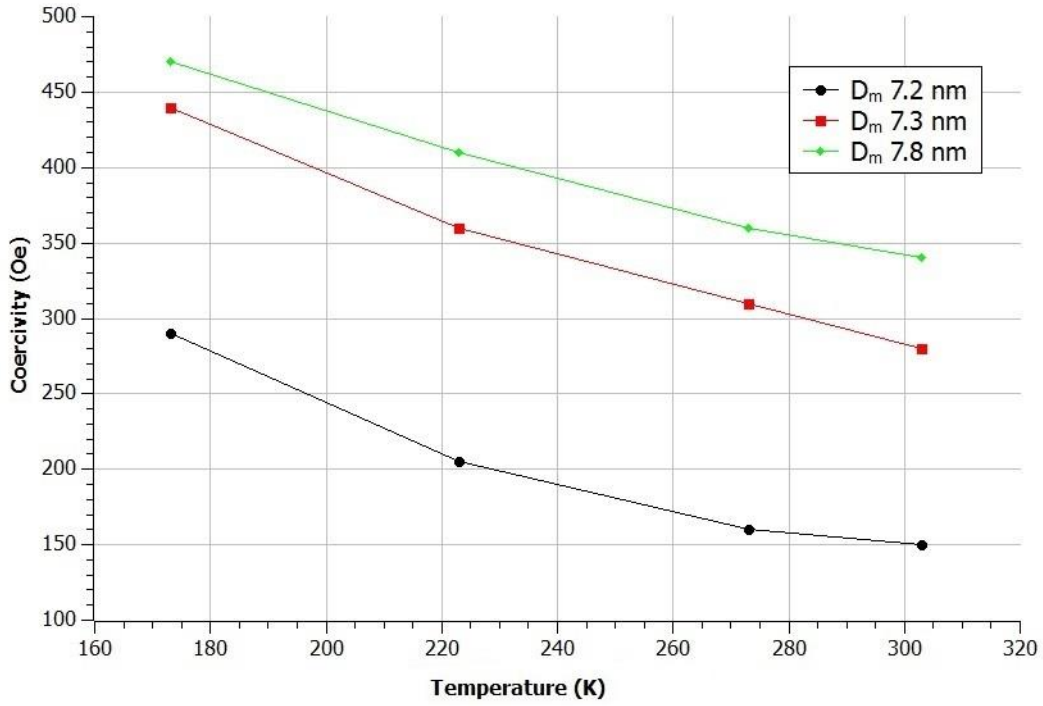


**Figure 88: Coercivity vs measurement temperature.**

### 6.2.5 Explanations of Coercivity at high temperatures

The variation in coercivity in exchange bias systems was reported along with its other features in 1956 [*Meiklejohn and Bean,1957*] and has been the subject of a number of investigations. Although it has never been given the same prominence as the shift in the hysteresis loop, it is an aspect of exchange bias and if a complete model is to be presented then it must include a discussion on coercivity. The temperature dependence of coercivity has often been investigated [*Fulcomer,1972, Nishioka,1996, Nishioka,1997, Ali,2003, Baltz,2010* ] but there is a different kind of behaviour depending on the temperature region being considered. The first temperature region being considered is around the blocking temperature and will be discussed in this section, 6.2. The second temperature region is what happens around 4.2K and is discussed in Section 6.3.

Coming back to the first temperature region, it has been seen before [*Nishioka,1997, Ali,2003*] that the coercivity tends to peak at around the blocking temperature. The source of the increase in exchange bias systems is usually attributed to thermally unstable antiferromagnetic grains that are coupled to the ferromagnet. During magnetic reversal, these grains, along with the ferromagnet, are also reversed and add an extra ‘drag’ to the process, thus increasing coercivity. As the temperature of the system approaches the blocking temperature, there are more of these thermally unstable antiferromagnetic grains which increase the coercivity. As the blocking temperature is passed, the antiferromagnetic structure starts to break down, the grains no longer behave antiferromagnetically, and so the coercivity reduces.

### 6.2.6 Spin Cluster effect in Coercivity

Although coercivity is often attributed to thermally unstable antiferromagnetic grains coupled to the ferromagnet [*Baltz, 2010*], it is not possible to reconcile this explanation with the results shown in Figure 88. If the coercivity is due to thermally unstable grains then there should be a range of grain sizes which fall into this category. This range would make up part of a grain size distribution and would have a lower limit consisting of the smallest grains in this category, and a higher limit consisting of the largest grains in this category. Now, this lower limit would remain the same regardless of conditions, whereas the higher limit would depend on the measurement temperature. The higher limit actually defines the point at which an antiferromagnetic grain goes from being unstable and contributing to the coercivity to being stable and therefore contributing to the exchange bias. The position of this limit is defined by the temperature of the measurement.

It, therefore, follows that as the temperature is reduced so does this higher limit. By reducing the measurement temperature, one is in effect, reducing the number of thermally unstable grains contributing to the coercivity and this should then result in a decrease in coercivity. In Figure 88, the opposite it seen. This then implies that perhaps the thermally unstable grains are not so significant in their contribution to the coercivity. Instead, the entity that might be creating the increase in coercivity is, in fact, the spin clusters. If they were, then an increase in the spin cluster size would result in an increase in coercivity, which is seen in the results. If the spin clusters also have an anisotropy that is temperature dependent, then, as the temperature decreases, the anisotropy would increase as would the coercivity and this is also seen. The concept of the spin clusters having a significant effect on the coercivity is discussed more in section 6.3.

### 6.2.7 Anisotropy Calculations from Coercivity.

For some systems it is actually possible to calculate the anisotropy form the coercivity. By minimizing the energy in the basic equation postulated by Meiklejohn and Bean (Equation 3-1), it is possible to derive an expression that relates the coercivity to the anisotropy of a magnetic system

$$H_C = \frac{4K}{M_s} \qquad \text{Eqn. 6-5}$$

where $H_C$ is the coercivity, *Ms* is the saturation magnetisation and *K* is the anisotropy (the same value of *Ms* as used in section 6.1 has been used here). From this, anisotropy values can be calculated given the coercivities in Figure 88.

| Temperature<br>Medium Grain Size | 173 K | 223 K | 273 K | 303 K |
|---|---|---|---|---|
| 7.2 nm | $5.8 \times 10^4$ | $4.1 \times 10^4$ | $3.2 \times 10^4$ | $3.0 \times 10^4$ |
| 7.3 nm | $8.8 \times 10^4$ | $7.2 \times 10^4$ | $6.2 \times 10^4$ | $5.6 \times 10^4$ |
| 7.8 nm | $9.4 \times 10^4$ | $8.2 \times 10^4$ | $7.2 \times 10^4$ | $6.8 \times 10^4$ |

**Table 7: Anisotropy values when varying measurement temperature (ergs/cc)** *Si/Ta(5nm)/Ru(5nm)/IrMn(10nm)/CoFe(2nm)/Ta(5nm)***.**

The main positive aspect of equation 6-5 is the ability to calculate the anisotropy of the samples given the coercivity, and then compare these values to each other and to different systems. The main drawback is down to what equation 3-1 is based on, which is a basic Stoner-Wohlfarth system. A Stoner-Wohlfarth system is modelled on a single domain particle reversing, where as it is far more complex in an exchange biased system. The other problem is the temperature dependence of the anisotropy. A temperature dependent form of the anisotropy for the bulk was suggested in Chapter 4, however, so little is known about the nature of the interfacial spin clusters, it is not possible to establish a temperature dependent function for them. All that can be said is that as the temperature decreases, so does the anisotropy.

## 6.3 Low Temperature Measurements

### 6.3.1 Modifications to Measurements

The final set of measurements taken used liquid Helium in order to get down to as low a temperature as possible. A number of trail sessions were needed in order to get sufficient signal to measure and resulted in some changes to the set up. The first change required was to increase the thickness of the ferromagnetic layer as the 2 nm did not give a large enough moment. Various thickness were experimented with to find a good balance between sufficient signal and sufficient exchange bias, which is given by Equation 6-6 below

$$H_{EX} \alpha \frac{1}{t_F} \qquad \text{Eqn. 6-6}$$

It was found that 10nm was a good compromise. The reasons for the reduced signal was a combination of the fact that the sample had to be placed in a cryostat, which effectively added extra shielding for the sample, along with the vibrations of the cryostat due to the workings of the cryopump.

As mentioned by Vallejo-Fernandez [*Vallejo-Fernandez, 2008*], increasing the thickness of the ferromagnet significantly increases the exchange field the antiferromagnet experiences from the ferromagnet. This can have a very noticeable effect on the properties of the bilayer and reduces, for example, the value of the median blocking temperature. However, as long as there is an awareness of the effects which the above paper outlines, then the ferromagnetic thickness can be changed, but with caution.

The original idea was to set the sample at 225 $^{O}$C for 90 minutes and then field cool to the measurement temperature and then reset it again before the next measurement. The issue here was that the cryostat would only go up to 100 $^{O}$C and so, in order to get to 225 $^{O}$C, the sample had to be removed and placed in another annealing furnace. It was found that when this was done, the results were of a very low quality, most probably due to the sample not staying in exactly the same position throughout the procedure.

Therefore, the measurement was changed to setting the sample, field cooling down to the initial temperature of 4.2K, taking a hysteresis loop, raising the temperature and taking another loop. In this case, the only change between each measurement is an increase in the temperature, if the bulk is assumed stable at such low temperatures, then any variation seen is due to an increase in the disorder at the interface due to thermal energy.

As per the other samples, grain size analysis was performed. The median diameters were found to be 5.0 nm, 6.3 nm and 7.1 nm (Figure 89). Again, these will be referred to in the text as being small, medium and large grain sizes.

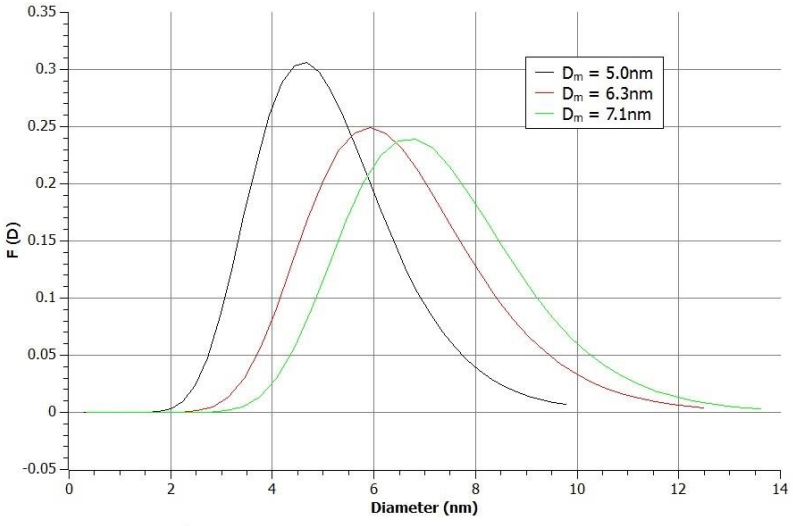


**Figure 89: Log normal distributions for the three samples used in the Helium measurements.**

### 6.3.2 Magnetic Measurements

Section 6.2 looked at the coercivity at relatively high temperatures, this section is going to look at what happens to the coercivity at low temperatures. The effect of a significant increase in the coercivity at liquid Helium temperatures has been known for some time [*Nishioka,1996, Ali, 2003*], however, there has never been a serious attempt to explain it. Here, a relatively simple comparison to what happens to the exchange bias in this temperature region will be made and used to help explain this phenomenon, which will also lend support to the argument of the spin cluster contribution to coercivity.

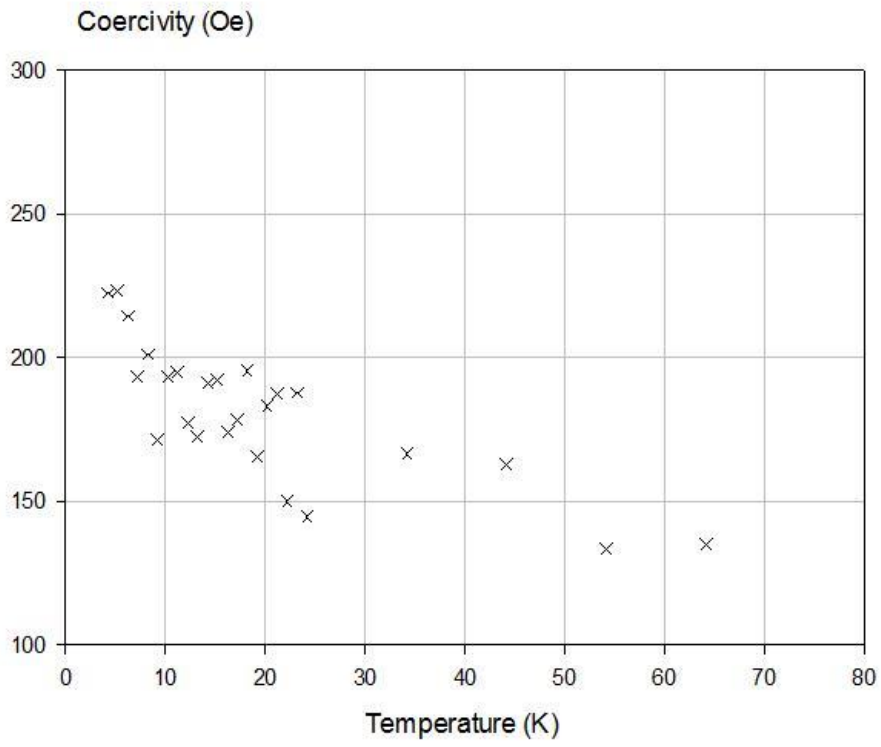


**Figure 90: $H_C$ vs $T_{MEAS}$, median grain diameter 5.0 nm.**

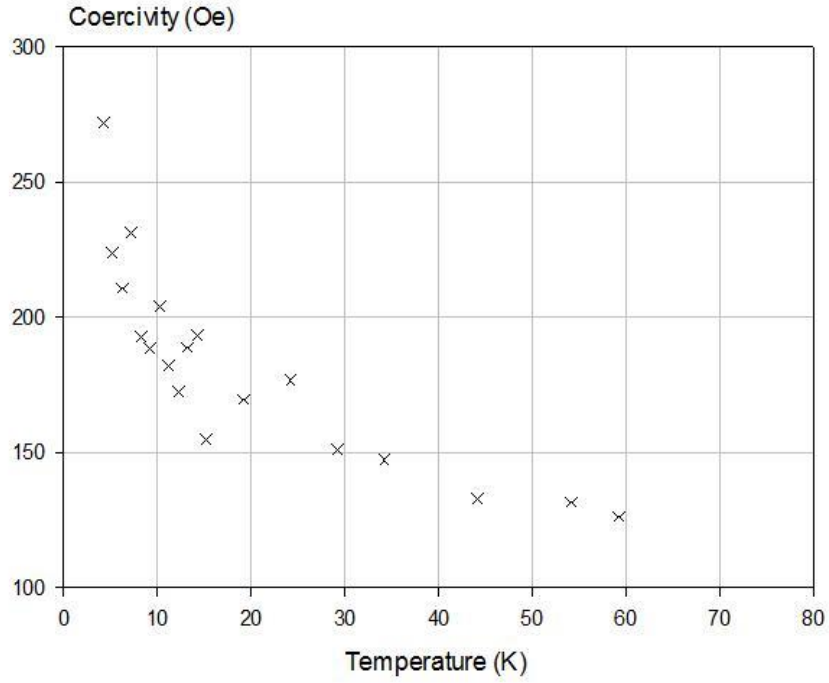


**Figure 91: $H_C$ vs $T_{MEAS}$, median grain diameter 6.3 nm.**

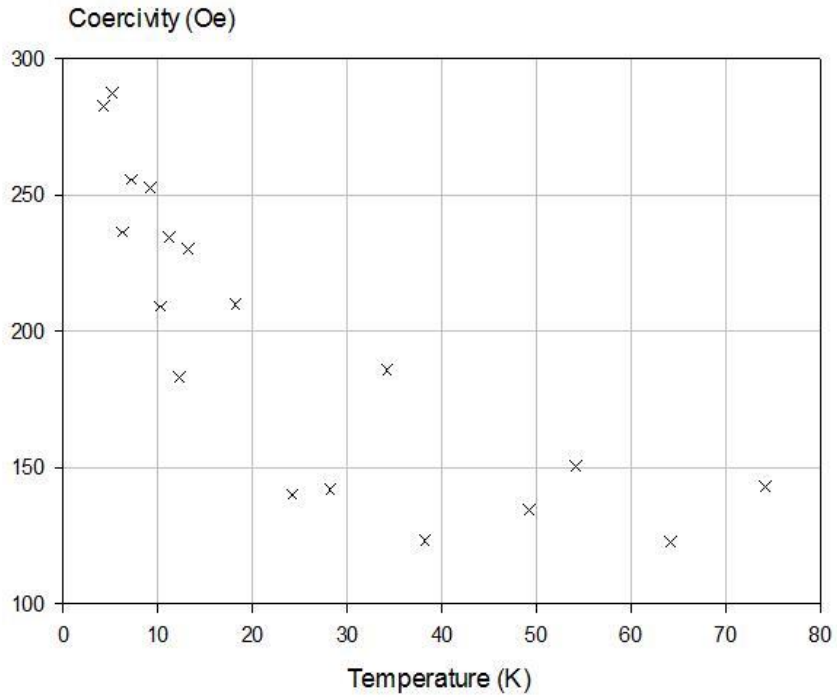


**Figure 92: $H_C$ vs $T_{MEAS}$, median grain diameter 7.1 nm.**

It has been reported before [*Fernandez-Outon,2008*] that when the temperature of an exchange bias system approaches 4.2K, the exchange bias can increase by up to 25%. Now, well above this temperature the vast majority of the bulk of the antiferromagnet has become stable, so the question is what is causing such a significant increase. The suggestion made in order to explain such an effect is that the interfacial spin clusters are entering a highly ordered state similar to that of a spin glass. Therefore, if the coercivity also increases in this temperature region where the interfacial spin clusters are going through this change of state, then the spin clusters must surely be contributing the coercivity.

Figures 90, 91 and 92 show the coercivity measurements at low temperatures. Again, just like in section 6.2, there is a clear grain size variation in the results. All three samples show a levelling off at around 150 Oe, and this similarity between them could suggest that this residual coercivity is actually due to the bulk. The significant increase which starts between 30K and 50K can then be attributed to the interfacial spin clusters entering into a spin glass state. If the grain diameters are then converted into volumetric rations, then there is a similarity between the increase in volume compared to the increase in coercivity.

### 6.3.3 Calculation of anisotropy values

| Temperature<br>Medium Grain Size | 4.2 K | 223 K |
|---|---|---|
| 7.2 nm | $4.5 \times 10^4$ | $2.7 \times 10^4$ |
| 7.3 nm | $5.4 \times 10^4$ | $2.6 \times 10^4$ |
| 7.8 nm | $5.8 \times 10^4$ | $2.4 \times 10^4$ |

**Table 8: Anisotropy values for Helium measurements (ergs/cc)**
*Si/Ta(5nm)/Ru(5nm)/IrMn(10nm)/CoFe(10nm)/Ta(5nm)***.**

Using Equation 6-5, the anisotropies of the samples can be calculated (Table 8). The first, most obvious difference between table 7 and table 8 is the reduction in anisotropy from the samples in 6.2 to the samples in 6.3. This is due to the increase in size of the ferromagnetic layer from 2nm to 10nm. This fivefold increase significantly reduces any effect that the antiferromagnetic bulk or spin clusters have on the ferromagnetic layer. If the layer size could have remained constant between the two experiments, then a better comparison could have been made, but, as was explained in section 6.3.1, this was not possible.

### 6.3.4 Grain size distribution of spin clusters

Baltz shared the view of Ali and Nishioka [*Baltz,2010 , Nishioka,1996, Ali,2003*] where he thought the coercivity was not a product of the interfacial spin clusters, but rather due to any thermally unstable grains during the measurement. Again, as with the coercivity work at high temperatures, this hypothesis conflicts with the results in the work presented here. If the coercivity is due to the thermally unstable grains, then, as the temperature of a sample is increase, the number of thermally unstable grains would increase which would result in an increase in the coercivity. The opposite is seen in Figures 89, 90 and 91.

As mentioned in section 4.1.10, there are a number of assumptions made in the work carried out by *O'Grady et al.* with regards to what constitutes a grain and what its antiferromagnetic behaviour is. There are other schools of thought [*Ali,2003*] that might not want to limit an antiferromagnet domain to the discrete black regions shown on the TEM images in Figures 41. However, the model proposed by *O'Grady et al.* is the foundation upon which this research has been carried out and the interpretations presented here are, therefore, an extension of the model.

This is important to note because the whole concept of the spin cluster is that it resides on the uppermost surface of the discrete antiferromagnetic grains. The assumption made is that the spin clusters share the diameter of the antiferromagnetic grain, however, unlike the grain, may be interacting with its neighbours. This is then extended, in the maths presented in section 6.1.10, to the belief that the grain size distribution determined for the bulk grains can be directly applied to the grain size distribution of the spin clusters. When these assumptions were made, the theoretical fit to the experimental fit as shown in Figure 82 was good.

Having re-establish this, the next thing to deal with is the hidden issue in the results presented in the whole of section 6. In the first set of spin cluster measurements (Section 6.1), the magnetic entity in the sample which responds to the increasing setting field beyond the saturation point of the ferromagnet is said to be the spin clusters. This order is then set in while field cooling. During the hysteresis measurement, the field is fully cycled and the exchange bias is retained, but the spin clusters which have contributed to the significant increase in exchange bias do not reverse.

The latter experimental results presented in section 6 discuss the spin clusters contribution towards coercivity. Here, a decrease in temperature always results in an increase of coercivity. It has already been explained how this is counter to the hypothesis that the unstable grains are responsible for coercivity. Also, at the low temperatures used in section 6.3.2, the bulk is stable, so the variation to coercivity must be attributed to the spin clusters. Here comes the hidden issue, in this situation during a hysteresis measurement, if one is considering the spin cluster contribution to coercivity, the spin clusters now reverse. There needs to be attempt to explain the difference in behaviour between the irreversible spin clusters in section 6.1 and the reversible spin clusters in section 6.3.

It is known that the coercivity of an exchange bias system passes through a peak as the temperature is lowered. This is consistent with an entity consisting of an energy barrier distribution passing through a consequent blocking temperature distribution. In the work of *Fernandez-Outon et al.* [*Fernandez-Outon,2008*] the measurements were invariably made at temperatures where the bulk of the antiferromagnetic grains is stable and hence there must be a second entity the spin clusters which gives rise to the peak in the coercivity. The hypothesis is that a fraction of the spin clusters are able to reverse in the field whilst a second fraction are unable to reverse. This gives rise to an irreversibility in the spin clusters consistent with a grain size distribution deriving from the antiferromagnetic grains.

It can now be suggested that the larger, more thermally stable ones, have their order set in during the setting process, and this order remains during cooling so that they are irreversible during hysteresis. Whereas, the smaller, less thermally stable ones contribute towards coercivity. Given this explanation, it is tempting to propose the following segregation between the two states that the spin clusters can be in.

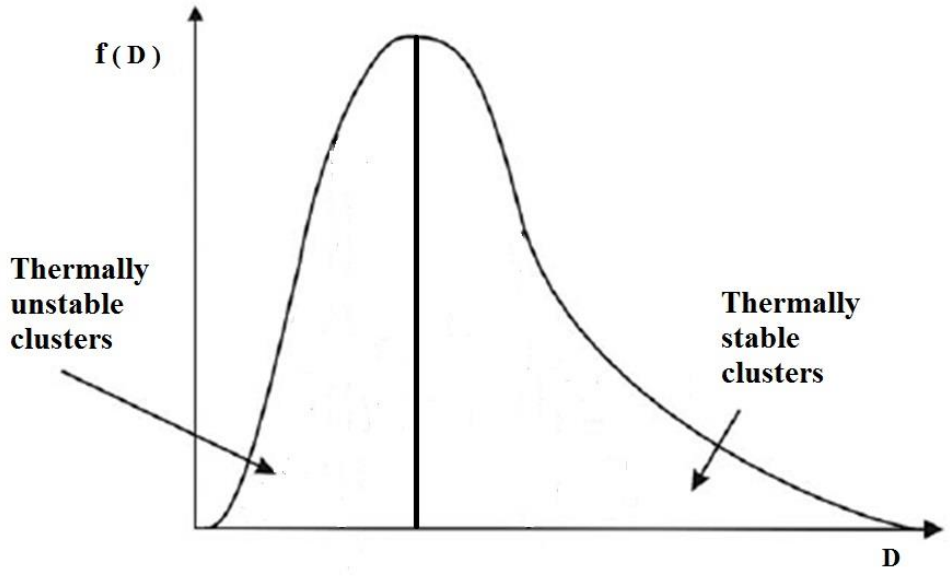


**Figure 93: Two phase diagram of spin clusters.**

Unfortunately, this theory does not fit in with the results given in Section 6.3.2. If this theory was true then, as the temperature decreases, there would be less thermally unstable spin clusters and the coercivity would decrease, not increase as is seen in the results.

However, there is an explanation that can attribute the coercivity to the spin clusters and also explain why the coercivity increases with decreasing temperature. It is worth restating here that at very low temperatures, the bulk grains are stable so the coercivity increase is being attributed to a variation in the state of the spin clusters. Another set of results of importance in this line of argument is that of from the work of Fernandez-Outon [*Fernandez-Outon,2008*]. Here, he presents experimental data which shows that at low temperatures, the Exchange bias increases by up to 25%. This is attributed to the interfacial spin clusters entering a more highly ordered state and are starting to taking on a spin glass nature. This again demonstrates that the spin clusters are contributing significantly to the state of the sample and are going through a transitional phase.

Figure 93 gives a grain size distribution of the spin clusters which, as has already been said, fails to explain the variation of coercivity at low temperatures, but a small change to this can help (Figure 94).

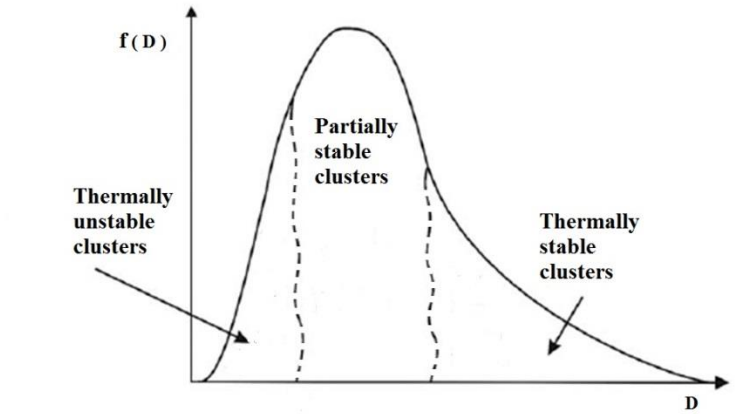


**Figure 94: Three phase diagram of spin clusters.**

Instead of a distinct line, it is suggested that there is, in fact, a very broad transitional phase from stable to unstable. So now, rather than there being two states to consider, there are three, the unstable, the partially stable and the stable.

When it is suggested that the coercivity is attributable to the unstable grains [*Nishioka,1996*], their size and volume is such that it is conceivable that they would induce a 'drag' on the reversal of the ferromagnet and, thereby, increase its coercivity. However, in the situation of the spin clusters, they are so small that when fully thermally unstable, they would not have any noticeable effect on the ferromagnet and would, therefore, not contribute to the coercivity. But, the situation is different for those spin clusters which, when looking at Figure 94, are in the transitional phase. These clusters which are becoming more stable are starting to couple more strongly to the already set bulk. They are not fully set though, as otherwise they would cease to contribute to the coercivity and instead contribute towards the exchange bias. Now it is possible to explain why a decrease in temperature increases coercivity because as the measurement temperature is reduced, this transitional region increases, which, in turn, increases the coercivity.

The next phase of the model would be to attempt to determine where these boundaries lie. The spin clusters are undergoing a very complex relationship with both the ferromagnet above them and the bulk antiferromagnet below them. The relationship between these three elements is further complicated by the fact that there is most probably no clearly defined boundary between the three. The spin clusters themselves reside at the blurred interface between the antiferromagnet and the ferromagnet, and due to the diffusion that will occur during deposition, attempts to model them will become very complex.

Regardless of the complications of producing an accurate, all round, model of the spin clusters, explanations of how the spin clusters, when irreversible, contribute towards the exchange bias and, when reversible, contribute towards the coercivity have been given. These explanations satisfy the results that have been seen and add extra insight the nature of exchange bias.

# 7. Conclusion and Future Work

## 7.1 Conclusions

The work of *O'Grady et al*. as described in section 4.1 explains how, when considered as discrete entities, the bulk of the antiferromagnet contributes to the exchange bias and, by following the protocol described, it is possible to accurately control the exchange bias of a system. However, although it may be able to predict the exchange bias as a function of the bulk, there are a number of effects that it does not explain mathematically such as the training effect, high field effects, variations in coercivity, and low temperature effects.

Whenever a set of measurements have been taken during this work, the training effect has always been calculated and considered. Whether it was carrying out normal blocking curves, increasing the setting field or reducing the measurement temperature, no correlation or pattern was ever found. It has already been established that the training effect is an interfacial property [*Kaeswurm,2011*], but beyond that, there is little that can be said for certain, other than it is an irreversible effect that occurs as a product of field cycling.

In regards to the other effects, experiments have been carried out that successfully demonstrate non-bulk properties which can be explained by the interfacial spin cluster concept which sit on top of an ordered grain. In the results described in section 6.1, the clusters were modelled as consisting of a number of disordered spins which behave in a quasi-superparagmagnetic manner. It is possible that at low fields they follow the low field proportional relationship of the Langevin function. However, it is difficult to test and verify this as the bulk effects are dominant in this region. At higher fields, there was clearly a component of the bilayer which responded to an increasing magnetic field, and this component

showed a grain size dependence. It is not too large a step to attribute this response to that of the interfacial spin clusters.

In section 6.2, a variety of measurements were carried out, some of which overlapped the work carried out by previous people [*O'Grady,2009*]] and others which started to investigate variations in coercivity. The main point to be drawn from these was the idea that, perhaps, rather than the coercivity being solely due to thermally unstable grains, there was actually another entity contributing to it.

The low temperature results of section 6.3, seemed to further lend weight to the above argument and even led to the idea that a significant contribution to the coercivity was actually from the interfacial spin clusters. A model was also put forward that explained the trends in the data which was based on the various thermal states the spin clusters could be in, all of which showed a grain size dependence.

Attributing the increase in coercivity in an exchange bias system to the interfacial spin clusters is not widely accepted, but it does fit in well in the context of the work by *O'Grady et al*. The initial aim of this work, as per the title of the thesis, was to characterise the interfacial spin clusters in polycrystalline thin films and, in this regard, good progress has been.

## 7.2 Future Work

There was a time when the exchange bias of thin films made a large contribution to magnetic conferences, now the effort put in to this research is diminished. Many of the research groups who studied the phenomenon have moved on to other work, as shown by the dates of the major topical reviews on this subject. There are probably not many more significant papers that will be written on exchange bias in thin films.

If the work of this particular thesis was to be continued in a focussed manner, then, as has been said, all of the experiments that have been described could be repeated for ever thinner antiferromagnetic thicknesses. In this way it might be possible to pin point when the bulk effects become less dominant and the interface effects become more so, which might lead to greater insight into the nature of interfacial spin clusters.

However, research into exchange bias and its applications are far from over as there are new and exciting technologies that can and do find a use for it. In these other areas, the antiferromagnet is not extended across a substrate of up to 5mm x 5mm. Instead, much small dimensions are being studied, such as nano-pillars. These are most applicable to the science of MRAM, where the current desire is to increase data density.

In this technology, new challenges are posed in the form of edge effects. In the work presented in this thesis, the edge and corner effects remain largely unconsidered due to the relative size over which the sample is extended in the horizontal plane when compared to the vertical height of the stack. However,

when the dimensions of the device are reduced, they become of great importance. Research is already being carried out in these areas with progress being made in the understanding of how exchange bias works on such a small scale [*Vallejo-Fernandez,2009, Baltz,2010(b)*].

In terms of gaining understanding into the nature of interfacial spins clusters, adding the new complications that come about from significant downsizing in the horizontal plane probably does not make the challenge any easier. In fact, it might even make a topic that is only partially understood even more complicated. However, investigating how exchange bias can be used on devices such as nano-pillars is the correct direction for the continuing research to go in.

# 8. List of Symbols

**A**

| | |
|---|---|
| A | Area |
| a | Lattice constant |
| AC | Alternating current |
| AF | Antiferromagnet |
| AGFM | Alternating Gradient Force Magnetometer |
| AMR | Anisotropic Magnetic Resistance |

**B**

| | |
|---|---|
| $\beta$ | Angle between ferromagnet magnetisation and antiferromagnet magnetisation |
| $\mu_B$ | Bohr magneton |
| bcc | Body centred cubic crystal |

**C**

| | |
|---|---|
| CIP | Current in plane |
| CIS | Current induced switching |
| CPP | Current perpendicular to plane |
| C* | Interfacial coupling constant |

**D**

| | |
|---|---|
| $\overline{D}$ | Mean diameter |
| d | Lattice Spacing |
| $<D_V>$ | Volume fraction diameter |
| DC | Direct current |

| | |
|---|---|
| $\rho$ | Density |

**E**

| | |
|---|---|
| $\Delta E$ | Energy barrier |
| E | Energy |
| EDX | Energy Dispersive X-ray Analysis |
| EELS | Electron Energy Loss Spectroscopy |
| emf | Electromotive force |
| $E_K$ | Crystal anisotropy energy |
| $E_X$ | Interlayer exchange energy |

**F**

| | |
|---|---|
| $f_0$ | Attempt frequency |
| F | Ferromagnet |
| $F_X$ | Force |
| $F_q$ | Uncoated resonant frequency of quartz crystal in thickness rate monitor of HiTUS |
| f(D) | Grain diameter distribution |
| f($\Delta E$) | Energy barrier distribution |
| f(V) | Grain volume distribution |
| fcc | Face Centred Cubic crystal |
| $\Phi$ | Magnetic flux |

**G**

| | |
|---|---|
| GMR | Giant Magnetoresistance Resistance |

## H

| | |
|---|---|
| h | Plank's Constant |
| H | Applied field |
| HAADF | High Angle Annular Dark Field Imaging |
| H* | Exchange field from ferromagnet |
| $H_C$ | Coercivity |
| $H_{C1}$ | Coercive field on descending branch of hysteresis loop |
| $H_{C2}$ | Coercive field on ascending branch of hysteresis loop |
| $\Delta H_{C1}$ | Training effect on descending branch |
| $\Delta H_{C2}$ | Training effect on ascending branch |
| $H_D$ | Demagnetising field |
| $H_{EX}$ | Exchange bias |
| $H_K$ | Anisotropy field |
| $H_K^*$ | Pseudo anisotropy field in a ferromagnet |
| $H_N$ | Nucleation field |
| $H_M$ | Molecular field |
| $H_{mA}$ | Molecular field experience by sublattice A |
| $H_{mB}$ | Molecular field experience by sublattice B |
| $H_{SET}$ | Setting field |
| hcp | Hexagonal closed packed |
| HiTUS | High Target Utilisation Sputtering |

## I

| | |
|---|---|
| I | Current |

## J

| | |
|---|---|
| $J_{EX}$ | Exchange integral |

| | |
|---|---|
| $J_{INT}$ | Interface coupling constant |
| Jsf | Spin-flop coupling |
| $J_{NET}$ | Direct coupling constant |
| J | Interlayer exchange |

**K**

| | |
|---|---|
| K | Crystalline anisotropy |
| $K_{AF}$ | Anisotropy constant of antiferromagnet |
| $K_F$ | Anisotropy constant of ferromagnet |
| $K_{SC}$ | Anisotropy constant spin cluster |
| $k_B$ | Bolztmann constant |

**L**

| | |
|---|---|
| l | Length |
| L | Domain diameter |

**M**

| | |
|---|---|
| M | Magnetisation |
| m | Moment |
| **m**(0) | Net sublattice magnetisation direction |
| μ | Median |
| $m_{AF}$ | Sublattice magnetisation |
| $M_A$ | Magnetisation of Sublattice A |
| $M_B$ | Magnetisation of Sublattice B |
| $M_f$ | Change in mass of quartz crystal due to deposition |
| $M_F$ | Ferromagnetic magnetisation |
| $M_q$ | Mass of quartz crystal |
| $M_S$ | Saturation magnetisation |
| MBE | Molecular Beam Epitaxy |

| | |
|---|---|
| MRAM | Magnetic Random Access Memory |
| MOKE | Magneto Optical Kerr Effect |
| MOIF | Magneto-Optic Indicator Technique |

**N**

| | |
|---|---|
| N | Integer number |
| $N_D$ | Demagnetising factor |

**O**

| | |
|---|---|
| Oe | Oested |

**P**

| | |
|---|---|
| PID | Proportional Integral Differential controller |

**R**

| | |
|---|---|
| R | Resistance |
| $R_P$ | Resistance – parallel configuration |
| $R_{AP}$ | Resistance- antiparallel configuration |
| RAM | Random Access Memory |
| $r_a$ | Atomic radius |
| $r_{3d}$ | Radius or 3d subshell |
| RF | Radio Frequency |
| $\rho$ | Resistivity |
| RKKY | Ruderman Kittel Kasuya Yosida |
| $\delta$ | Resolution of Optical Microscope |
| $\mu$ | Refractive Index |

## S

| | |
|---|---|
| S | Magnetic viscosity coefficient |
| $S_i$ , $S_j$ | Spin quantum number |
| σ | Standard deviation |
| SQUID | Super Conducting Interference Device |

## T

| | |
|---|---|
| T | Temperature |
| t | Time |
| τ | Time in which magnetisation decays to 1/e of original value |
| θ | Angle between single axis and applied field |
| $t_0$ | constant |
| $T_{ACT}$ | Thermal activation temperature |
| $t_{ACT}$ | Time of thermal activation |
| $t_{AF}$ | AF thickness |
| $T_B$ | Blocking temperature |
| $<T_B>$ | Median Blocking temperature |
| $T_C$ | Curie point |
| $t_{CR}$ | Critical thickness in Mauri model |
| TEM | Transmission Electron Microscope |
| $t_F$ | Thickness of ferromagnet |
| $T_{MEAS}$ | Measurement temperature |
| $T_N$ | Néel temperature |
| $T_{NA}$ | Temperature of no thermal activation |
| $T_{SET}$ | Setting temperature |
| $t_{SET}$ | Setting time |
| TMR | Tunnelling Magnetoresistance |

**U**

| | |
|---|---|
| **u** | Easy directions of the uniaxial anisotropy |

**V**

| | |
|---|---|
| <V> | Median grain volume |
| V | Volume |
| $V_{ACT}$ | Volume of largest grain that can be aligned at a given activation temperature $T_{ACT}$ |
| $V_C$ | Critical grain volume |
| $V_m$ | Median grain volume |
| $V_{SC}$ | Volume of spin cluster |
| $V_{SET}$ | Volume of the largest grain that can be set at a given setting temperature $T_{SET}$ |
| VSM | Vibrating Sample Magnetometer |

**W**

| | |
|---|---|
| w | Width |
| λ | Wave length |

**Y**

| | |
|---|---|
| Y | Young's Modulus |

**Z**

| | |
|---|---|
| Z | Dimensionless parameter |

# 9. Bibliography

## A

Aley, N.P., Vallejo-Fernandez, G., Kroeger, R., Lafferty, B., Agnew, J., Lu, Y., O'Grady, K., Texture Effects in IrMn/CoFe Exchange Bias Systems. IEEE Transactions on Magnetics, 2008, 44(11): p2820-2823 (a)

Aley, N.P., Bonet, C., Lafferty, B., O'Grady, K., Effect of Cu Impurities on $K_{AF}$ in $IrMn_{1-x}Cu_x$/CoFe Exchange Bias System. IEEE Transactions on Magnetics, 2008, 45(10): p3858-3861 (b)

Ali, M., Marrows, C. H., Al-Jawad, M., Hickey, B., J., Misra, A. Nowak, U. Usadel, K. D., Antiferromagnetic layer thickness dependence of the IrMn/Co exchange-bias system. Physical Review B, 2003. 68(21): p. 214420.

Ali, M., C.H. Marrows, and B.J. Hickey, Controlled enhancement or suppression of exchange biasing using impurity δ layers. Physical Review B, 2008. 77(13): p. 134401.

Ambrose, T. and C.L. Chien, Dependence of exchange coupling on antiferromagnetic layer thickness in NiFe/CoO bilayers. Journal of Applied Physics, 1998. 83(11): p. 6822-6824.

## B

Baibich, M.N., et al., Giant Magnetoresistance of (001)Fe/(001)Cr Magnetic Superlattices. Physical Review Letters, 1988. 61(21): p. 2472.

Baltz, V., Rodmacq, B., Zarefy, A., Lechevallier, L., Dieny, B., Bimodal distribution of blocking temperature in exchange-biased ferromagnetic/antiferromagnetic bilayers. Physical Review B, 2010, 81, 052404

Baltz, V., Gaudin, G., Somani, P., Dieny, B., Influence of edges on the exchange bias properties of ferromagnetic/antiferromagnetic nanodots. Applied Physics Letters, 2010, 96, 262505 (b)

Bean, C. P., Livingston, J.D., Supperparamagnetisim. Journal of Applied Physics, 1959, 30, 120S-129S

**C**

Carey, M.J., Smith, N., Gurney, B.A., Childress, J.R., Lin, T., J.Appl. Phys. 89 (2001) 6579

Crangle, J., Solid State Magnetism. 1991: Van Nostrand Reinhold.

Cramp, N.C., Carpenter, R., O'Grady, K.,Characterisation of Interface Spin Clusters in Exchange Bias Systems. IEEE Transactions on Magnetics, 2012, 48(11): p2881-2884.

Cullity, Introduction to Magnetic Materials. 1972.

**F**

Fernandez-Outon, L., E., Vallejo-Fernandez, G., Manzoor, S., Hillebrands, B., O'Grady, K., Interfacial spin order in exchange biased systems. Journal of Applied Physics 2008 104, 093907

Fert A., Jaffres, H.. Manttana, R Seneor, P. EuroPhys. News, 2003. 34(6): p. 227

Fecioru-Morariu, M., Güntherodt, G.,Exchange coupling between an amorphous ferromagnet and a crystalline antiferromagnet. Journal of Applied Physics. 2007 102, 053911 (a)

Fecioru-Morariu, M., Ali, S., Papusio, C., Sperich, M., Güntherodt, G., Effects of Cu Dilution in IrMn on the Exchange Bias of CoFe/IrMn Bilayers. Physical Review Letters, 2007. 99(9): p. 097206 (b)

Flanders, P.J., An Alternating-Gradient Magnetometer. Journal of Applied Physics, 1988. 63(8): p. 3940.

Foner, S., Vibrating Sample Magnetometer. Review of Scientific Instruments, 1956. 27(7): p. 548-548.

Fontana, J.R.C.a.R.E.J., C. R. Physique, 2005. 6: p. 997.

Fulcomer, E. and S.H. Charap, Thermal fluctuation aftereffect model for some systems with ferromagnetic&antiferromagnetic coupling. Journal of Applied Physics, 1972. 43(10): p. 4190-4199.

Fulcomer, E. and S.H. Charap, Temperature and frequency dependence of exchange anisotropy effects in oxidized NiFe films. Journal of Applied Physics, 1972. 43(10): p. 4184-4190.

## G

Granqvist, C.G. and R.A. Buhrman, Ultrafine metal particles. Journal of Applied Physics, 1976. 47(5): p. 2200-2219.

Grimsditch, M., et al., Exchange-Induced Anisotropies at Ferromagnetic-Antiferromagnetic Interfaces above and below the Néel Temperature. Physical Review Letters, 2003. 90(25): p. 257201.

Grove, W.R., On the Electro-Chemical Polarity of Gases. Philosophical Transactions of the Royal Society of London, 1852. 142: p. 87-101.

Grünberg, P., et al., Layered Magnetic Structures: Evidence for Antiferromagnetic Coupling of Fe Layers across Cr Interlayers. Physical Review Letters, 1986. 57(19): p. 2442-2445.

## H

Hitatchi. https://www1.hitachigst.com

Hoffmann, A., Symmetry Driven Irreversibilities at Ferromagnetic-Antiferromagnetic Interfaces. Physical Review Letters, 2004. 93(9): p. 097203.

## I

IHS Technology. https://www.technology.ihs.com

Imakita, K.., M. Tsunoda, and M. Takahashi, Giant exchange anisotropy observed in Mn--Ir/Co--Fe bilayers containing ordered Mn[sub 3]Ir phase. Applied Physics Letters, 2004. 85(17): p. 3812-3814.

## J

Jette, E., et al., Trans. Am. Inst. Mining. Met. Engrs, 1934. 87: p. 7094.

Jiles, D., Introduction to Magnetism and Magnetic Materials. Chapman and Hall. 1991

Jung, H.S., W.D. Doyle, and S. Matsunuma, Influence of underlayers on the soft properties of high magnetization FeCo films. Journal of Applied Physics, 2003. 93(10): p. 6462-6464.

## K

Kaeswurm, B. and K. O'Grady, The origin of athermal training in polycrystalline metallic exchange bias thin films. Applied Physics Letters, 2011. 99(22): p. 222508.

Kaeswurm, B., O'Grady, G. Interfacial and bulk order in polycrystalline exchange bias systems. Journal of Applied Physics. 2010. 107: p09D727

Katine, J.A., et al., Current-Driven Magnetization Reversal and Spin-Wave Excitations in Co /Cu /Co Pillars. Physical Review Letters, 2000. 84(14): p. 3149-3152

Keller, J., et al., Domain state model for exchange bias. II. Experiments. Physical Review B, 2002. 66(1): p. 014431.

Knoll, M.a.R., E., Z. Physic, 1932(78): p. 318.

Koon, N.C., Calculations of Exchange Bias in Thin Films with Ferromagnetic/Antiferromagnetic Interfaces. Physical Review Letters, 1997. 78(25): p. 4865.

**M**

Malozemoff, A.P., Random-field model of exchange anisotropy at rough ferromagnetic-antiferromagnetic interfaces. Physical Review B, 1987. 35(7): p. 3679.

Mauri, D., et al., Novel method for determining the anisotropy constant of MnFe in a NiFe/MnFe sandwich. Journal of Applied Physics, 1987. 62(7): p. 2929-2932.

Meiklejohn, W.H. and C.P. Bean, New Magnetic Anisotropy. Physical Review, 1957. 105(3): p. 904.

Mott, N., Proc. R. Soc. A, 1936. 153: p. 699.

**N**

Neel, L., Influence des Fluctuations du Champ Moleculaire sur les Proprietes Magnetiques des Corps. Annals of Physics, 1932. 18: p. 5-105.

Neel, L., Interface Roughness. Annals of Physics, 1967. 2.

Nishioka, K., et al., Grain size effect on ferro-antiferromagnetic coupling of NiFe/FeMn systems. Journal of Applied Physics, 1996. 80(8): p. 4528-4533.

Nishioka, K., et al., Thickness effect on ferro/antiferromagnetic coupling of Co/CrMnPt systems. Journal of Applied Physics, 1998. 83(6): p. 3233-3238.

Nogués, J. and I.K. Schuller, Exchange bias. Journal of Magnetism and Magnetic Materials, 1999. 192(2): p. 203-232.

Nowak, U., et al., Domain state model for exchange bias. I. Theory. Physical Review B, 2002. 66(1): p. 014430.

## O

O'Handley, R.C., Modern Magnetic Materials, Principles and Applications. John Wiley and Sons Inc., 2000

O'Grady, K., Bradbury, A, Particle size analysis in ferrofluids, Journal of Magnetism and Magnetic Materials, 1983, 39,91-94

O'Grady, K., V.G. Lewis, and D.P.E. Dickson, Alternating gradient force magnetometry: Applications and extension to low temperatures (invited). Journal of Applied Physics, 1993. 73(10): p. 5608-5613.

O'Grady, K., Fernandez-Outon, L. E., Vallejo-Fernandez, G. A new paradigm for exchange bias in polycrystalline thin films. Journal of Magnetism and Magnetic Materials. 2009 doi:10.1016/j.jmmm.2009.12.011

## P

Parkin, S.S.P., N. More, and K.P. Roche, Oscillations in exchange coupling and magnetoresistance in metallic superlattice structures: Co/Ru, Co/Cr, and Fe/Cr. Physical Review Letters, 1990. 64(19): p. 2304-2307.

Peng, X., et al., Effect of material selection and background impurity on interface property and resulted CIP-GMR performance. Journal of Magnetism and Magnetic Materials, 2009. 321(18): p. 2902-2910.

## S

Sampaio, L. C., Mougin, A., Ferré, J., Georges, P., Brun, A., Bernas, H., Poppe, S., Mewes, T., Fassbender, J., Hillerbrands, B., Probing interface magnetism in the FeMn/NiFe exchange bias system using magnetic second-harmonic generation., EuroPhysics Letters, 2003, 63, 819

Sang, H., Y.W. Du, and C.L. Chien, Exchange coupling in Fe[sub 50]Mn[sub 50]/Ni[sub 81]Fe[sub 19] bilayer: Dependence on antiferromagnetic layer thickness. Journal of Applied Physics, 1999. 85(8): p. 4931-4933.

Sakuma, A., et al., First-principles study of the magnetic structures of ordered and disordered Mn-Ir alloys. Physical Review B, 2003. 67(2): p. 024420.

Sauerbrey G.Z., Phys. Verhand. 8 193 (1957)

Shull, R.D., et al., Stationary antiferromagnetic domains during magnetization reversal in an exchange-biased FeMn/Fe[sub 76]Mn[sub 6]C[sub 18] bilayer. Journal of Applied Physics, 2003. 93(10): p. 8603-8605.

Slonczewski, J.C., Current-driven excitation of magnetic multilayers. Journal of Magnetism and Magnetic Materials, 1996. 159(1–2): p. L1-L7

Stamps, R.L., Mechanisms for exchange bias. Journal of Physics D: Applied Physics, 2000. 33(23): p. R247.

Stiles, M.D. and R.D. McMichael, Model for exchange bias in polycrystalline ferromagnet-antiferromagnet bilayers. Physical Review B, 1999. 59(5): p. 3722 (a)

Stiles, M.D. and R.D. McMichael, Temperature dependence of exchange bias in polycrystalline ferromagnet-antiferromagnet bilayers. Physical Review B, 1999. 60(18): p. 12950 (b)

Stiles, M.D. and R.D. McMichael, Coercivity in exchange-bias bilayers. Physical Review B, 2001. 63(6): p. 064405

Stoner E. C., W.J.C., A Mechanism of Magnetic Hysteresis in Heterogeneous Alloys. Phil. Tran. Roy. Soc., 1948. A240: p. 599.

## T

Takano, K., Kodama, R. H., Berkowitz, A. E., Cao, W., Thomas, G., Anisotropy in Polycrystalline Ni81Fe19/CoO Bilayers. Physics Review Letters, 1997, 79, 1130

Thomson, W., Proc. R. Soc., 1857. 8: p. 546.

Thomson, J.J., Cathode Rays. The Electrician, 1897. 39: p. 104.

Tomeno, I., et al., Magnetic neutron scattering study of ordered Mn[sub 3]Ir. Journal of Applied Physics, 1999. 86(7): p. 3853-3856.

Thompson, S. J., The discovery, development and future of GMR: The Nobel Prize 2007, Journal of Physics D: Applied Physics, 2008, 41, 093001

Tsunoda, M., et al., L12 phase formation and giant exchange anisotropy in Mn3Ir/Co–Fe bilayers. Journal of Magnetism and Magnetic Materials, 2006. 304(1): p. 55-59.

Tsunoda, M., Uncompensated antiferromagnetic spins at the interface in Mn?Ir based exchange biased bilayers. Journal of Applied Physics., 2007. 101(9): p. 09E510.

## V

van der Heijden, P.A.A., et al., Thermally assisted reversal of exchange biasing in NiO and FeMn based systems. Applied Physics Letters, 1998. 72(4): p. 492-494.

Vallejo-Fernandez, G., Fernandez-Outon, L. E., O'Grady, K., Measurement of the anisotropy constant of antiferromagnets in metallic polycrystalline exchange biased systems. Applied Physics Letters. 2007. 91, 212503

Vallejo-Fernandez, G., et al., Effect of the Ferromagnetic Layer Thickness on the Blocking Temperature in IrMn/CoFe Exchange Couples. Magnetics, IEEE Transactions on, 2008. 44(11): p. 2835-2838.

Vallejo-Fernandez, G., Fernandez-Outon, L. E., O'Grady, K., Antiferromagnetic grain volume effects in metallic polycrystalline exchange bias systems. Journal of Physics D: Applied Physics. 2008. 41. 112001 (b)

Vallejo-Fernandez, G., Fernandez-Outon, L. E., O'Grady, K., Thermal activation of bulk and interfacial order in exchang biased systems. Journal of Applied Physics. 2008. 103. 07C101 (c)

Vallejo-Fernandez, G., Aley, N.P. Fernandez-Outon, L. E., O'Grady, K., Control of the setting process in CoFe/IrMn exchange bias systems. Journal of Applied Physics. 2008. 104. 033906 (d)

Vallejo-Fernandez, G., Chapman, J. N., Size effects in submicron exchange bias square elements Applied Physics Letters . 2009. 94. (26) ISSN 0003-6951

Vallejo-Fernandez, G. et al., Measurement of the antiferromagnet activity in exchange bias systems. Journal of Applied Physics., 2010. 107: p.09D709

Vopsaroiu, M., Thwaites, M., Rand, S., Grundy, P.J., O'Grady, K. Novel Sputtering Technology for Grain-Size Control. IEEE Transactions on Magnetics 2004 40(4) p.2443-2445

Vopsaroiu, M., Fernandez, G.V., Thwaites, M., Anguita, J., Grundy, P.J., O'Grady, K., Deposition of polycrystalline thin films with controlled grain size. Journal of Physics D: Applied Physics 2005. 38. p490-496 (a)

Vopsaroiu, M., Thwaites, M., Fernandez, G.V., Lepadatu, S., O'Grady, K., Grain size effects in metallic thin films prepared using a new sputtering technology. Journal of Optoelectronics and Advanced Materials. 2005. 7(5) p.2713-2720 (b)

**W**

Williams, D.a.C., C., Transmission Electron Microscopy. Vol. 1. 1996.

**X**

Xi, H., Theoretical study of the blocking temperature in polycrystalline exchange biased bilayers. Journal of Magnetism and Magnetic Materials, 2005. 288: p. 66-73.

**Y**

Yamaoka, T., Antiferromagnetism in γ-Phase Mn-Ir Alloys. Journal of the Physical Society of Japan. 36(Copyright (C) 1974 The Physical Society of Japan): p. 445.

**Z**

Zijlstra, H., A Vibrating Reed Magnetometer For Microscopic. AIP Review of Scientific Instruments, 1970. 41(8): p. 1241.